Departement Natuurkunde
Faculteit van de wetenschappen
Vrije Universiteit Brussel

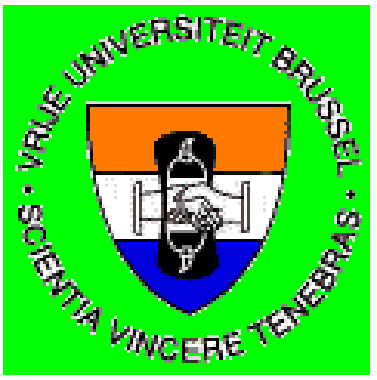

Triple Regge analysis of single diffractive photoproduction at HERA

Roel Heremans
december 2002

Triple Regge analysis of single diffractive photoproduction at HERA

PROEFSCHRIFT

ingediend met het oog op
het behalen van de wettelijke graad
van doctor in de wetenschappen
aan de Vrije Universiteit Brussel

door

Roel Heremans

Promotiecommissie:

Promotor:	Prof. Dr. R. Roosen, Vrije Universiteit Brussel
Voorzitter:	Prof. Dr. J. Van Craen, Vrije Universiteit Brussel
Secretaris:	Prof. Dr. R. Roosen, Vrije Universiteit Brussel
Overige leden:	Prof. Dr. E. De Wolf, Universiteit Antwerpen
	Prof. Dr. J. Lemonne, Vrije Universiteit Brussel
	Prof. Dr. P. Marage, Université Libre de Bruxelles
	Prof. Dr. A. Sevrin, Vrije Universiteit Brussel
	Prof. Dr. T. Sloan, Lancaster University

Cover: HERA, the Hadron Electron Ring Accelerator at the DESY laboratory in Hamburg. (Photo: David Parker/SPL taken from *The Particle Odyssey: A Journey to the Heart of Matter*, F. Close, M. Marten, C. Sutton, *Oxford University Press* (2002))

Dedicated to the memory of my father.

Abstract

A new measurement is presented, using the H1 detector, of the differential cross section $M_X^2 \; d\sigma/dM_X^2$ for the process $\gamma p \rightarrow XY$, with a large rapidity gap between the systems X and Y and with Y a proton or a low mass proton excitation, at three centre of mass energies $\langle W \rangle$ = 91, 187 and 231 GeV. The slope parameter $\alpha_{eff}(0)$ obtained from a single Regge type parameterization with a single effective trajectory is presented as a function of M_X^2. A combined triple Regge fit is performed over these data together with leading proton data from the same experiment and lower energy fixed target data. The pomeron intercept $\alpha_{I\!P}(0)$ is extracted from this fit and was found to be $\alpha_{I\!P}(0)=$ $1.127 \pm 0.004(\mathrm{stat}) \pm 0.025(\mathrm{syst}) \pm 0.046(\mathrm{mod})$. The extracted triple Regge couplings are compared with those obtained from pp-data and found to be in reasonable agreement. Diffractive data like $F_2^{D(3)}$, F_2^{LP} and F_2^{LN} were compared in the deep inelastic region with a triple Regge model, using either the triple Regge couplings extracted from the combined triple Regge fit or using the triple Regge couplings which were determined from pp data. A reasonable description of the data at low Q^2 and high M_X is found for both methods.

Contents

List of Figures

List of Tables

Chapter 1

Introduction

The data analysed in this thesis has been collected at HERA, which is the world's first electron-proton collider situated near to Hamburg, Germany. The large centre of mass energy ($\sqrt{s} \approx 300$ GeV) obtained by colliding electrons of 27.5 GeV on 820 GeV protons, allows to explore new regions, where particles with masses up to 300 GeV can be produced, where the structure of the proton can be studied with a resolving power varying over 5 orders of magnitude down to dimensions of 10^{-18} m and where partons with very small fractional proton momenta (Bjorken-x down to 10^{-6}) become experimentally accessible.

The H1 and ZEUS experiments, both consisting of multipurpose detectors, installed respectively around the northern and southern interaction point of HERA, observed in 1993 a large number of events in which in a large interval in rapidity no final state particles were observed. These events, nowadays known as rapidity gap events, are interpreted as diffractive events resulting from the exchange of a colorless object called the *pomeron*. Since their observation, rapidity gap events have been extensively studied. In particular, because the large Q^2 photons available at HERA allow to investigate the internal structure of the pomeron.

In the present analysis, rapidity gap events are studied using the process $ep \to Xp$, where X represents the photon dissociation system. The process will be analysed in the photoproduction limit where the photon's momentum transfer $Q^2 \to 0$, i.e. the photon is quasi-real. In particular the differential cross section $M_X^2 \; d\sigma/dM_X^2$ is measured and subjected to a triple Regge analysis in which also data from fixed target experiments and leading proton data are considered. The results of this analysis are then also extrapolated to the deep inelastic region to investigate where the transition between the soft and hard processes takes place.

The structure of the thesis is as follows: Chapter 2 introduces the main feature of lepton-nucleon scattering going over the deep inelastic diffractive scattering, towards the topic of this thesis, diffractive scattering in photoproduction. Here the triple Regge theory is introduced and a summary of existing analysis in this domain is reviewed stressing those measurements which will be used in either the triple Regge analysis or in comparisons made in chapter 6. Chapter 3 reviews the main layout of the HERA accelerator and introduces

the pilot bunch concept. Also the main H1 detector components are briefly described, with emphasis on those which are of particular importance in this analysis. Chapter 4 treats the subject of background identification, data selection and mass reconstruction. Chapter 5 describes the extraction of the differential cross section, $M_X^2\ d\sigma(\gamma p \to XY)/dM_X^2$. In chapter 6, the results obtained in chapter 5 together with earlier diffractive data are subjected to a triple Regge analysis. These results are then extrapolated to the deep inelastic regime.

Chapter 2

Theoretical introduction

The HERA physics program to date has primarily focused on testing our understanding of the strong force. Measurements have been performed in kinematic regions where perturbative QCD calculations are accurate, as well as in regions where no hard scale is present and non-perturbative processes dominate. In the following section, the structure of the proton and the measurement of the proton structure function will be briefly reviewed. Subsequently the concept of structure functions in deep inelastic diffractive scattering will be schematically outlined. Then the framework in which soft diffractive processes are considered, i.e. the triple Regge formalism, constituting the theoretical framework in the analysis of this thesis, will be treated in detail. As the roots of this theory date back to the late sixties, the triple Regge formalism has been applied to several diffractive final states in γp- and pp-experiments in the past. These results will be reviewed at the end of this section with emphasis on those obtained at the HERA experiment.

2.1 Lepton-nucleon scattering

In the most general case the lepton-nucleon interaction proceeds via the exchange of a virtual vector boson as depicted in figure 2.1. Since the lepton number has to be conserved, we expect the presence of a scattered lepton in the final state, while the nucleon fragments into a hadronic final state X. The interaction is called inelastic when a quark is knocked out of the proton, and the proton is broken up. It is called deep when the proton is probed with a gauge boson which resolves small distance scales.

The following four Lorentz invariant variables are most commonly used to describe the lepton nucleon scattering:

$$\begin{aligned} s &= (k+P)^2, \\ Q^2 &= -q^2 = -(k-k')^2, \\ x &= \frac{Q^2}{2P.q}, \\ y &= \frac{q.P}{k.P}. \end{aligned}$$

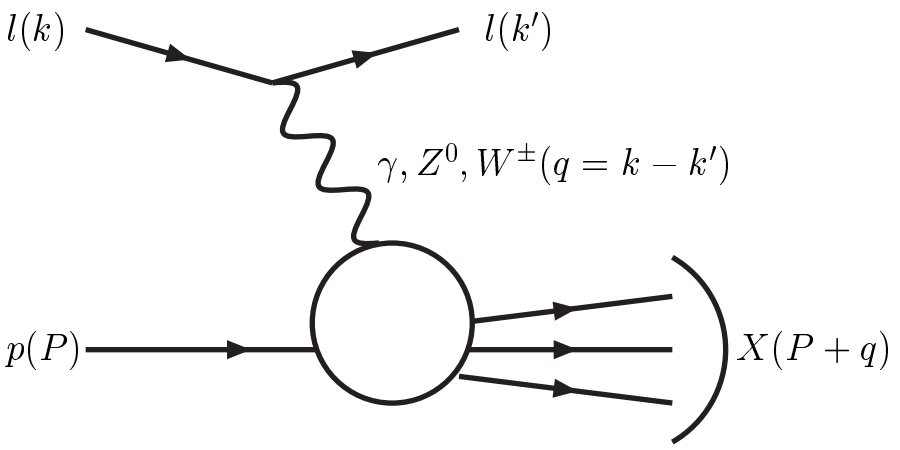

Figure 2.1: *Schematic diagram describing inelastic lepton-nucleon scattering. The four-vectors of the particles, or system of particles, are given in parentheses.*

where the four-vectors of the initial and final lepton, of the incoming nucleon, and of the outgoing hadronic system, are represented by k, k', P and P' respectively. The variable s is the centre of mass energy squared with $\sqrt{s} \approx 300$ GeV at HERA[1]. Because of the large value of s at HERA, photons with a virtuality $Q^2 \approx 10^4$ GeV^2 can be produced, resolving sizes as small as $\sim 10^{-18}$ m. In the proton rest frame the expression for y reduces to

$$y = 1 - \frac{E_{l'}}{E_l}, \tag{2.1}$$

where $E_{l'}$, E_l are the energies of the scattered lepton and incoming lepton, respectively. In this frame the dimensionless variable y is a measure of the fraction of the incident electron energy which enters the interaction. In the parton model the Bjorken variable x can be interpreted as the fraction of the proton momentum carried by the massless struck quark. At fixed centre of mass energy $\sqrt{s}$, only two of these four variables (x, y, s, Q^2) are independent due to energy momentum conservation. When the electron and proton are assumed to be massless the relation between them is:

$$Q^2 = xys. \tag{2.2}$$

In addition W is defined as the centre of mass energy of the exchanged boson and the incoming proton

$$\begin{aligned} W^2 = (q + P)^2 &\simeq ys - Q^2 \\ &\simeq Q^2 \left(\frac{1}{x} - 1\right) \end{aligned} \tag{2.3}$$

[1]This is for 27.5 GeV incident electrons or protons and 820 GeV protons.

2.2 Proton structure function

Most generally, the cross section of unpolarized ep-scattering is written as a tensor product made up of a leptonic and a hadronic part, $\sigma \sim L_{\mu\nu}W^{\mu\nu}$, where $W^{\mu\nu}$ represents the hadronic tensor, which parameterizes the interaction occurring between the exchanged boson and the proton. Consideration of the requirements of Lorentz invariance and current conservation lead to the following expression for the deep inelastic neutral current cross section for not too high Q^2 [1, 2]:

$$\frac{d^2\sigma(ep \to eX)}{dxdQ^2} = \frac{4\pi\alpha_{em}^2}{xQ^4}\left[(1-y+\frac{y^2}{2})F_2(x,Q^2) - \frac{y^2}{2}F_L(x,Q^2)\right] \quad (2.4)$$

$$= \frac{4\pi\alpha_{em}^2}{xQ^4}\left[(1-y+\frac{y^2}{2})\,\sigma_r\right] \quad (2.5)$$

where α_{em} is the electromagnetic coupling constant and $F_2(x,Q^2)$ and $F_L(x,Q^2)$ are structure functions which provides information on the quark and gluon content of the proton and $\sigma_r = F_2 - \frac{y^2}{1+(1-y)^2}F_L$. In order to describe fully the neutral current DIS at high Q^2, a third structure function, $F_3(x,Q^2)$ is required, which in addition to the photon also takes into account the parity violating Z^0 exchange. In the region of low Q^2 ($Q^2 \ll M_{Z^0}^2$) only photon exchange contributes. The Z^0 exchange and the interference between the Z^0 and the photon exchange can be neglected safely since the gauge boson masses enter the matrix element of the cross section by the propagator terms $1/Q^2$ and $1/(Q^2+M_{Z^0}^2)$ for the photon and Z^0 respectively.

The two structure functions $F_2(x,Q^2)$ and $F_L(x,Q^2)$ can also be expressed as a function of two independent contributions, σ_T and σ_L of the photo-absorption cross section [3]:

$$F_2(x,Q^2) = \frac{Q^2}{4\pi^2\alpha_{em}}\left[\sigma_T(x,Q^2) + \sigma_L(x,Q^2)\right], \quad (2.6)$$

and

$$F_L(x,Q^2) = \frac{Q^2}{4\pi^2\alpha_{em}}\sigma_L(x,Q^2). \quad (2.7)$$

The quantity $R(x,Q^2)$ can be defined as the ratio of longitudinally to transversely polarized photon cross sections and is given by,

$$R(x,Q^2) = \frac{\sigma_L(x,Q^2)}{\sigma_T(x,Q^2)} = \frac{F_L(x,Q^2)}{F_2(x,Q^2) - F_L(x,Q^2)}. \quad (2.8)$$

It can be seen from equation (2.8) that the condition that the transverse and longitudinal photon induced cross sections must be positive, leads to

$$0 \leq F_L \leq F_2. \quad (2.9)$$

From equation (2.9) and the fact that the F_L term appears with a proportionality factor y^2 in equation (2.5), it can be seen that the F_2 term is dominant in regions of low y, with

the F_L contribution increasing at high y. From the difference between the measured σ_r and the (from low y) extrapolated F_2, $F_L(x, Q^2)$ is determined as described in [4], [5].

Another way of looking at the total cross section, $\sigma_{tot} = \sigma_T + \sigma_L$, is by describing it as a convolution of a flux of quasi-real or virtual gauge bosons from the electron with the absorption cross section of that boson by the proton as depicted in figure 2.2. At small enough Q^2, the Z^0 and $W^{\pm}$ exchange can be neglected and the boson can be interpreted as a virtual photon. This massive spin 1 particle acquires three polarization vectors corresponding to the three helicity states of the photon, $\lambda = \pm 1, 0$. The absorption cross section may than depend on the helicity. We will thus have two independent cross sections, one for absorbing a transversely polarized photon σ_T ($\lambda = \pm 1$) and one for a longitudinally polarized photon σ_L ($\lambda = 0$). The differential cross section can then be written in the form:

$$\frac{d^2\sigma(ep)}{d\ W\ d\ Q^2} = f_{\gamma/e}(\sigma_T^{\gamma p} + \epsilon\sigma_L^{\gamma p}) \tag{2.10}$$

where W represents the γp centre of mass energy, $f_{\gamma/e}$ the flux factor of virtual photons and $\epsilon = \frac{2(1-y)}{1+(1-y)^2}$ the ratio of the flux for longitudinal to transverse photons.

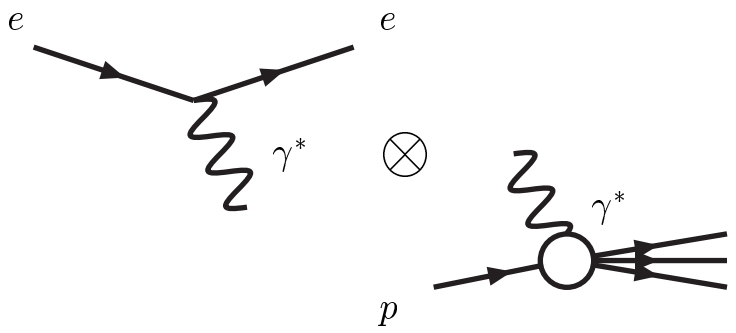

Figure 2.2: *At small Q^2, ep-scattering can be thought of as a radiation of a virtual photon γ^* from the electron, followed by $\gamma^* p$-scattering.*

2.2.1 The Quark Parton Model (QPM) and the scaling violation

The first DIS experiments at SLAC [9, 10] in the early sixties showed that the structure function $F_2(x, Q^2)$ exhibited a scaling behavior in the limit $Q^2 \to \infty$ predicted by Bjorken [6]:

$$F_2(x, Q^2) \to F_2(x). \tag{2.11}$$

In the quark parton model (QPM) [6, 7, 8], in which the proton is considered to be made of point-like charged quarks, the structure function F_2 is expected to be independent of Q^2 and is related to the parton momentum distributions $f_i(x)$ of flavor i by

$$F_2(x, Q^2) = \sum_i e_i^2\ x f_i(x) \tag{2.12}$$

where e_i is the electric charge of parton i. In the QPM, for spin-1/2 partons, $R = 0$ [3], implying that $\sigma_L(x) = F_L(x) = 0$. The parton distributions $f_i(x)$ are constrained by the sum-rule:

$$\sum_i \int x f_i(x) dx = 1, \tag{2.13}$$

where the summation runs over all species of charged partons. However measurements showed that this sum-rule is not fulfilled and that quarks and anti-quarks account for only half of the proton's momentum [15],[16]. Observation at fixed target experiments [11, 12, 13] later verified by HERA [14], showed that the scaling behavior is applicable for values of $x \approx 0.13$, but outside this x-region a weak logarithmic dependence on Q^2 is observed, implying a violation of the scaling hypothesis. The QPM is only a zeroth order description for the deep inelastic scattering process. The partons in the proton or more generally in the hadron, are not free objects and they interact with each other via a color field mediated by gluons. The theory that describes the interactions of quarks and gluons is called *Quantum ChromoDynamics* (QCD).

The scaling violations, observed in figure 2.4, which is an F_2-compilation of the most up to date measurements [17, 18, 5, 19, 20, 12, 21, 11], can be explained by considering processes of the type depicted in figure 2.3. The result of this is that for instance the quark distribution becomes scale dependent and satisfies the integro differential equation

$$\frac{dq(x,Q^2)}{d\ln Q^2} = \frac{\alpha_s(Q^2)}{2\pi} \int_x^1 \frac{dy}{y} q(y,Q^2) P_{qq}\left(\frac{x}{y}\right) \tag{2.14}$$

which is one of the DGLAP (Dokshitzer, Gribov, Lipatov, Altarelli and Parisi) [22] evolution equations. The splitting function $P_{qq}(x/y)$ represents the probability for a quark to emit another quark with momentum fraction x and can be expanded as a power series in α_s:

$$P_{qq}(x/y) = \sum_n \alpha_s^n \, p^{(n)}(x/y). \tag{2.15}$$

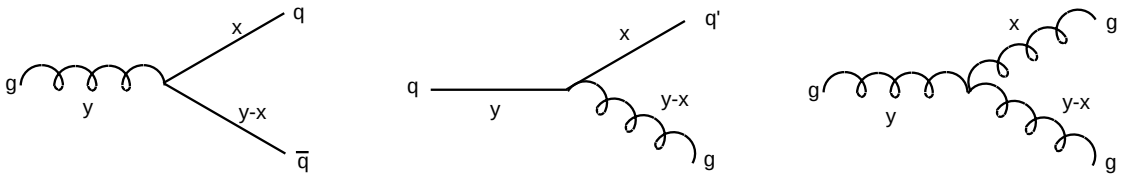

Figure 2.3: *The three different splitting functions $P_{ij}(x/y)$ of first order in α_s are shown.*

Not only the quarks but also the gluon distributions evolves, such that the full DGLAP equation becomes:

$$\frac{dq(x,Q^2)}{d\,\ln Q^2} = \frac{\alpha_s(Q^2)}{2\pi} \int_x^1 \frac{dy}{y} \left(q(y,Q^2) P_{qq}\left(\frac{x}{y}\right) + g(y,Q^2) P_{qg}\left(\frac{x}{y}\right) \right) \tag{2.16}$$

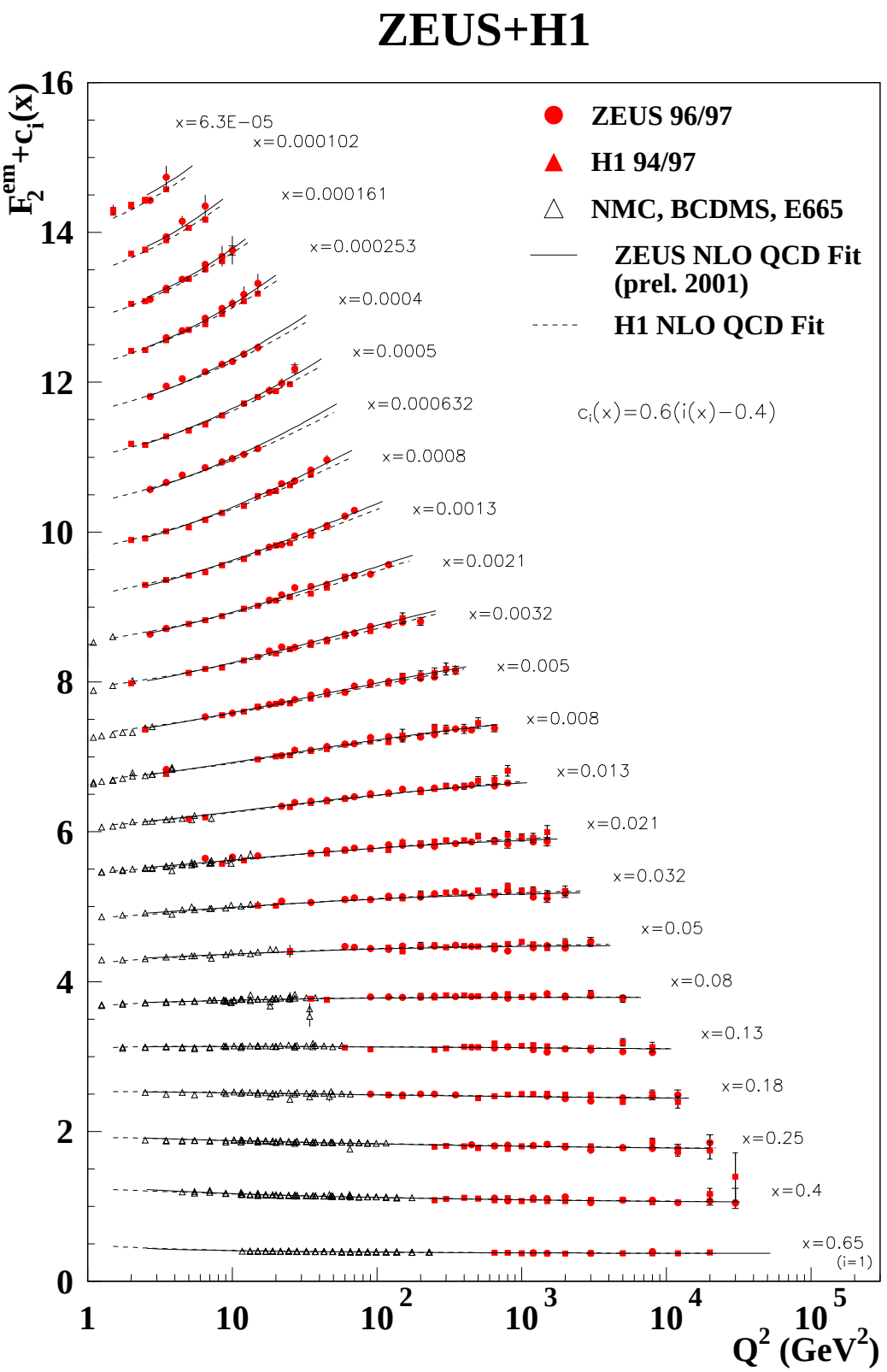

Figure 2.4: *F_2 is plotted versus Q^2 for fixed x values for the HERA data, as well as for the fixed target data. F_2 shows strong scaling violations particularly at small x.*

$$\frac{dg(x,Q^2)}{d\,\ln Q^2} = \frac{\alpha_s(Q^2)}{2\pi}\int_x^1 \frac{dy}{y}\left(\sum_q q(y,Q^2)P_{gq}\left(\frac{x}{y}\right) + g(y,Q^2)P_{gg}\left(\frac{x}{y}\right)\right) \quad (2.17)$$

where y is the momentum of the emitting parton and x is the fractional momentum of the resulting parton as illustrated in figure 2.3.

In leading order (LO), the DGLAP equation resums all contributions of the type $(\alpha_s\ \ln Q^2)^n$ and the actual gauge corresponds to the emission of a chain of n gluons with strongly transverse ordering:

$$Q^2 \gg k_{T,n}^2 \gg k_{T,n-1}^2 \gg ... \gg k_{T,1}^2 \gg Q_0^2, \quad (2.18)$$

and also weaker ordering of longitudinal momenta,

$$x < x_n < x_{n-1} < ... < x_1. \quad (2.19)$$

In the next-to-leading order (NLO) also terms of the type $\alpha_s^n\ (\ln Q^2)^{(n-1)}$ are resummed. In fits to structure function measurements, the parton density functions $q_i(x,Q^2)$ and $g(x,Q^2)$, which are inherently non-perturbative, are parameterized at a starting scale Q_0^2. The equations (2.16) and (2.17) can be used to predict the parton distributions at any other value of Q^2. An example of the gluon distribution obtained at NLO is shown for three different values of Q^2 in figure 2.5 [5]. The gluon contribution is dominant at the lowest values of x.

The large centre of mass energy at HERA, not only may result in a large Q^2 but also in a large $1/x \propto ys/Q^2$-value. This means that not only leading log in Q^2 may be important but also those in $\alpha_s\ \ln(1/x)$. A resummation of those terms not coupled to large $\ln(Q^2)$ leads to the BFKL (Balitsky, Fadin, Kuraev, Lipatov) [23] formalism. In contrast to the DGLAP approximation there is a strong ordering of longitudinal momentum fractions,

$$x \ll x_n \ll x_{n-1} \ll ... \ll x_1, \quad (2.20)$$

and no ordering of k_T.

To date the DGLAP evolution scheme alone can describe structure function data throughout the entire HERA phase space. Hence, so far there is no unambiguous evidence for the need for BFKL contributions. Figure 2.6 shows the kinematical plane in x and Q^2, illustrating the regions of validity for both formalisms.

2.3 Diffractive scattering

One of the surprises that came along with the first results from HERA was the observation of DIS events with a large rapidity gap in the hadronic final state, located between the photon and proton fragmentation regions [31, 32]. The observed fraction of events with large rapidity gaps is of the order of 10%, fairly independent of the γp centre of mass energy, W, and the photon virtuality squared, Q^2. In QCD, the fragmentation process driven by parton radiation leads to an exponential suppression of large rapidity gaps between hadrons [33]. Large rapidity gap formation, with little dependence on W, is typical of diffractive

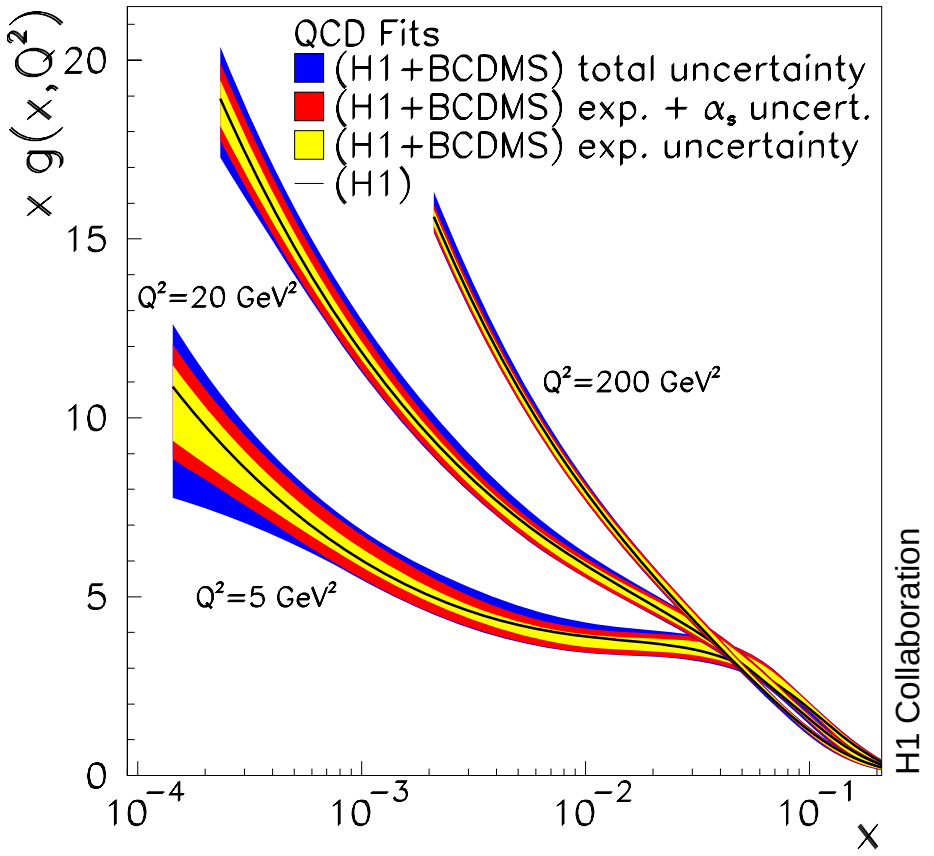

Figure 2.5: *The gluon distribution from next-to-leading order (NLO) DGLAP fits with starting scale* $Q_0^2 = 4.0\ GeV^2$.

scattering and invokes the notion of the pomeron. The fact that the diffractive exchange can be probed with large virtual photons means that its structure can be studied in much the same way as the partonic structure of the proton. The large range of the photon virtuality available at HERA opened the possibility to measure precisely the partonic structure of the diffractive exchange (see section 2.4).

At HERA, one usually identifies three types of interactions that differ in the characteristics of the final states. In elastic scattering, both initial particles emerge relatively unscathed and no other particles are produced. A diagram of the reaction $\gamma p \to Vp$ where V is any vector meson, may be considered in the framework of the VDM model [34], in which the photon is considered to consist of a two component state (i.e a part interacting only electro-magnetically and a hadronic part undergoing conventional strong interactions) to be elastic. Such an elastic (EL) γp reaction is shown in figure 2.7.a. In diffractive scattering, the energy transfer between the two interacting particles remains small, but one (single dissociation, i.e. gamma (GD) or proton dissociation (PD)) or both (double dissociation

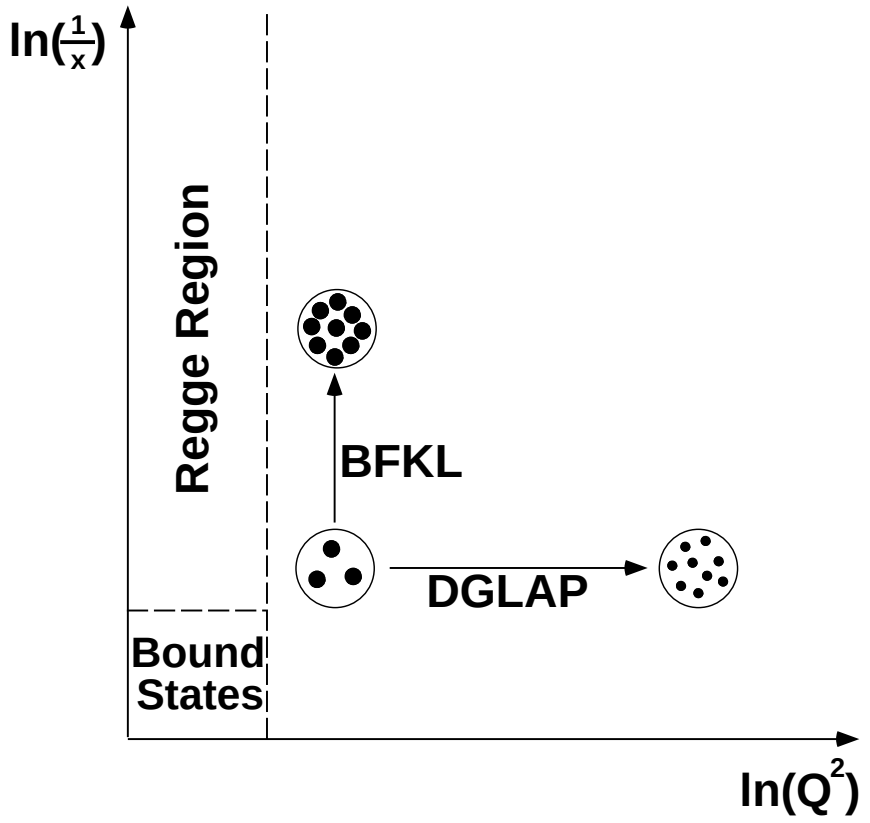

Figure 2.6: *The kinematic plane in x and Q^2 showing where the DGLAP and BFKL approximations are theoretically valid.*

(DD)) particles dissociate into multiparticle final states preserving the quantum numbers of the initial particle. Figures 2.7.b-d show the three distinct classes of dissociative diffraction that can occur with single pomeron exchange in γp-collisions. The remaining configurations correspond to so called inelastic interactions which in contrast with the elastic and diffractive scatterings show no large rapidity gaps in the final state.

Characteristic of high energy elastic and diffractive scattering is the exponential behavior of the cross section as a function of the square of the momentum transfer t. As this property is reminiscent of the diffraction of light by a circular aperture, diffractive scattering in strong interactions derives its name from the optical analogy [35]. The slope of the t-distribution will be linked with the radius of the interacting object in the following section.

Defining in an unique way what diffraction is, is very hard. But to get an idea how a single diffractive scattering can come true, two constraints have to be valid:

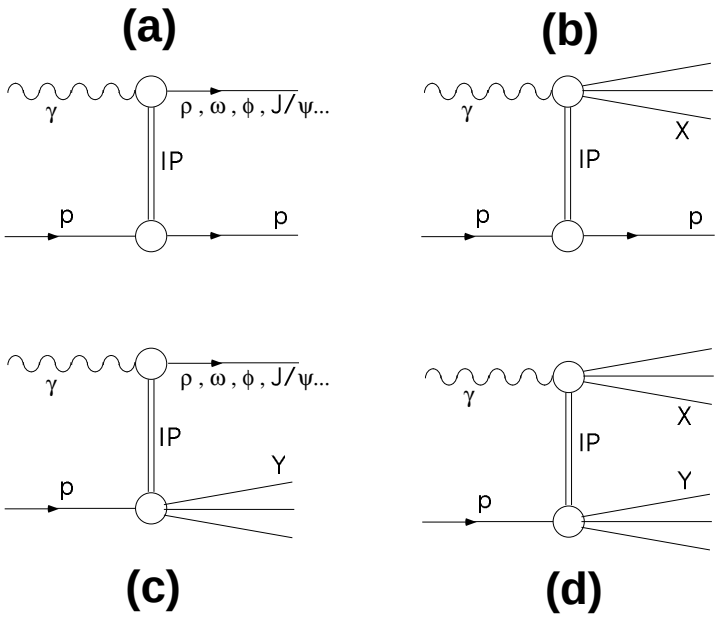

Figure 2.7: *Diffractive interactions proceeding by single pomeron exchange, occurring in γp-collisions. Figure a) represents the EL process, b) the GD process, c) the PD process and d) the DD process. The symbol $I\!P$ is used to denote the exchange of the leading pomeron trajectory.*

- **conservation of intrinsic quantum numbers of the initial state**
  The diffractive state preserves the intrinsic quantum numbers of the initial particles. However spin and parity can be changed since the momentum transfer of the interaction may change the internal motion of the interacting hadrons.

- **coherence constraint**
  The absorbing hadron should preserve its identity, which limits the invariant mass of the diffracted state. The minimum momentum transfer squared for a particle of mass m and momentum p to create a mass M_X via the interaction with a stationary target is

$$\mid t_{min} \mid = \left(\frac{M_X^2 - m^2}{2p} \right)^2 . \tag{2.21}$$

  Using the uncertainty principle, the coherence of the absorbing hadron of radius R will be preserved if

$$(M_X^2 - m^2) \leq \frac{2p}{R}. \tag{2.22}$$

Hence, when studying diffractive events, the study of low momentum transfer is especially of great interest [36, 39, 37]. In the pre QCD era these events have been successfully described in the framework of Regge-theory [38] which is based on the S-matrix formalism, in which scattering processes are described in terms of the exchange of reggeons. This Regge framework will be described below.

2.3.1 Diffractive scattering linking with optical diffraction

In figure 2.8 the cross section for elastic proton-proton scattering is plotted for different centre of mass energies as a function of $\mid t \mid$ where t is the squared momentum transfer between the two hadrons. For low centre of mass energies a falling cross section is observed where the slope gets steeper towards higher centre of mass energies. In addition a minimum and a maximum appear. This shape of the cross section down to the first minimum can be approximated by an exponential function of the form:

$$\frac{d\sigma/dt}{(d\sigma/dt)_{t=0}} = e^{bt} \approx 1 - b(p\theta)^2 \tag{2.23}$$

with $b \sim 10$ GeV^{-2}.

The data can be interpreted in the spirit of the similarity between optical and hadronic diffraction [39]. In this picture one discusses the scattering of a fast hadron represented by a plane wave in the field of a hadron at rest. In optical diffraction the following formula holds for $kR \ll 1$:

$$\frac{I}{I_0} \approx 1 - \frac{R^2}{4}(k\theta)^2 \tag{2.24}$$

which describes the fraction of observed intensity with respect to the initial intensity as a function of the diffraction angle θ, where R is the radius of the disc and k denotes the wave number of the incident light wave. If one relates the scattering angle θ to the momentum transfer t in hadron-hadron interactions, the wave number k to the momentum of the hadrons, and the radius of the disc R to the mass of the pion one can deduce a t-slope of $b = 12.5$ GeV^{-2} resulting in the right order of magnitude as the one measured.

2.3.2 The S-matrix and aspects of Regge theory

In the study of hadron-hadron interactions at low momentum transfer t, where no hard scale is present and perturbative QCD is not applicable, the phenomenological models very often still give the best descriptions available. A consistent description of such strong interactions is offered by Regge theory.

Regge theory was introduced in the framework of non-relativistic quantum mechanics and generalized the ideas of Yukawa explaining particle interactions by the exchange of virtual particles. Later it was generalized to describe also relativistic particle interactions.

Since Regge theory is based on the S-matrix formalism we will first briefly introduce the basic assumptions:

- **Unitarity of S**
  The scattering matrix is unitary, which means that the probability that there will be some final state starting from any given state $\mid i\rangle$ must be unity and is expressed as:

$$S^\dagger S = 1 = S S^\dagger \tag{2.25}$$

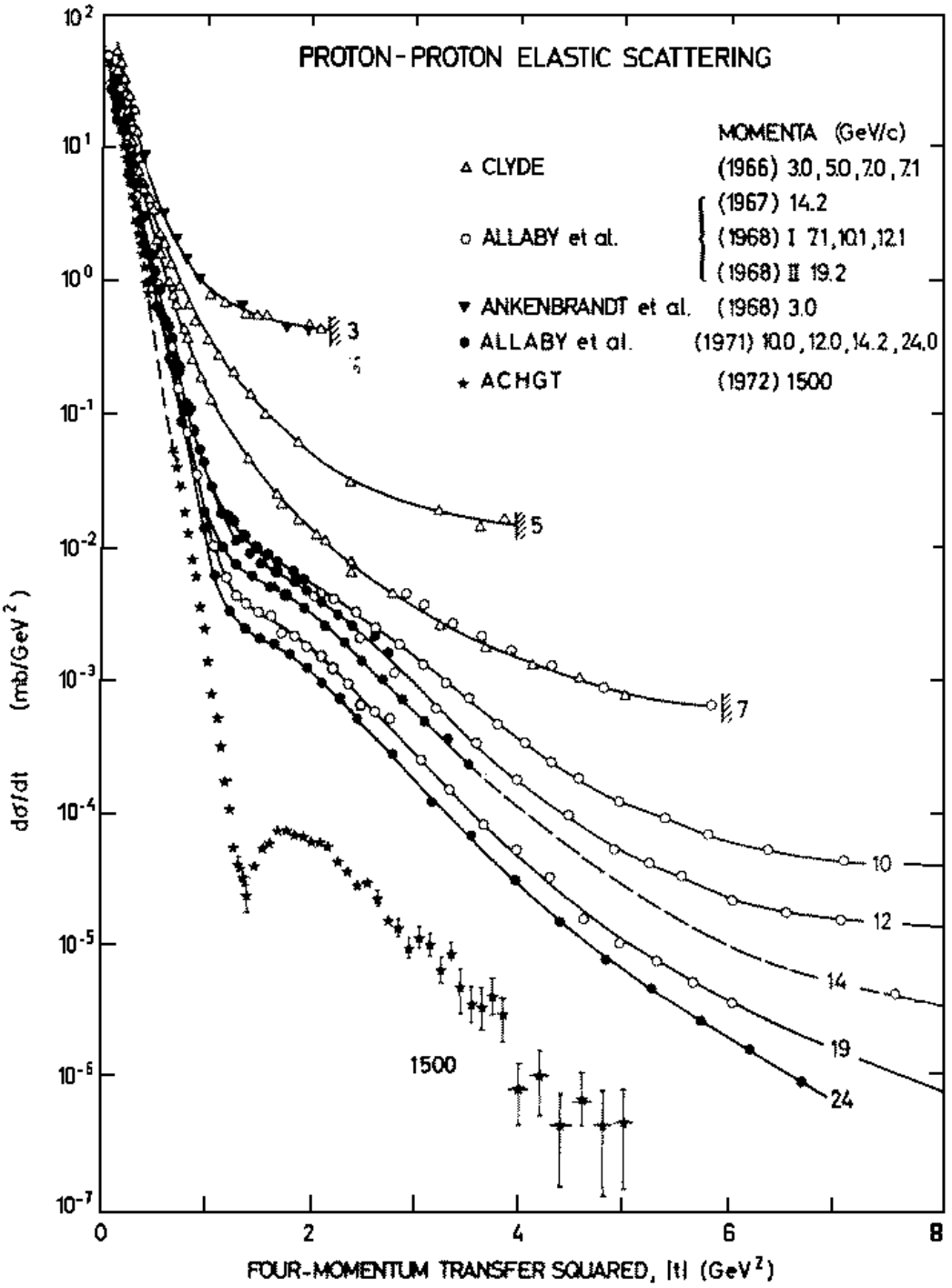

Figure 2.8: *Proton-proton elastic differential cross section versus four-momentum transfer squared at various incident proton momenta. As the energy increases, a classical diffraction pattern as in optical diffraction appears.*

- **Maximal analyticity**
  If one considers the reaction $A + B \rightarrow C + D$, the Mandelstam variables are real numbers defined by relations of the form $s_{ij} = (\pm P_i \pm P_j)^2$ with $i, j \in \{A, B, C, D\}$. Maximal analyticity of first order means that these variables can be extended into the complex plane which allows the use of complex analysis. The S-matrix can now be written as a function of these complex numbers. In the limit of real numbers one gets back the S-matrix for particle reactions in the physical region.

- **Crossing symmetry**
  A consequence of the maximal analyticity assumption is the crossing symmetry which states that if the reaction $A+B \rightarrow C+D$ is described by the variable $s = (P_A+P_B)^2$ and $t = (P_A - P_C)^2$ by the S-matrix $S(s,t)$ one can calculate the amplitude for the reaction $A+\overline{C} \rightarrow \overline{B}+D$ by exchange of s and t which leads to the amplitude $S(t,s)$ i.e.
  $$S_{AB\rightarrow CD}(s,t) = S_{A\overline{C}\rightarrow \overline{B}D}(t,s). \tag{2.26}$$

- **Generalization of angular momentum in the complex plane**
  In the s-channel, all the possible resonances which can be produced by the interaction of A and B and which conserve quantum numbers (parity, charge etc.) are linked by a linear trajectory in a two-dimensional space defined by mass squared and angular momentum. In Regge theory, angular momentum is treated as a continuous complex variable, $\alpha(t)$, with physically observable t-channel resonances occurring only at physical values of spin, such that $\mathcal{R}e(\alpha(t))$ is an integer or half integer, known as Regge poles. Stable hadrons have pure real values of $\alpha(t)$, whilst unstable hadrons have an imaginary component that is related to their decay width. Bound states therefore lie near to the real axis of $\alpha(t)$. The linear trajectories can be parameterized as:
  $$\alpha(t) = \alpha(0) + \alpha' t. \tag{2.27}$$
  As an example, the trajectory for which the ρ meson is the lowest lying state is shown in figure 2.9.

Amplitudes in the t-channel may be computed by decomposition into partial waves of different angular momenta

$$A(s,t) = \sum_{l=0}^{\infty} (2l+1)\, A_l(t)\, P_l(\cos\theta) \tag{2.28}$$

where $A_l(t)$ is the amplitude of the l^{th} partial wave, and $P_l(\cos\theta)$ is the Legendre polynomial for angular momentum l. In continuing the amplitude to describe the s-channel, where $\cos\theta > 1$, equation (2.28) may be re-expressed as a sum over poles. When expressed in terms of contributing Regge trajectories, the pole in the l^{th} partial wave may be written as [38]

$$A_l(t) = \frac{\beta(t)}{l - \alpha_l(t)}. \tag{2.29}$$

At $l = \alpha_l(t)$ a Regge pole occurs with a residue function described by $\beta(t)$.

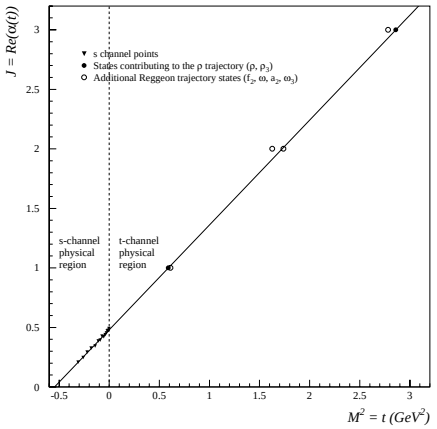

Figure 2.9: *The ρ trajectory, $\alpha_\rho(t)$. The data shown with triangles at negative t are measured in the charge exchange reaction, $\pi^- p \to \pi^0 n$, and are taken from [40]. In the t-channel physical region the bound states (ρ, ρ_3) are shown. A straight line through these states is continued into the s-channel region. The comparison there with the measured hadron-hadron data is remarkable.*

In the asymptotic limit where $s \to \infty$ and $t/s \to 0$, only the leading trajectory contributes and equation (2.28) becomes:

$$A(s,t) = f(t) \left(\frac{s}{s_0}\right)^{\alpha(t)} \tag{2.30}$$

where $f(t)$ includes $\beta(t)$ and the part of the amplitude not depending on s. s_0 defines the energy scale on which s must be large, typically taken to be ~ 1 GeV^2. Hence, at high energies the s-dependence of the s-channel scattering amplitude is a simple power behavior.

Using the optical theorem, relating the forward scattering amplitude to the total cross section

$$\sigma_{tot} = \frac{1}{s}\mathcal{I}m(A(s,t=0)) \tag{2.31}$$

one obtains, combining equations (2.30) and (2.31), the following expression for $\sigma_{tot}(s)$

$$\sigma_{tot}(s) \propto \left(\frac{s}{s_0}\right)^{\alpha(0)-1}. \tag{2.32}$$

The measurement of the energy dependence of the cross section therefore provides access to the intercept $\alpha(0)$ of the leading trajectory. When measuring also the t-dependence (see section 2.3.3) of cross sections, the determination of the slope α' becomes possible.

2.3.3 t-dependence and shrinkage

For a process that is dominated by the exchange of a single trajectory, the expression for the differential cross section follows from equations (2.27) and (2.30) and is given by,

$$\frac{d\sigma}{dt} \propto \frac{1}{s^2} \mid A(s,t) \mid^2 \tag{2.33}$$

$$\propto F(t) \left(\frac{s}{s_0}\right)^{2(\alpha(0)-1)} \left(\frac{s}{s_0}\right)^{2\alpha' t}. \tag{2.34}$$

If the dependence of the coupling, $F(t)$, is small in t, then at large s, the t-dependence must be dominated by the final factor of equation (2.34). Since t is negative, and α' positive, $d\sigma/dt$ decreases faster as a function of t as s increases. Regge theory thus predicts that if the centre of mass energy increases the forward peak shrinks as seen experimentally in figure 2.8.

Since the fast variation of the differential cross section with t at fixed s is found experimentally to be well described at low $\mid t \mid$ by an exponential parameterization, equation (2.34) may be re-expressed as

$$\frac{d\sigma}{dt} = \left(\frac{d\sigma}{dt}\right)_{t=0} e^{bt} \tag{2.35}$$

where b, known as the slope parameter, is given by;

$$b \sim b_0 + 2\alpha' \ln\left(\frac{s}{s_0}\right) \tag{2.36}$$

and describes a logarithmic shrinkage of the forward peak with increasing centre of mass energy s.

It was observed (see figure 2.10) that the total cross section in $p\overline{p}$- and pp-interactions and later in γp-interactions, decreases with energy at low energies which is explained by Regge trajectories, whereas the rise of the cross section for high energy was not expected. To account for this rise the **pomeron** was introduced which is characterized by the quantum numbers of the vacuum. Donnachie and Landshoff parameterized this energy behavior of the total cross section by the sum of two reggeon amplitudes ($I\!P$ and $I\!R$):

$$\sigma_{tot}(s) = A_{I\!P} s^{\alpha_{I\!P}(0)-1} + A_{I\!R} s^{\alpha_{I\!R}(0)-1} \tag{2.37}$$

with $A_{I\!P}$ and $A_{I\!R}$ the normalization parameters and $\alpha_{I\!P}(0)$ and $\alpha_{I\!R}(0)$ the trajectory intercepts also left as free parameters. To account for the rising cross section at high energies the pomeron intercept in equation (2.37) had to be larger than one. The fit of equation (2.37) to the $p\overline{p}$- and pp-data (see figure 2.10.a) results in,

$$\alpha_{I\!P}(0) = 1 + \epsilon = 1.08 \tag{2.38}$$

$$\alpha_{I\!R}(0) = 0.55. \tag{2.39}$$

Assuming $I\!P/I\!R$-universality, the intercepts were fixed to the values obtained from the fit on the $p\overline{p}$- and pp-data, and a new fit was performed on $\pi^- p$-, and $\pi^+ p$-data (see figure 2.10.b))

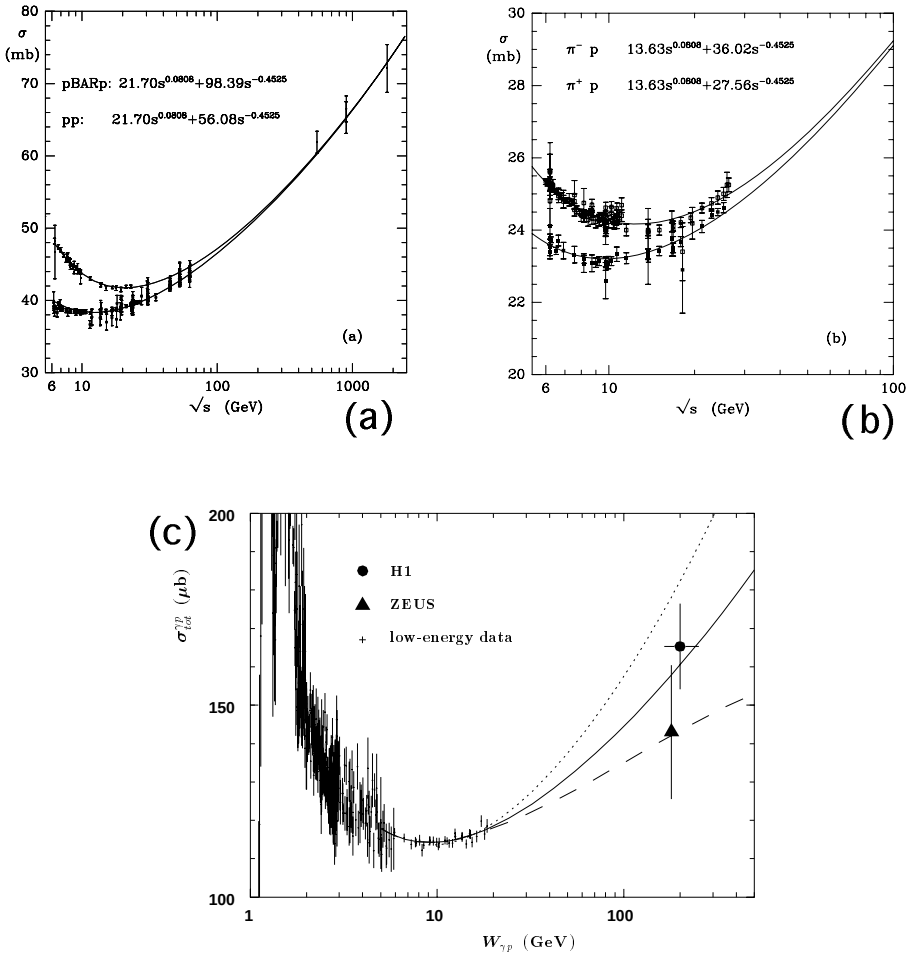

Figure 2.10: *Fits performed by Donnachie and Landshoff to the centre of mass energy dependence of the total cross section for a) pp-and $p\overline{p}$-scattering [41], b) $\pi^- p$ and $\pi^+ p$ scattering [41], and c) γp-scattering [42]. The high s points in the $p\overline{p}$ case are from the Tevatron. Those in the γp case are from HERA. In c) the solid line is the Donnachie Landshoff fit with $\alpha_{I\!P}(0) = 1.08$, the dotted line with $\alpha_{I\!P}(0) = 1.11$, whilst the broad dashed curve represents the ALLM parameterization [43].*

and γp-data (see figure 2.10.c)) leaving only the normalizations free in the fit. The reggeon has the larger coupling to hadrons, and consequently dominates at low centre of mass energies. However, the reggeon contribution falls approximately as $s^{-1/2}$, such that at large centre of mass energies, the pomeron term ($\propto s^{0.08}$) dominates, and the cross section starts to rise slowly with s. At large centre of mass energies, the coupling strength to particle and anti-particle are observed to become the same leading to similar cross sections for particle-particle interactions with respect to particle-anti-particle interactions, in accordance with the Pomerancuk theorem.

Assuming an s-dependence of the slope b as given by equation (2.36) in the $\overline{p}p$ elastic scattering data at the Tevatron Collider and the CERN ISR data, yields a value of the pomeron slope of $\alpha'_{I\!P} = 0.26 \pm 0.02$ GeV^{-2} [44]. The pomeron trajectory takes thus the form:

$$\alpha_{I\!P}(t) = 1.08 + 0.26\ t. \tag{2.40}$$

2.4 Diffraction in DIS

Where, in the region of inclusive deep inelastic scattering at high Q^2 a hard scale is present, suitable to resolve the partonic content of the proton, here in diffractive scatterings, this hard scale can be used in resolving the partonic content of the pomeron. This analogy leads to the Ingelmann-Schlein approach [45], that the diffractive deep inelastic scattering in γp-interactions proceeds in two steps as depicted in figure 2.11: first a pomeron is emitted from the proton and then the virtual photon is absorbed by a constituent of the pomeron. In order to describe this process new variables are introduced, in addition to the inclusive

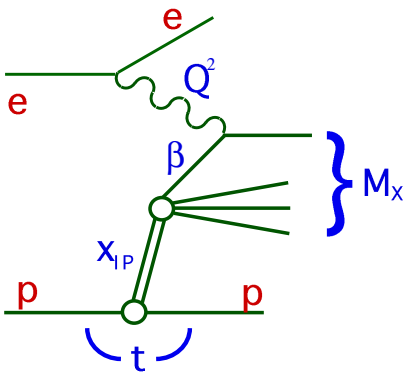

Figure 2.11: *Pictorial representation of the common diffractive variables.*

DIS variables from section 2.1. Defining the total γp centre of mass energy, the invariant mass of system X, and momentum transfer to the scattered proton respectively as:

$$W^2 \quad = \quad (q + P)^2 \tag{2.41}$$

$$M_X^2 = (q + P - P')^2 \tag{2.42}$$
$$t = (P - P')^2. \tag{2.43}$$

The variable $x_{I\!P}$ which represents the momentum fraction of the proton carried by the pomeron defined as

$$x_{I\!P} = \frac{q.(P - P')}{q.P} \tag{2.44}$$

can be rewritten as

$$x_{I\!P} = \frac{M_X^2 + Q^2 - t}{W^2 + Q^2 - m_p^2} \simeq \frac{M_X^2 + Q^2}{W^2 + Q^2} \tag{2.45}$$

where P and P' denote respectively the initial and final four-momenta of the proton and where m_p stands for the mass of the proton. The last relation on the right-hand side holds for $m_p^2 \ll Q^2,\ W^2$ and $\mid t \mid \ll Q^2,\ M_X^2$ which is a good approximation in the kinematical region of high energy diffraction at HERA.

Since the deep inelastic scattering can now be interpreted to take place on the pomeron, one can define an equivalent variable as Bjorken x but now relative to the pomeron momentum instead of the proton momentum. This variable called β, representing the fraction of the four-momentum of the pomeron carried by the struck quark, is given by,

$$\beta = \frac{Q^2}{2q.(P - P')} = \frac{x}{x_{I\!P}} = \frac{Q^2}{Q^2 + M_X^2 - t} \simeq \frac{Q^2}{Q^2 + M_X^2}. \tag{2.46}$$

2.4.1 Diffractive structure function

Analogous to the inclusive DIS cross section (see section 2.2), the diffractive DIS cross section can be written, after integration over t, as a three fold differential cross section depending on $x_{I\!P},\ \beta$, andQ^2 [48],

$$\frac{d\sigma^D(ep \to epX)}{d\beta\ dQ^2\ dx_{I\!P}\ dt} = \frac{4\pi\alpha_{em}^2}{\beta Q^4}\left(1 - y + \frac{y^2}{2}\right)\sigma_r^{D(3)}(\beta, Q^2, x_{I\!P}, t). \tag{2.47}$$

In the region, $Q^2 \ll M_{Z^0}^0$, where contributions from Z^0 exchange can be neglected, $\sigma_r^{D(3)}$ is related to the diffractive structure functions $F_2^{D(3)}$ and $F_L^{D(3)}$ by,

$$\sigma_r^{D(3)} = F_2^{D(3)} - \frac{y^2}{1 + (1 - y)^2}F_L^{D(3)} \tag{2.48}$$

where F_L^D is the longitudinal diffractive structure function. Also here the positivity constraint on the cross sections for longitudinally and transversely polarized photon scattering leads to the relation $0 \leq F_L^D \leq F_2^D$. The contribution of F_L^D to $\sigma_r^{D(3)}$ can be sizeable only at large values of y, and in most of the kinematic range the relation $\sigma_r^{D(3)} \approx F_2^D$ holds to good approximation. In contrast to the inclusive deep inelastic scattering were F_L is measured in the range of large y, F_L^D is not yet measured in diffractive scattering interactions.

QCD hard scattering factorization in diffraction

The proof that QCD hard scattering factorization can be applied to diffractive DIS [46] implies that in the leading $\log(Q^2)$ approximation, the cross section for the diffractive process $\gamma^\star p \to XY$ can be written in terms of convolutions of universal partonic cross sections $\sigma^{\gamma^\star i}$ with diffractive parton distributions F_i^D [47], representing probability distributions for a parton i in the proton under the constraint that the proton is scattered with particular values of t and $x_{I\!P}$. Thus, at leading twist,

$$\frac{d^2\sigma(x,Q^2,x_{I\!P},t)^{\gamma^\star p\to p'X}}{dx_{I\!P}\,dt} = \sum_i \int_x^{x_{I\!P}} d\xi\ \sigma^{\gamma^\star i}(x,Q^2,\xi)\ f_i^D(\xi,Q^2,x_{I\!P},t). \tag{2.49}$$

The factorization formula is valid for large enough Q^2 and fixed $x_{I\!P}$ and t. The partonic cross sections $\sigma^{\gamma^\star i}$ are the same as those for inclusive DIS and the diffractive parton distributions f_i^D, which are not known from first principle, should obey the DGLAP evolution equations.

Regge factorization

An additional assumption is often made in the analysis of diffractive cross sections, saying that the shape of the diffractive parton distribution is independent of $x_{I\!P}$ and t and that their normalization is controlled by Regge asymptotics [45]. The diffractive parton distributions can then be factored into a term depending only on $x_{I\!P}$ and t and a second term depending only on β and Q^2 (see figure 2.12):

$$f_i^D(x_{I\!P},t,\beta,Q^2) = f_{I\!P/p}(x_{I\!P},t).f_i^{I\!P}(\beta,Q^2). \tag{2.50}$$

Under this Regge factorization assumption, often refered to in the literature as the Ingelman-Schlein or resolved pomeron model, the diffractive exchange can be treated as a quasi-real object with a partonic structure, given by parton distributions $f_i^{I\!P}(\beta,Q^2)$. The variable β then corresponds to the longitudinal momentum fraction of the diffractive exchange carried by the struck parton in the pomeron. The pomeron flux factor $f_{I\!P/p}(x_{I\!P},t)$ represents the probability that a pomeron with particular values of $x_{I\!P}$ and t couples to the proton. Although equation (2.50) has no firm basis in QCD, at the present level of precision it appears to be supported by data [48, 49, 50].

Figure 2.13 show the $x_{I\!P}$-dependence of the measured diffractive reduced cross section $\sigma_r^{D(3)}(\beta,Q^2,x_{I\!P})$ [51] for fixed β and Q^2 respectively, using a parameterization of the form

$$\sigma_r^{D(3)}(x_{I\!P},\beta,Q^2) = f_{I\!P}(x_{I\!P})A_{I\!P}(\beta,Q^2) + f_{I\!R}(x_{I\!P})A_{I\!R}(\beta,Q^2) \tag{2.51}$$

where the pomeron and reggeon flux factors are defined as

$$f_{\{I\!P,I\!R\}}(x_{I\!P}) = \int_{t_{cut}}^{t_{min}} \frac{e^{B_{\{I\!P,I\!R\}}t}}{x_{I\!P}^{2\alpha_{\{I\!P,I\!R\}}(t)-1}}\,dt \tag{2.52}$$

where the pomeron and reggeon trajectories are assumed to be linear. The free parameters in the fit are $\alpha_{I\!P}(0)$, $A_{I\!P}(\beta,Q^2)$ and $A_{I\!R}(\beta,Q^2)$. A striking feature of the data presented

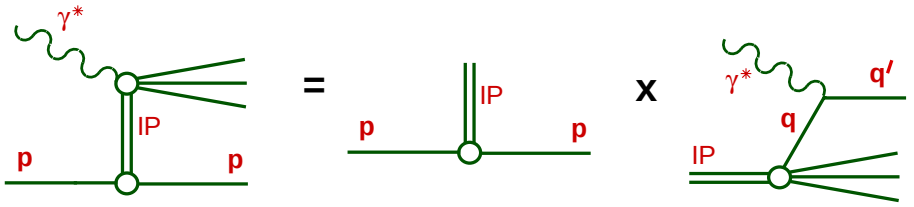

Figure 2.12: *Representation of the Regge factorization assumption.*

in [51], is the scaling violations with positive $\partial\sigma_r^{D(3)}/\partial \ln Q^2$ throughout most of the phase space, becoming negative only at the highest measured values of β. This behavior is different from that observed for the scaling violation of $F_2(x, Q^2)$ at fixed x, which is negative for $x \geq 0.1$. In a QCD interpretation, this means that the measured Q^2-dependences are strongly suggestive of a large gluonic component of the diffractive exchange.

In order to investigate whether $\alpha_{I\!P}(0)$ has any dependence on Q^2, the fits were performed in different Q^2-intervals. Those results of the pomeron intercepts are shown in figure 6.7 at $Q^2 > 0$ GeV^2 with some values of the pomeron intercept extracted in this thesis at $Q^2 = 0$ GeV^2.

2.5 Diffractive dissociation in photoproduction

Returning back to the low Q^2-region of soft physics, where no QCD predictions exist, Regge theory offers predictions in terms of trajectories for the dynamics of dissociative diffraction, and of inclusive processes in general. Feynman [53] predicted that high energy inclusive reactions of the type

$$A + B \to C + X$$

where C is the observed particle and X represents everything else produced, should scale in analogy to Bjorken scaling in DIS, such that cross sections should be function of the transverse and longitudinal momenta of the particle C, but not of the centre of mass energy. An extended version of the optical theorem for such inclusive processes, depicted in figure 2.14, was proposed by Mueller [54], relating the inclusive reaction $AB \to CX$ to the theoretically much simpler three-body elastic scattering process, $AB\overline{C} \to AB\overline{C}$,

$$f \equiv E_C \frac{d\sigma}{d^3 p_C}(A + B \to C + X) \simeq \frac{1}{s}\mathrm{Disc}_{M^2} A(AB\overline{C} \to AB\overline{C}) \tag{2.53}$$

where the discontinuity is to be taken only across the M_X^2 cut of the elastic amplitude. Here M_X^2 is defined as $(P_A + P_B + P_{\overline{C}})^2$. The importance of Mueller's optical theorem is that the behavior of the inclusive reaction can be obtained from that of the theoretically much

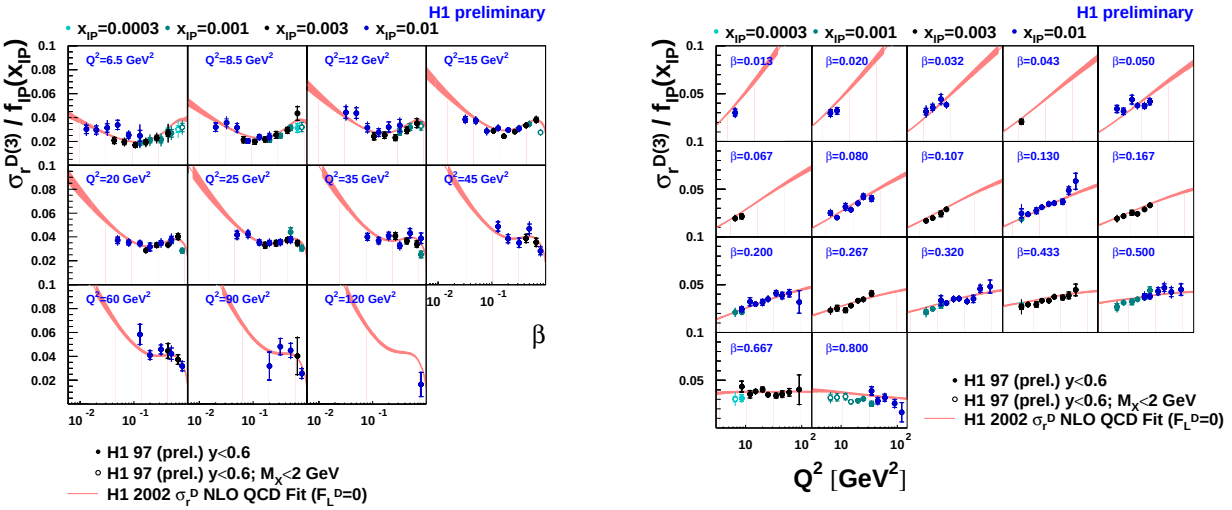

Figure 2.13: *β-dependence (left) and Q^2-dependence (right) of the reduced cross section (left) scaled at each $x_{I\!P}$ by the values assumed for the t-integrated pomeron flux in the QCD fits. Only data with $y < 0.6$ are shown to minimize the influence of the longitudinal structure function F_L^D. The data are compared with the prediction of the NLO QCD fits under the assumption that $F_L^D = 0$.*

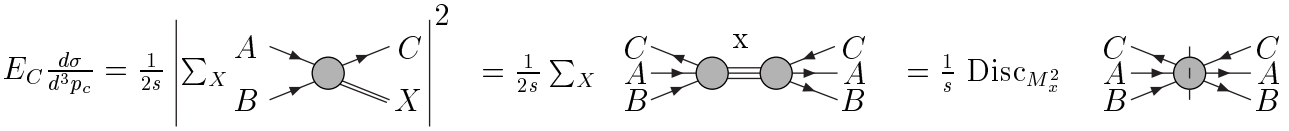

Figure 2.14: *Pictorial representation of Mueller's Optical theorem.*

simpler, elastic three-body amplitude. Much of the knowledge gained from Regge type analyses of two-body scattering was immediately carried over into the inclusive domain.

To calculate the inclusive cross section for $A+B \to C+X$ we shall assume Regge behavior for the three-body amplitude. It is necessary to distinguish between three kinematical regions for particle C, i.e. the beam and target fragmentation region and the central region. The beam and target fragmentation region corresponds to finite values of $t \equiv (p_A - p_C)^2$ and $u \equiv (p_B - p_C)^2$ respectively. Intuitively C can be regarded as a fragment of A (or B) if the momentum difference between them remains finite at large s. In the third region, i.e. the central region, where t and u are both large, C is not closely associated with either incoming particle. A general criterion for a Regge expansion of a multi particle amplitude, such as $AB\overline{C} \to AB\overline{C}$, is that the kinematic invariant spanning the Regge exchange should

be large (a typical value $\geq$ 5 GeV^2). In the central region where both t and u are large, we have the double Regge limit. On the other hand, in the beam fragmentation region ($s \to \infty$, $t/s \to 0$) there are three different Regge limits when different combinations of the invariants M_X^2 and s/M_X^2 become large.

2.5.1 The fragmentation region

Typical Regge contributions for the three different limits [38] are shown in figure 2.15.

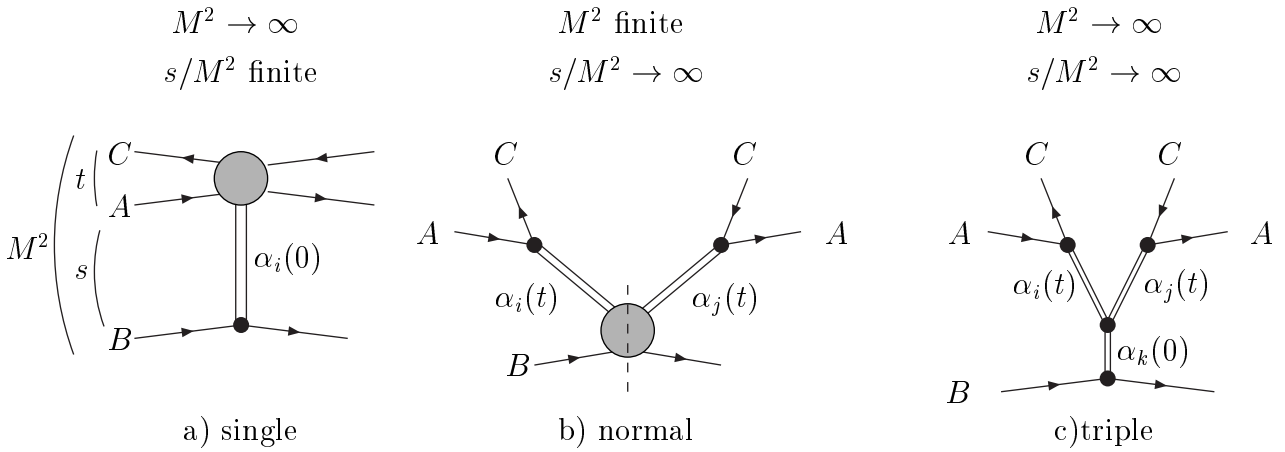

Figure 2.15: *The single, normal and triple Regge limit is depicted in the beam fragmentation region.*

1. **The single Regge limit ($s_{AB} \to \infty$ and $x_{I\!P} = M_X^2/s_{AB}$ fixed $\Rightarrow M_X^2 \to \infty$).** Since M_X^2 is the total centre of mass energy for the $AB\overline{C}$ elastic scattering process, and since large centre of mass energy (here M_X^2) and small $\mid t \mid$ suggest a single Regge pole exchange picture as in figure 2.15.a, this leads to an inclusive cross section of the form;

$$s\,\frac{d^2\sigma}{dt\,dM_X^2} = \sum_i \beta_i \left(\frac{M_X^2}{s}, t\right) \left(\frac{M_X^2}{s_0}\right)^{\alpha_i(0)-1} \tag{2.54}$$

where i runs over all possible reggeons that can be exchanged between particles A and B. Notice also that the argument of α_i is taken at $t_{BB'}$ which is for this forward three-body process always equal to 0, and should not be confused with $t \equiv t_{AC}$ which gives the invariant mass of the quasi-particle ($A\overline{C}$). Assuming the leading singularity, the pomeron, has $\alpha_{I\!P}(0) = 1$ and the leading meson exchanges have $\alpha_{I\!R}(0) = 0.5$, the inclusive cross section will scale for $M_X^2 \to \infty$. At low invariant mass reggeon contribution will go down as $(M_X^2/s_0)^{-1/2}$. The same behavior was also seen in the total cross sections as a function of the centre of mass energy s (see figure 2.10).

2. **The normal Regge limit (M_X^2 fixed , $s/M_X^2 \to \infty$).**
In this case equation (2.53) yields an inclusive cross section:

$$s\frac{d^2\sigma}{dt\, dM_X^2} = \frac{1}{s}\sum_{ij}\beta_{AC}^i(t)\beta_{AC}^j(t)\ \left(\frac{s}{M_X^2}\right)^{\alpha_i(t)+\alpha_j(t)}\ \text{Im}\ A_{(iB\to jB)}(\nu, t_{AC}, t_{BB}=0) \tag{2.55}$$

where the sum is over all contributing trajectories. β_{AC}^i are the reggeon couplings. $A_{(iB\to jB)}(\nu, t_{AC})$ is usually refered to as the forward reggeon-particle scattering amplitude with $\nu \equiv M_X^2 - t - m_p^2$ and the mass of the state X constrained to be M_X^2 as indicated by the dashed line in the middle diagram of figure 2.15.

3. **The triple Regge limit ($M_X^2 \to \infty$, $s/M_X^2 \to \infty$ or $s_{AB} \gg M_X^2 = s_{\alpha_i B} \gg t_{AC}$).**
This kinematic region is the overlap of the two preceding regions. For large M_X^2 the Reggeon-particle forward scattering amplitude of equation (2.55), which is related by Mueller's optical theorem via an intermediate state with mass M_X^2 to the Reggeon-particle cross section, can be expanded in terms of Regge exchanges in the $B\overline{B}$-channel which leads to the following triple Regge expansion:

$$\text{Im}\ A_{(iB\to jB)}(M_X^2, t) = \sum_k g_{ijk}(t)\beta_{BB}^k(0)\left(\frac{M_X^2}{s_0}\right)^{\alpha_k(0)} \tag{2.56}$$

where g_{ijk} is the triple reggeon coupling at the centre of the last diagram of figure 2.15. The overall differential cross section in the triple Regge limit is then given, from equations (2.55) and (2.56), by

$$s\frac{d^2\sigma}{dt\, dM_X^2} = \frac{1}{s}\sum_{ijk}\beta_{AC}^i(t)\beta_{AC}^j(t)\beta_{BB}^k(0)g_{ijk}(t)\ \left(\frac{s}{M_X^2}\right)^{\alpha_i(t)+\alpha_j(t)}\ \left(\frac{M_X^2}{s_0}\right)^{\alpha_k(0)} \tag{2.57}$$

2.5.2 The triple pomeron amplitude

In the asymptotic limit in which $M_X^2 \to \infty$ and $s/M_X^2 \to \infty$ only the $I\!P I\!P I\!P$ term survives and equation (2.57) reduces to the triple pomeron amplitude given by:

$$\frac{d^2\sigma}{dtdM_X^2} \simeq \frac{\beta_{AI\!P}^2(t)\beta_{BI\!P}(0)g_{I\!P I\!P I\!P}(t)}{s^2}\left(\frac{s}{M_X^2}\right)^{2\alpha_{I\!P}(t)}\left(\frac{M_X^2}{s_0}\right)^{\alpha_{I\!P}(0)}. \tag{2.58}$$

When rewriting equation (2.58) as:

$$\frac{d^2\sigma}{dtdx_{I\!P}} \simeq \beta_{AI\!P}^2(t)\beta_{BI\!P}(0)g_{I\!P I\!P I\!P}(t)\,(x_{I\!P}s)^{\alpha_{I\!P}(0)-1}\,x_{I\!P}^{(1-2\alpha_{I\!P}(t))} \tag{2.59}$$

$$\simeq \mathcal{F}_{I\!P/P}(x_{I\!P}, t)\sigma_{I\!P B}^{tot}(x_{I\!P}s, t) \tag{2.60}$$

where $x_{I\!P} \simeq M_X^2/s$ (see equation (2.44)), the pomeron flux is separated from the pomeron-particle cross section. The pomeron flux and the pomeron-particle cross section are respectively equal to:

$$\mathcal{F}_{I\!P/P}(x_{I\!P}, t) \propto \beta_{AI\!P}^2(t)x_{I\!P}^{1-2\alpha_{I\!P}(t)} \tag{2.61}$$

$$\sigma_{I\!P B}^{tot}(x_{I\!P}s, t) \propto \beta_{BI\!P}(0)g_{I\!P I\!P I\!P}(t)\,(x_{I\!P}s)^{\alpha_{I\!P}(0)-1} \tag{2.62}$$

Writing the pomeron trajectory as:

$$\alpha_{I\!P}(t) = 1 + \epsilon + \alpha'_{I\!P} t \tag{2.63}$$

the equation (2.58) becomes:

$$\frac{d^2\sigma}{dtdM_X^2} \simeq \kappa(t) s^{2\epsilon+2\alpha'_{I\!P}t} \left(\frac{1}{M_X^2}\right)^{1+\epsilon+2\alpha'_{I\!P}t} \tag{2.64}$$

where $\kappa(t)$ contains all the couplings of equation (2.58).

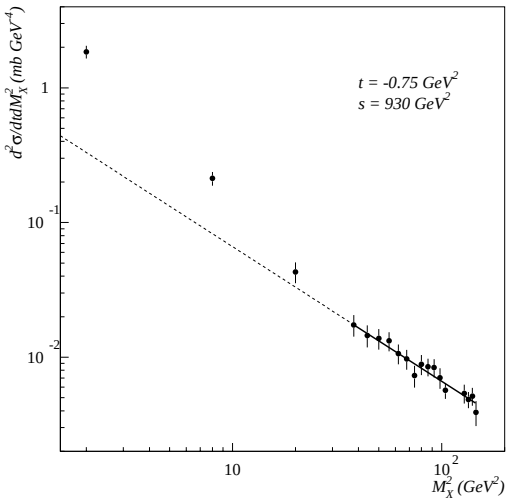

Figure 2.16: *The differential cross section for the reaction $pp \to pX$ at a centre of mass energy $s = 930\ GeV^2$ and momentum transfer $t = -0.75\ GeV^2$ [56]. The line drawn is proportional to $1/M_X^2$, which fits the data well in the triple Regge region. The dashed line is the continuation of the triple Regge region fit.*

Figure 2.16 shows a measurement of the differential cross section $d^2\sigma/dtdM_X^2$ for diffractive pp-collisions at the CERN ISR. In the triple Regge region defined by the large dissociation masses beyond the resonance region, the $1/M_X^2$-dependence is clearly observed.

2.5.3 Interference terms

Since the pomeron and the f reggeon exchange identical quantum numbers (see table 2.1) they may interfere [57, 58, 59, 60]. Such a contribution is expressed in terms of the 'non-diagonal' amplitudes $\{I\!P I\!R\}I\!P$ and $\{I\!P I\!R\}I\!R$ where,

$$\{I\!P I\!R\}k \equiv I\!P I\!R k + I\!R I\!P k. \tag{2.65}$$

Restrictions are imposed on the magnitudes of the interference relative to the non-interference terms through the Schwartz inequality [61]

$$\left(\sum_k G_{\{I\!P I\!R\}k}(t)(M_X^2)^{\alpha_k(0)}\right)^2 \leq 4\sum_k G_{I\!P I\!P k}(t)(M_X^2)^{\alpha_k(0)} \sum_k G_{I\!R I\!R k}(t)(M_X^2)^{\alpha_k(0)}. \quad (2.66)$$

Following [62, 60] two component duality can be assumed in the reggeon-photon scattering amplitude, such that the diagonal and non-diagonal terms are separately related for $k = I\!P$ and $k = I\!R$. When maximal coherence is assumed and through equation (2.66), the interference couplings at $t = 0$ GeV^2 can be parameterized as:

$$G_{\{I\!P I\!R\}I\!P}(0) = 2\sqrt{\mid G_{I\!P I\!P I\!P}(0) G_{I\!R I\!R I\!P} \mid}, \quad (2.67)$$

$$G_{\{I\!P I\!R\}I\!R}(0) = 2\sqrt{\mid G_{I\!P I\!P I\!R}(0) G_{I\!R I\!R I\!R} \mid}. \quad (2.68)$$

2.5.4 Pion exchange

At high centre of mass energies and low $x_{I\!P}$ (i.e. $x_{I\!P} < 0.03$) the diffractive cross section is dominated by pomeron exchange [50] but at $x_{I\!P} > 0.03$ reggeon exchange contribution to the diffractive structure function becomes important [63]. And especially at even higher $x_{I\!P}$ (i.e. $x_{I\!P} \geq 0.1$) pion exchange becomes important [63]. Data taken at HERA where the scattered proton is measured in the Forward Proton Spectrometers lie in this high $x_{I\!P}$-region. Since real pion-hadron scattering data exist, the pion-flux factor $\mathcal{F}_{\pi/P}$, in contrast with pomeron-hadron data, can be normalized absolutely to:

$$\mathcal{F}_{\pi/P} \propto x_\pi^{1-2\alpha_\pi(t)} \frac{-t \exp\left(b_\pi(t - m_\pi^2)\right)}{(m_\pi^2 - t)^2}, \quad (2.69)$$

so that the differential cross section for pion exchange has the following form:

$$s\frac{d^2\sigma}{dt dM_X^2} = \sum_{k=I\!P, I\!R} \frac{G_{\pi\pi k}(t)}{s}\left(\frac{s}{M_X^2}\right)^{2\alpha_\pi(t)} (M_X^2)^{\alpha_k(0)} \frac{-t \exp\left(b_\pi(t - m_\pi^2)\right)}{(m_\pi^2 - t)^2}. \quad (2.70)$$

2.6 Review of diffractive dissociation analysis.

Since all ingredients of the triple Regge model are introduced, we can come to the review of existing diffractive dissociation analysis. First the results from the reaction $pp \to Xp$ and $\overline{p}p \to Xp$ at respective pp- and $\overline{p}p$-collider experiments will be discussed, followed by a summary of the existing HERA results on this topic.

2.6.1 Fixed target and ISR results

The application of triple Regge phenomenology to inclusive diffractive final states dates back to the early seventies [64]. These first analyses used data obtained with 24 GeV/c

PID	isospin	signature	C parity	G parity
$I\!P$	0	+	+	+
f	0	+	+	+
ρ	1	-	-	+
ω	0	-	-	-
a	1	+	+	-
π	1	-	+	-
γ	0,1	-	-	/

Table 2.1: *The most relevant quantum numbers of the considered reggeons.*

incident protons and concluded that they were still far from having verified the Regge predictions in these experiments. It is only with the arrival of FNAL fixed target and ISR data at $\sqrt{s} > 20$ GeV [65] that quantitative conclusions could be drawn. Two global Regge fits by Field and Fox [57] and Roy and Roberts [61], have been performed which have been comprehensively reviewed and re-analysed by Ganguli and Roy in [66]. Various combinations of the triple Regge couplings, represented in equation (2.72), were considered, being $G_{I\!P I\!P I\!P}$, $G_{I\!P I\!P I\!R}$, $G_{I\!R I\!R I\!P}$, $G_{I\!R I\!R I\!R}$, $G_{\pi\pi I\!P}$ and $G_{\pi\pi I\!R}$. The latter two couplings were added as it was pointed out [67] that the π contribution could be sizeable (50% at $x_{I\!P} \simeq 0.83$). In order to cover a wide M^2-range very low masses had to be included. This was achieved by using the finite mass sum rules (FMSR). The triple Regge couplings resulting from the fits as a function of t are shown in table 2.2. They will be used to compare the results on the pp-data with those from γp-data, see section 2.6.2 and 6.3. The trajectories in these fits were assumed to be $\alpha_{I\!P}(t) = 1 + 0.25t$, $\alpha_{I\!R}(t) = 0.5 + t$ and $\alpha_\pi(t) = -0.02 + t$.

-t	$G_{I\!P I\!P I\!P}(t)$	$G_{I\!P I\!P I\!R}(t)$	$G_{I\!R I\!R I\!P}(t)$	$G_{I\!R I\!R I\!R}(t)$	$G_{\pi\pi I\!P}(t)$	$G_{\pi\pi I\!R}(t)$
0.05	3.80 ± 0.13	0.73 ± 0.15	44 ± 5	1 ± 10	167	259 ± 200
(0.05	4.24±0.24	0.51±0.18	15±5	27±18	619±112	21±150)
0.1	2.74 ± 0.11	1.16 ± 0.12	38 ± 5	0 ± 9	124 ± 60	0 ± 116
0.15	1.89 ± 0.08	1.13 ± 0.10	35 ± 5	15 ± 11	104 ± 62	4 ± 153
0.2	1.43 ± 0.07	0.92 ± 0.10	35 ± 4	22 ± 11	47 ± 44	0 ± 147
0.25	1.11 ± 0.24	0.94 ± 0.12	21 ± 5	41 ± 12	49 ± 45	0 ± 139
0.35	0.80 ± 0.06	0.70 ± 0.07	23 ± 5	20 ± 16	133 ± 98	0 ± 88
0.45	0.54 ± 0.03	0.47 ± 0.05	22 ± 4	46 ± 15	34 ± 56	0 ± 105
	$4.95e^{4.95t}$	0.83	$47.7e^{1.89t}$	24.4	$200.0e^{4.38t}$	30.0

Table 2.2: *Triple Regge couplings (in mb/GeV^2) for the six terms considered in the fit from Ganguli and Roy [66]. A simple exponential fit parameterizes the t-dependence.*

A fixed target experiment of importance performed at Fermilab, where incident photons were scattered on a hydrogen target, measured the diffractive dissociation cross section,

$d^2\sigma/(dtdM_X^2)$, at fixed t and at two centre of mass energies W=12.9 and 15.3 GeV [74]. In the analysis, Chapin et al., tested the FMSR and the factorization hypothesis by comparing γp-data with $\pi^- p$-data which were obtained in the same experiment. In addition an exponential behavior in t and a dominant $1/M_X^2$-behavior for $M_X^2 > 4$ GeV^2 was observed.

Those data will be combined in a triple Regge fit to the main rapidity gap data presented in this analysis and leading proton data [69] which will be introduced in section 2.6.2. By doing so the covered range in W is extended by more than one order in magnitude towards lower centre of mass energies, providing us a much larger lever-arm in W to disentangle the W-dependence.

2.6.2 HERA results

Both Collaborations at HERA (ZEUS and H1) have used two different methods to select diffractive dissociative processes. The most straightforward selection consists in tagging the scattered proton by means of a forward or leading proton spectrometer, called FPS in the case of the H1 experiment or LPS for the ZEUS experiment. The other method relies on the presence of a rapidity gap in the forward part of the detector. Both methods have their advantages and disadvantages. Generally the leading proton spectrometers measure well the proton momentum without much background resulting from dissociative processes. However because of their limited acceptance, the accumulated statistics is rather limited. Almost the reverse is true for the rapidity gap selection where the collected statistics is much larger, but because the leading proton is not tagged, background resulting from low mass proton excitation processes can be substantial. They provide complementary information in that the mass range covered by both methods differ.

Tagged leading proton data

In the case where the leading proton is tagged in the forward proton spectrometers the photon dissociative mass M_X can be measured by measuring the centre of mass energy of the photon-proton system W, by $M_X = W\sqrt{1-z}$. Here z is the energy fraction of the proton leaving the interaction, $z = E'_p/E_p$, where E'_p and E_p represent the energy of the outgoing and incoming protons respectively. The process $\gamma p \to Xp$ is interpreted in the framework of triple Regge theory depicted in figure 2.17. The similarity between figure 2.15 and 2.17 is seen, but here the picture is presented for γp-scattering. The possibility of contributions of interference terms was also neglected in figure 2.17, such that the two reggeon trajectories coupling to the proton are identical. The cross section can than be expressed as a sum over contributing Regge trajectories such that equation (2.57) becomes:

$$W^2\frac{d^2\sigma}{dtdM_X^2} = \frac{d^2\sigma}{dtdz} = \frac{s_0}{W^2}\sum_{i,k} G_{iik}(t)\left(\frac{W^2}{M_X^2}\right)^{2\alpha_i(t)}\left(\frac{M_X^2}{s_0}\right)^{\alpha_k(0)}. \tag{2.71}$$

Here α_i refers to the trajectory exchanged between the photon and the proton and α_k refers to the additional trajectory describing the total cross section between α_i and the photon. The triple Regge coupling $G_{iik}(t)$ may be factored into products of couplings $\beta_{pi}(t)$

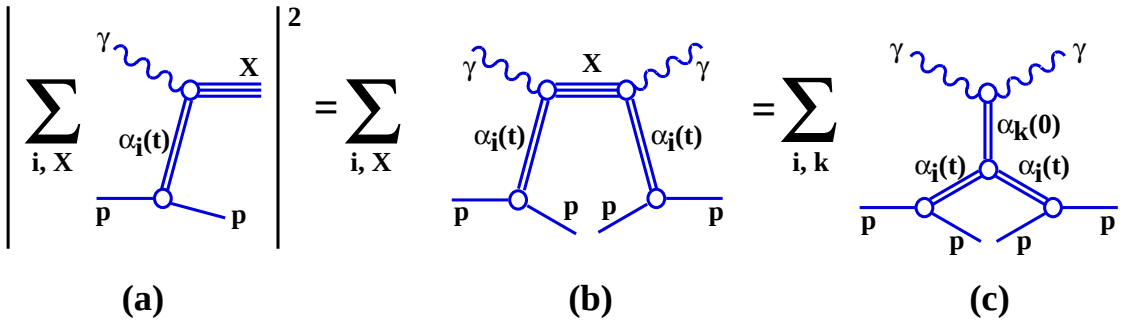

Figure 2.17: *Representation of the Mueller-Regge approach for the inclusive photon dissociative cross section.*

of trajectory i to the proton, of couplings $\beta_{\gamma k}(0)$ of trajectory k to the photon and of a triple Regge coupling $g_{iik}(t)$ as:

$$G_{iik}(t) = \frac{1}{16\pi}\beta_{pi}^2(t)\beta_{\gamma k}(0)g_{iik}(t). \tag{2.72}$$

The t-dependence of the reggeon-proton and three-reggeon couplings are parameterized here as

$$\beta_{pi}(t) = \beta_{pi}(0)e^{b_{pi}t} \tag{2.73}$$
$$g_{iik}(t) = g_{iik}(0)e^{b_{iik}t}. \tag{2.74}$$

With the three trajectories, $\alpha_{I\!P}$, $\alpha_{I\!R}$ and α_π, assuming no interference between the $I\!P$ and $I\!R$, equation (2.71) leads to a total of six terms with distinct W^2- and M_X^2-dependences. Those terms, all with their individual W^2- and M_X^2-dependences on the differential cross section $M_X^2 d\sigma/dM_X^2$ are listed in table 6.1.

In the triple Regge limit in which both $W^2/M_X^2 \to \infty$ and $M_X^2 \to \infty$ only the $iik = I\!P I\!P I\!P$ term survives and equation (2.71) reduces to

$$\frac{d^2\sigma}{dtdM_X^2} = \frac{G_{I\!P I\!P I\!P}(0)}{s_0^{\alpha_{I\!P}(0)-1}}\left(W^2\right)^{2\alpha_{I\!P}(0)-2}\left(\frac{1}{M_X^2}\right)^{\alpha_{I\!P}(0)} e^{B(W^2,M_X^2)t}, \tag{2.75}$$

where $B(W^2, M_X^2) = 2b_{pI\!P} + b_{I\!P I\!P I\!P} + 2\alpha'_{I\!P}\ln(W^2/M_X^2)$.

In this kinematical domain where $x_{I\!P} = M_X^2/W^2 = 1 - z \geq 0.12$, the complete mixture of $I\!P$, $I\!R$ and π contributing trajectories are important as explained by Field and Fox in [57]. But given the complexity of a triple Regge analysis and given the limited kinematical region to make a complete decomposition, the sum over all possible exchanges was replaced by single effective trajectories α_i and α_k. A triple Regge fit of the following form,

$$\frac{d\sigma}{dz} = W^2\frac{d\sigma}{dM_X^2} = \frac{A}{b}s_0^{1-\alpha_k(0)}\left(e^{bt_{min}} - e^{bt_{max}}\right)W^{4\alpha_i(0)-2}M_X^{2\alpha_k(0)-4\alpha_i(0)}, \tag{2.76}$$

was performed on the data, with t_{min} the minimum kinematical value of t and $t_{max} \sim p_T^2 \leq 0.04$ GeV^2. The t-dependent terms are assumed to be absorbed into a single exponential e^{bt},

where $b = b_0 - 2\alpha_i' \ln(1-z)$. The cross section shown in figure 2.18 shows an approximate independence of $d\sigma/dz$ of M_X^2 and W which leads to the expectation that $4\alpha_i(0) - 2 \sim 0$ and $2\alpha_k(0) - 4\alpha_i(0) \sim 0$, or $\alpha_i(0) \sim 0.5$ and $\alpha_k(0) \sim 1$. From the fit one indeed finds:

$$\begin{aligned} \alpha_i(0) &= 0.33 \pm 0.04\ (\text{stat}) \ \pm 0.04\ (\text{syst}), \\ \alpha_k(0) &= 0.99 \pm 0.01\ (\text{stat}) \ \pm 0.05\ (\text{syst}), \\ b_0 &= (3.6 \pm 0.7\ (\text{stat}) \ \pm 1.4\ (\text{syst}))\ \text{GeV}^{-2}. \end{aligned} \tag{2.77}$$

The result of the fit is shown by the full line in figure 2.18. The exchange between the photon and the proton can be understood as a mixture of trajectories dominated by π and $I\!R$ exchange, since the extracted value of $\alpha_i(0)$ was found between zero and one, the values of the intercept for respectively the pion and reggeon trajectory [37]. This result is also consistent with the previous H1 measurement at higher Q^2 [70]. In addition since $\alpha_k(0)$ was found to be unit, the total cross section for the scattering between the mixture of Regge trajectories α_i and the photon seemed to be dominated by pomeron exchange, as would be expected for total cross sections at these energies ($M_X^2 \in [1010, 16915]$). The value b_0 extracted from the fit implied that $b = (6.6 \pm 0.7\ (\text{stat}) \ \pm 1.5\ (\text{syst}))\ \text{GeV}^{-2}$ for a mean value of $z = 0.78$ which was found to be compatible with the direct measured value of ZEUS [71] for $p_T^2 < 0.5\ \text{GeV}^2$.

A comparison was made with $pp \to Xp$ data from Ganguli and Roy [66], assuming vertex factorization and shown by the dashed curve in figure 2.18.a-e. The prediction at $W = 187$ GeV and its decomposition obtained from a triple Regge analysis on $pp \to Xp$ data into the three dominant triple Regge terms are shown in figure 2.18.f. The predicted photoproduction cross sections lie 25 to 65% above the measured values, which can be considered as a reasonable agreement given the simplicity of the model, the uncertainties on the couplings and the basic difference between γp- and pp-data very often described by the gap survival probability. This agreement contrasts with the discrepancies of an order of magnitude or more observed when predictions were made for diffractive hard scattering cross sections at large z in $\overline{p}p$ collisions at the Tevatron [72] using parton densities extracted from diffractive DIS at HERA [48, 49].

However very recently the ZEUS collaboration has measured the differential cross section using leading proton data [73]. Instead of measuring $d\sigma(\gamma p \to Xp)/dz$ like in the case of the H1 collaboration [69], the ZEUS collaboration measured $1/\sigma_{tot} d\sigma(\gamma p \to Xp)/dz$ leading to the advantage that most acceptance correction factors and systematic uncertainties cancel in the ratio. Figure 2.19 shows the comparison between the H1 and ZEUS measurement,therefore the differential cross section from H1 is divided by the total cross section $\sigma_{tot} = 160\ \mu$b [42] at $W = 187$ GeV. Notice that the ZEUS measurement is performed at $\langle W \rangle = 200$ GeV, while the γp centre of mass energy from the H1 measurement is at $\langle W \rangle = 187$ GeV. The mean difference factor between both experiments is of the order of 1.9.

Non tagged proton data

Non tagged $\gamma p \to XY$ large rapidity gap data, with Y a proton or a low mass proton excitation are used in [68] to measure the differential cross section $d\sigma/dM_X^2$ at two γp

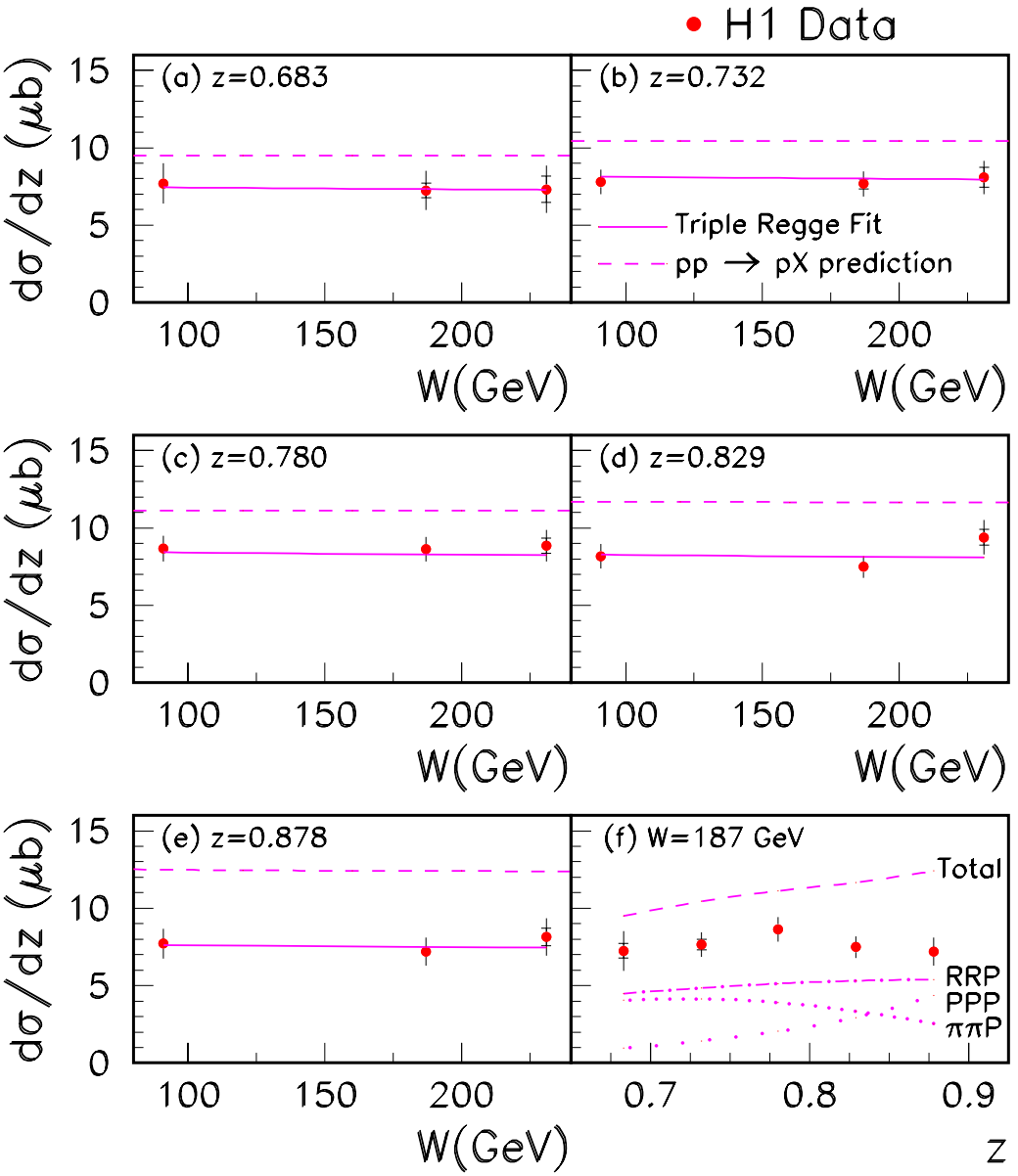

Figure 2.18: *The differential cross sections $d\sigma/dz$ as a function of W for each measured z value in the leading proton spectrometer. The data are compared with the results of a triple Regge fit and with the predictions from a triple Regge analysis on $pp \to Xp$ data. f) Shows the measured cross section as a function of z at W=187 GeV compared with the prediction derived from triple Regge analysis of $pp \to Xp$ data together with the decomposition into the three dominant terms.*

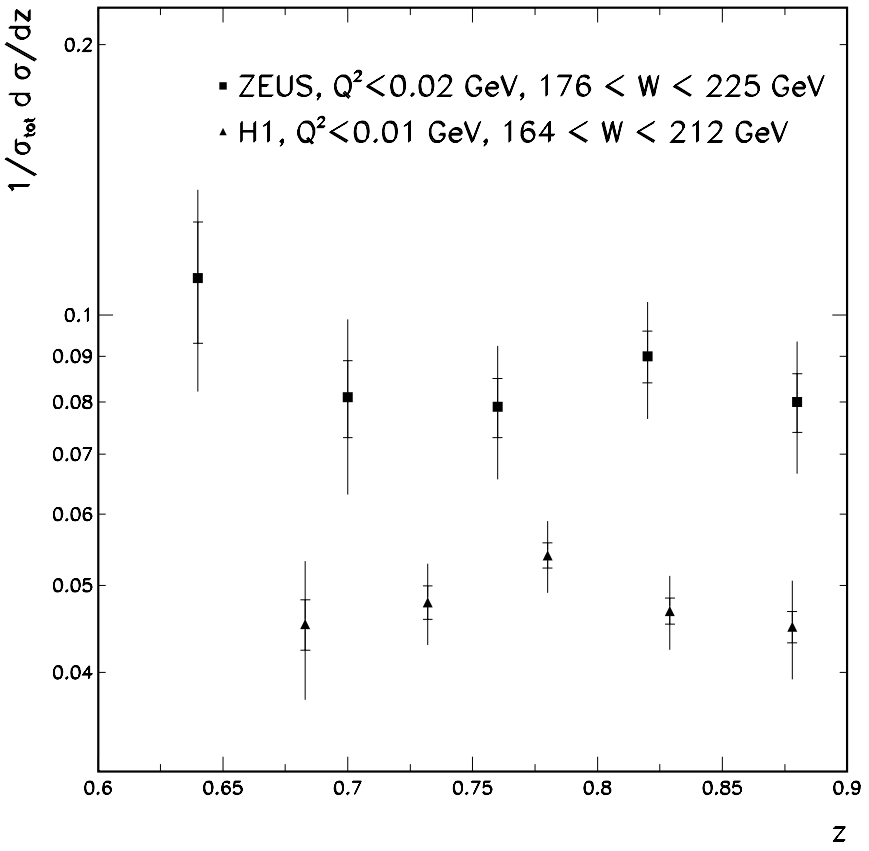

Figure 2.19: *The normalized cross section* $(1/\sigma_{tot})\ d\sigma/dz$ *for photoproduction data in the region* $p_T^2 < 0.04\ GeV^2$ *is compared between the H1 and ZEUS experiment. The inner error bars indicate the statistical uncertainties, and the outer error bars are the statistical and systematical uncertainties added in quadrature.*

centre of mass energies $\langle W \rangle$=231 and 187 GeV. Those data were subjected to a triple Regge fit, taking interference terms into account, of the form:

$$\frac{d^2\sigma}{dtdM_X^2} = \frac{s_0}{W^4} \sum_{i,j,k} G_{ijk}(t) \left(\frac{W^2}{M_X^2}\right)^{\alpha_i(t)+\alpha_j(t)} \left(\frac{M_X^2}{s_0}\right)^{\alpha_k(0)} \cos[\phi_i(t) - \phi_j(t)], \tag{2.78}$$

where $\phi_i(t)$ represents the phase of reggeon i which is determined by the signature factor. When no interference between the diffractive and non-diffractive exchanges is considered, which means $i = j$, then equation (2.78) is identical to previously mentioned triple Regge formula given in equation (2.71). The sum in the triple Regge formula is performed over only six terms given in table 6.1. Here no π-exchange was considered since they give contributions which are negligible at low M_X and become comparable to diffractive pomeron exchange

Parameter	Value		
$\alpha_{I\!R}$	0.55	$\pm$0.10	
α_{π}	0.	$\pm$0.	
$\alpha'_{I\!P}$	0.26	$\pm$0.02	GeV^{-2}
$\alpha'_{I\!R}$	0.90	$\pm$0.10	GeV^{-2}
α'_{π}	1.	$\pm$0.50	GeV^{-2}
$b_{pI\!P}$	2.3	$\pm$0.30	GeV^{-2}
$b_{pI\!R}$	1.0	$\pm$1.0	GeV^{-2}
$b_{p\pi}$	1.0	$\pm$1.0	GeV^{-2}
b_{ijk}	0.0	$\pm$1.0	GeV^{-2}

Table 2.3: The fixed parameters in the triple Regge fit and their assumed values.

only at $M_X^2 \approx 0.03W^2$ [57].

In order to investigate the importance of the six terms a large range in W^2 and M_X^2 is required. Therefore the fixed target data from [74] with $\langle W\rangle$=12.9 and 15.3 GeV and $4 \leq M_X^2 \leq 18$ GeV^2 are added to these rapidity gap data [68] with $\langle W\rangle$=231 and 187 GeV and $0.16 \leq M_X^2 \leq 1860$, on which simultaneous fits were performed. The parameters listed in table 2.3 were fixed to the measured values from [36, 75, 44, 76], $\alpha_{I\!P}(0)$ and the four couplings, $G_{I\!P I\!P I\!P}(0)$, $G_{I\!P I\!P I\!R}(0)$,$G_{I\!R I\!R I\!P}(0)$ and $G_{I\!R I\!R I\!R}(0)$ were free fit parameters.

Three scenarios were examined in this analysis. Based on the χ^2/ndf values from each fit, a preference for either a large interference or a large isovector contribution to the subleading terms (see section 6.2.1), or else a mixture of both could be concluded. A single value of the pomeron intercept was obtained by taking the average of the three fits, giving $\alpha_{I\!P}(0) = 1.068 \pm 0.016 \pm 0.022 \pm 0.041$. The result of the fit where interference was taken into account based on the assumption of maximal coherence (see section 2.5.3) is shown in figure 2.20. No contribution from isovector exchange is taken into account by the fit. The fit represents the scenario in which the f is the dominant subleading exchange and the f and the pomeron couple similarly to the proton. The ZEUS Collaboration has also measured the photon dissociation process at $\langle W\rangle$=200 GeV using rapidity gap data [77]. As they only used their own data in the fit, a less detailed analysis was performed. The photon dissociation mass spectrum was analysed in the range $3 \leq M_X \leq 24$ GeV, assuming the presence of only $I\!P I\!P I\!P$ and $I\!P I\!P I\!R$ terms in the triple Regge sum. It was shown that the $I\!P I\!P I\!P$ term could describe the large mass spectrum, $8 \leq M_X \leq 24$ GeV with a value of the pomeron intercept, $\alpha_{I\!P}(0) = 1.12 \pm 0.04 \pm 0.08$. They also verified that a two component contribution of $I\!P I\!P I\!P$ and $I\!P I\!P I\!R$ with $\alpha_{I\!P}(0) = 1.08$ and $\alpha_{I\!R}(0)$=0.45 gave a good description of the data over the whole M_X-range. The contribution of the $I\!P I\!P I\!R$ term to the cross section over the full M_X-range was estimated to be $f_{I\!P I\!P I\!R} = 23 \pm 5$(stat) %. It should be emphasized that in the ZEUS Collaboration, the diffractive sample is obtained by subtracting from the rapidity gap sample the non-diffractive component which is modeled by the Monte Carlos EPSOFT and PYTHIA and which is in contrast with the definition of diffraction in H1.

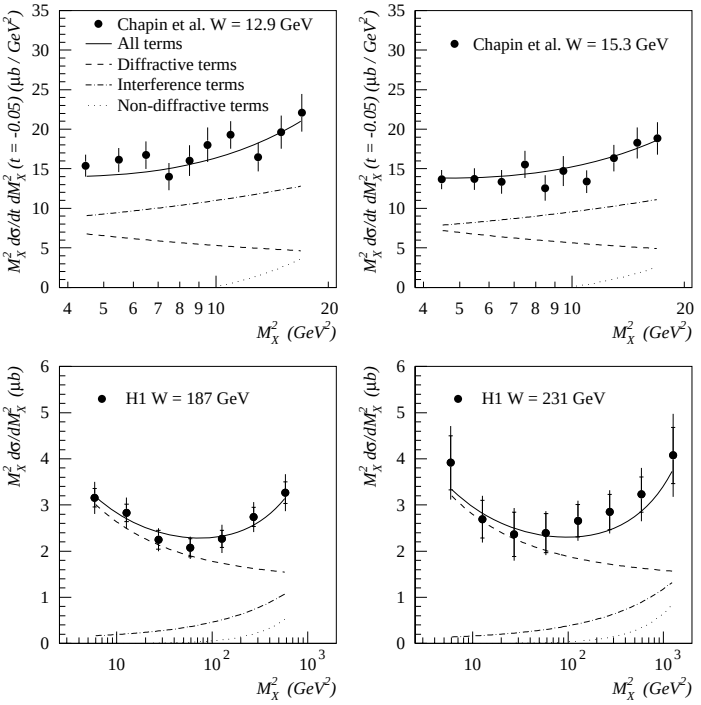

Figure 2.20: *A triple Regge fit taking maximal constructive interference between the diffractive and non-diffractive exchange into account on the diffractive differential cross sections from [68] and [74].*

Chapter 3

The H1 experiment at HERA

H1 is one of the two general purpose detectors installed at HERA (Hadron Electron Ring Anlage) and designed to study electron-proton or positron-proton interactions. The present chapter, after a brief introduction on HERA, describes the H1 detector components with emphasis on those which are of primary importance to this analysis. An exhaustive detector description can be found in [78].

3.1 The HERA collider

The HERA machine [79] is the world's first lepton-nucleon collider. It is located in Hamburg, Germany, and has been providing luminosity to the experiments H1 and Zeus since the summer of 1992. It is schematically shown in figure 3.1, along with the pre-HERA accelerator elements.

The HERA collider is composed of two rings one for the electron (positron) and one for the proton beam storage, having a circumference of 6.3 km. Electrons are accelerated to 27.5 GeV and protons to 820 GeV [1]. Conventional magnets are used to steer the electron beam, but fields well in excess of the magnetic saturation of iron are required to constrain the 820 GeV protons. Therefore a field of 4.6 Tesla is used with a system of superconducting coils. The beams are steered in a way that they cross at zero angle at two points on the ring where collisions may take place.

The beams are bunched in small buckets (called bunches) separated 28.8 m (or 96 ns). Some bunches are left empty so that a filled electron or proton bunch might arrive at the interaction point without a corresponding colliding partner. These so called *pilot bunches* are useful for studying background events due to the collision of an electron or proton with residual gas in the beam-pipe (*beam-gas interactions*) or with the beam-pipe-wall (*beam-wall interactions*).

Two detectors, H1 located at the north and Zeus located at the south side of HERA, have been built around the interaction points. Both multi-purpose detectors provide nearly

[1] Since 1998 the HERA accelerator operates with 920 GeV protons.

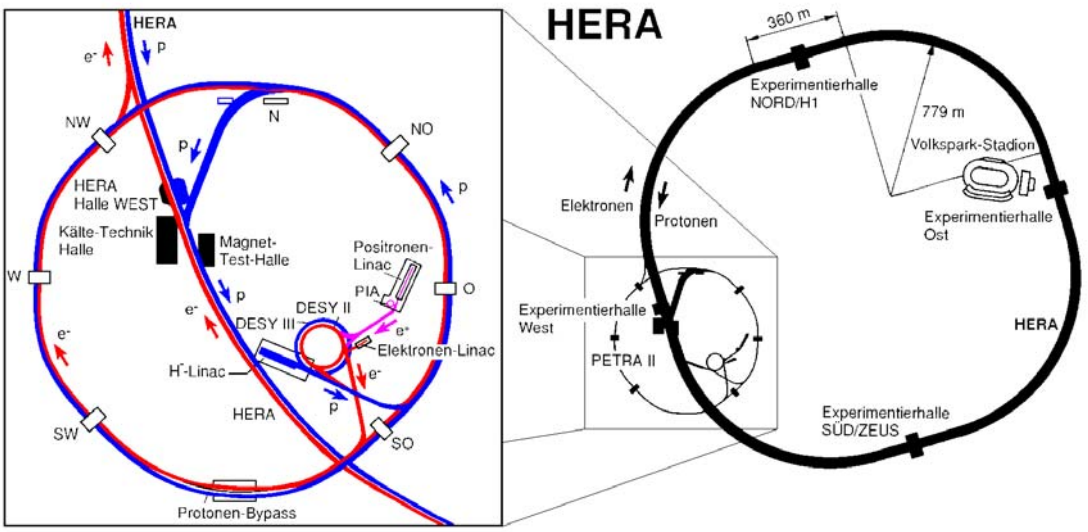

Figure 3.1: *The layout of HERA is shown on the right, along with the location of the different detector halls. The pre-accelerators are shown in the blowup on the left.*

full angular coverage and are asymmetric in the beam direction, optimizing the acceptance for high multiplicity final states in the proton direction.

The electron (positron) beam can be polarized up to 70 %, by making use of the fact that over a period of time, synchrotron radiation leads to a natural transverse polarized beam. A third experiment, HERMES [80] located on the east side of HERA, makes use of this polarized beam by colliding it with a polarized proton gas jet to study the spin structure of the proton. A fourth experiment, HERA-B [81] located on the west side of HERA, was approved in February 1995, primarily to search for CP violation in decays of B mesons.

The most important HERA parameters are given in table 3.1, showing those used in 1997, the year in which the data for the present analysis were collected.

3.2 General description of the H1 detector

The H1 detector depicted in figure 3.2 is designed to study many aspects of ep scattering and therefore consists of a number of subsystems providing complementary information, from which the properties of the collision processes can be reconstructed. In order to exploit fully the physics potential, the detector has to fulfil a number of major roles, which are:

- **Electron detection:** identification and energy measurement of scattered electrons is vital for the study of neutral current DIS events as well as for photoproduction events, where the scattered electrons are at very low Q^2 values.

Parameter	*Unity*	*1997* e^+/p
Circumference	m	6336
Interaction points		4
Max. number of bunch slots		220/220
Number of colliding bunches		174
Number of e-pilot bunches		15
Number of p-pilot bunches		10
Number of empty bunches		21
Nominal energies	GeV	27.55/820
Mean Currents	mA	40/100
Package separation	ns	96
σ_x *at IP*	μm	179
σ_y *at IP*	μm	48
σ_z^{proton} *at IP*	mm	200
$\mathcal{L}_{inst}$	$\mathrm{cm}^{-2}\mathrm{s}^{-1}$	1.4 x 10^{31}

Table 3.1: The main HERA parameters.

- **Hadron detection:** calorimetry with good resolution and fine granularity is needed for characterizing the hadronic final state in many processes. The calorimeter must be hermetic in order to measure the transverse energy balance while for charged current DIS events, the undetected final state neutrino exhibits an imbalance.
- **Charged particle tracking:** charged particle momentum measurement and identification is required for the investigation of many processes at HERA. This is provided by tracking detectors covering a large solid angle. A magnetic field curves the tracks and allows the momentum to be determined, while energy loss measurements enable particle identification.
- **Muon identification:** heavy flavor, rare Standard Model and exotic physics processes are detected through the production of muons in the final state.
- **Luminosity measurement:** accurate determination of the luminosity delivered to the experiment is vital for calculation of cross sections.
- **Triggering and readout:** on the basis of the fast information coming from the different detector subsystems, a selection of ep interactions of physics interest has to be done by the trigger system.

In these aspects the H1 detector does not differ strongly from the detectors at e^+e^--colliders, or pp-colliders built in the past. The principal H1 detector parameters are given in table 3.2. Specific at HERA are however the imbalance in the energy of the two colliding beams, which requires an asymmetric detector. Different also is the micro-structure of the

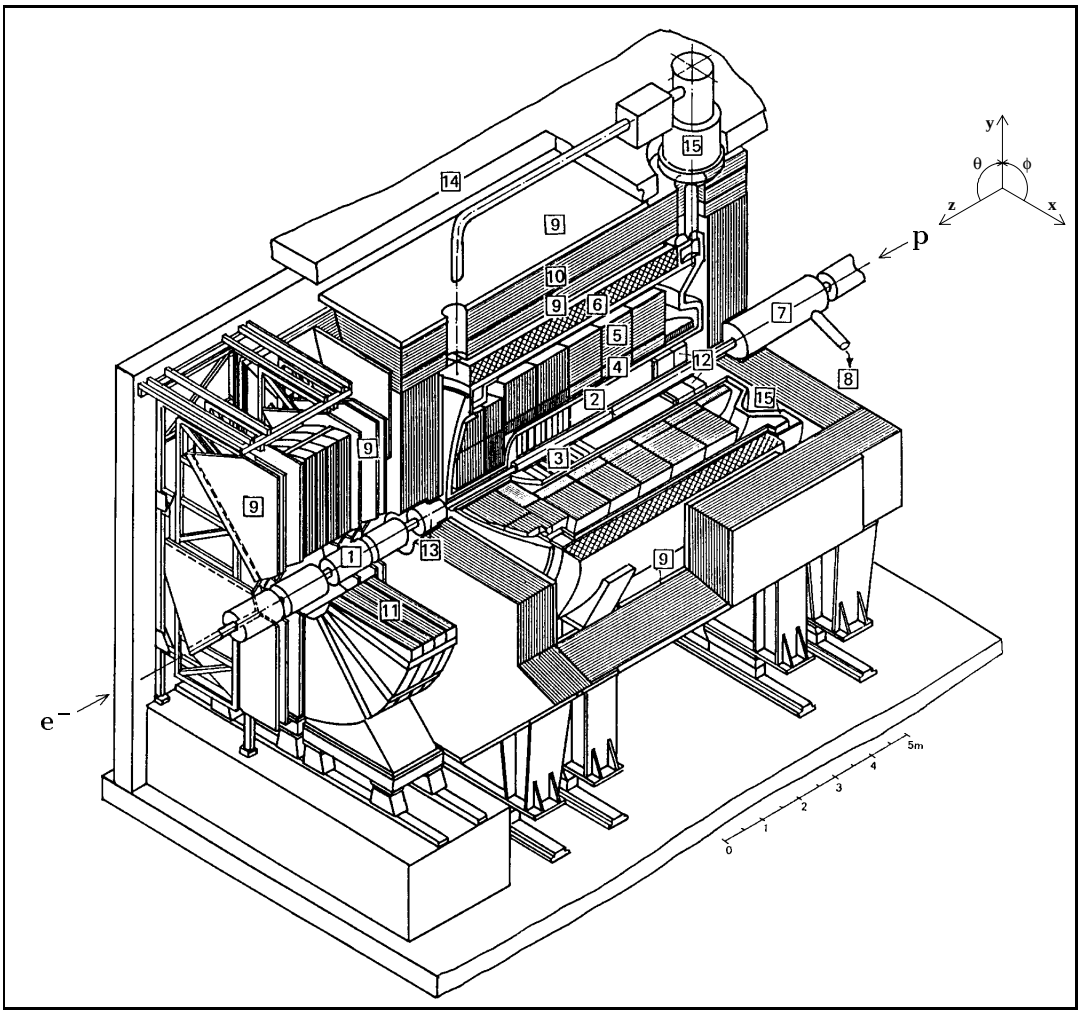

1	Beam pipe and beam magnets	9	Muon chambers
2	Central tracking device	10	Instrumented iron yoke
3	Forward tracking device	11	Forward muon toroid
4	Electromagnetic LAr calorimeter	12	Backw. calorimeter (SPACAL)
5	Hadronic LAr calorimeter	13	PLUG calorimeter
6	Superconducting coil (1.15 T)	14	Concrete shielding
7	Compensating magnet	15	Liquid argon cryostat
8	Helium supply for 7		

Figure 3.2: *Schematic layout of the H1 detector.*

Component	*Parameter*	*Value*
LAr calorimeter	angular coverage	$4^o \leq \theta \leq 153^o$
	granularity (EM/Had)	10 - 100 cm^2 / 50 - 2000 cm^2
	depth (EM/Had)	20-30 X_0 / 4.7 - 7 λ_{int}
	number of channels (EM/Had)	30784 / 13568
	σ_E/E (EM shower)	$0.12/\sqrt{E(GeV)} \oplus 0.01$
	EM E scale uncertainty	1 - 3 %
	σ_E/E (Had shower)	$0.50/\sqrt{E(GeV)} \oplus 0.02$
	Had E scale uncertainty	4 %
	angular resolution	2 mrad for $\theta < 30^o$
	angular resolution	< 5 mrad for $\theta > 30^o$
SPACAL calorimeter	angular coverage	$153^o \leq \theta \leq 177.8^o$
	granularity (EM/Had)	4.05 x 4.05 cm^2 / 12 x 12 cm^2
	σ_E/E (EM shower)	$0.075/\sqrt{E(GeV)} \oplus 0.025$
	EM E scale uncertainty	1 - 3 %
	Had E scale uncertainty	7 %
	spatial resolution	4 mm
	time resolution	< 1 ns
Central Tracking	B-field (Tesla)	1.15
	angular coverage	$15^o < \theta < 165^o$
	σ/p_T	0.01 x p_T(GeV)
Luminosity	normalization uncertainty	1.5 %

Table 3.2: The principal H1 detector parameters (status 1997).

beams, which leads to the high bunch crossing rate at HERA (10.4 MHz), and also to high backgrounds from beam-gas and beam-wall interactions, therefore the detector must be able to identify physics processes from background, digitize and read out a large number of detector channels ($>$ 250,000) while minimizing dead time. A fast pipelined, multi-level trigger system, in combination with high-speed digitization and readout is therefore employed.

The main elements of the detector are shown in figure 3.2 as well as the reference frame adopted in the experiment. The positive z-axis points in the proton beam direction. The x-axis points to the centre of the HERA ring and the y-axis completes the right-handed system. In the following we often refer to the electron direction as the backward direction (negative z-values relative to the centre of the interaction region and $\theta = \pi$), and the proton direction as the forward direction (positive z and $\theta = 0$). Since the centre of mass for ep collisions at HERA is boosted along the proton direction with a factor γ_{CMS}=2.82, the H1 detector is considerably more massive and highly segmented in this direction.

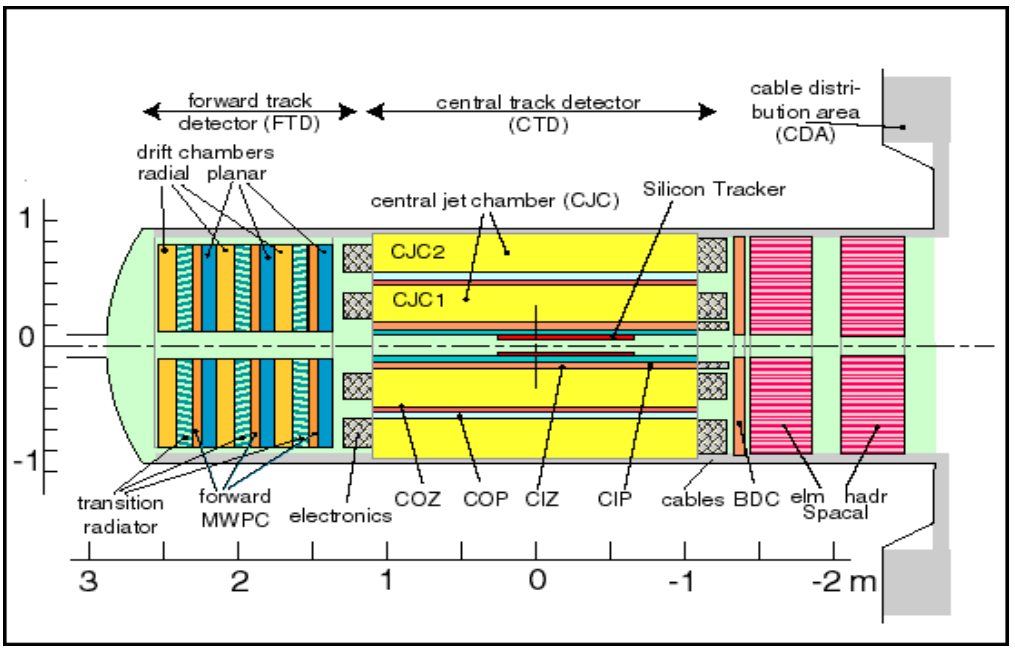

Figure 3.3: *A cross-sectional view of the H1 tracking system, showing the central and forward trackers, and the BDC.*

3.3 Tracking

The tracking system of H1 shown in figure 3.3 is split into two major components; the central tracker, covering the region in polar angle $15° < \theta < 165°$, and the forward tracker, covering the region $7° < \theta < 25°$. In addition, the backward region is covered by the backward drift chamber (BDC) which is mounted on the front of the SPACAL calorimeter and covers the region $151° < \theta < 177.5\,°$. The central and backward silicon trackers (CST and BST) provide precision measurements of tracks close to the interaction vertex. Only the central and forward tracking devices used in this analysis will be described in more detail below, since the CST and BST where still not fully operational in 1997.

3.3.1 The Forward Tracker (FT)

The forward tracker (FT) shown in figure 3.3, is used in this analysis to reconstruct tracks in combination with central tracks or to help in the construction of the z-vertex histogram (see section 3.9.1). The FT is composed of three very similar super-modules. Each super-module consists, in increasing z, of twelve layers of planar drift chambers, a section of multi-wire proportional chambers (MWPCs), transition radiators and twelve layers of radial drift chambers. The MWPCs in the first super-module are used with the CIP and COP in the z-vertex trigger.

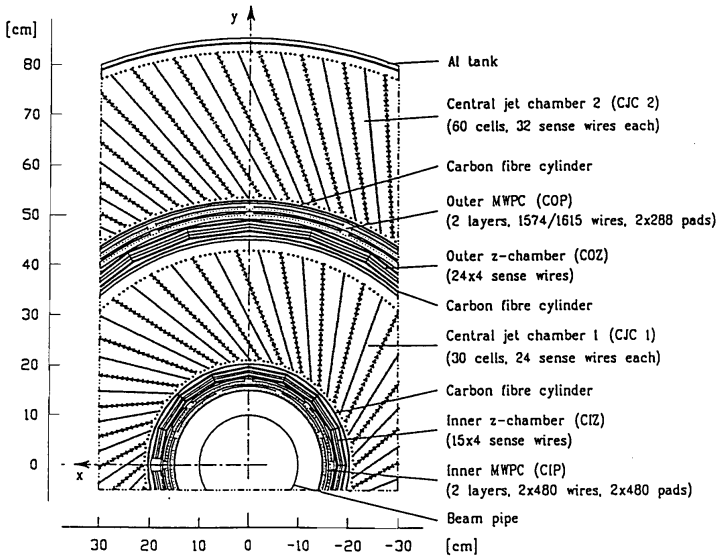

Figure 3.4: *The Central Tracker. A view in the r-ϕ plane*

3.3.2 The Central Tracker

Two large concentric drift chambers, CJC1 and CJC2, with a length of 2.2 m are the main components of the central tracking system. CJC1 (CJC2) consists of 30 (60) cells with 24 (32) sense wires parallel to the z axis shown in figure 3.4. The inner radius is 20.3 (53.0) cm and the outer radius 45.1 (84.4) cm. The drift cells are inclined by about 30° with respect to the radial direction. The space point resolution in (r,ϕ) is respectively 170 μm and 2.2 cm in z using a charge division method. The resolution in z is much improved by the usage of z-chambers (CIZ and COZ) with wires perpendicular to the beam-axis. CIZ is located inside and COZ outside CJC1 at a radius of 18 cm and 47 cm, respectively. CIZ and COZ are divided into 15 and 24 drift cells with 4 sense wires per cell. The achieved resolution in z is 260 μm.

Charged particles are bent by the homogeneous magnetic field of 1.15 T provided by the superconducting coil around the LAr calorimeter. The combination of CJC1 and CJC2 with the z-chamber measurements leads to momentum resolution for the track measurement of $\sigma(p_T)/p_T < 0.01\ p_T/\text{GeV}$. In addition to the drift chambers two multi-wire proportional chambers (CIP and COP) deliver fast signals used for trigger purposes (see section 3.9).

3.4 Calorimetry

Figure 3.5 shows an overview of the various components of the H1 calorimetry. Only the LAr and SPACAL calorimeters, used in this analysis for the measurement of the produced hadronic final state, will be described.

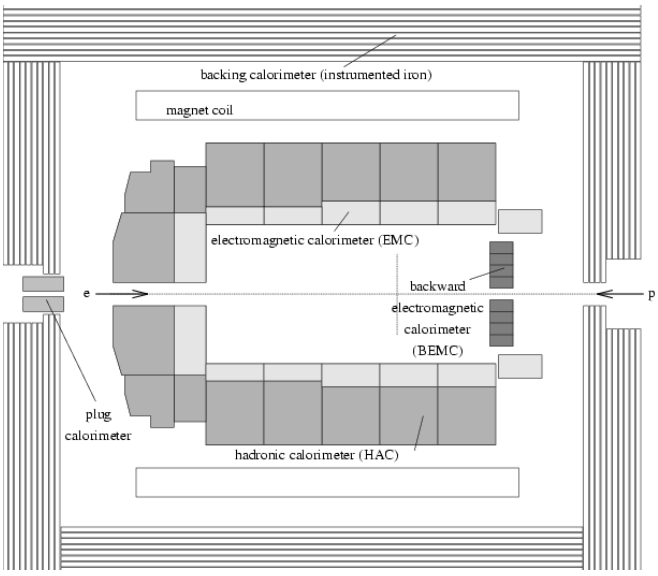

Figure 3.5: *$r-z$ projection of the H1 calorimeters.*

3.4.1 The Liquid Argon calorimeter

The LAr calorimeter shown in figure 3.6 provides energy measurement in the range $4^\circ < \theta < 154^\circ$ with full azimuthal coverage. The LAr, housed in a large cryostat inside the magnet solenoid, is segmented into 8 wheels each of which is further segmented into eight identical ϕ-octants. The six central wheels are divided into an electromagnetic and a hadronic section, whereas the most forward wheel consists of two hadronic sections. The most backward wheel (BBE) consists only of an electromagnetic section. The electromagnetic part of the LAr calorimeter is made of 2.4 mm thick lead absorber plates which are supplemented with high voltage and readout plates, alternated with similar size gaps flooded with liquid argon which serves as the active material. The total thickness varies between 20 and 30 radiation lengths depending on the polar angle. The hadronic section consists of 19 mm stainless steel absorber plates with a double gap of 2.4 mm filled with liquid argon. In total this corresponds to 5 to 8 hadronic interaction lengths. The LAr calorimeter energy resolutions for electromagnetic and hadronic showers have been measured in test beams [82] and are $\frac{\sigma(E)}{E} \sim \frac{0.12}{\sqrt{E}} \bigoplus 0.01$ and $\frac{\sigma(E)}{E} \sim \frac{0.50}{\sqrt{E}} \bigoplus 0.02$ respectively (the energy is expressed in GeV).

The LAr calorimeter is non compensating, i.e. the response to hadrons is about 30% smaller with respect to electrons with the same energy. This is corrected off-line using a weighting technique. The main advantages of the liquid argon technique are good stability, homogeneity of the response, ease of calibration and fine granularity. The total number of read-out channels is about 45000.

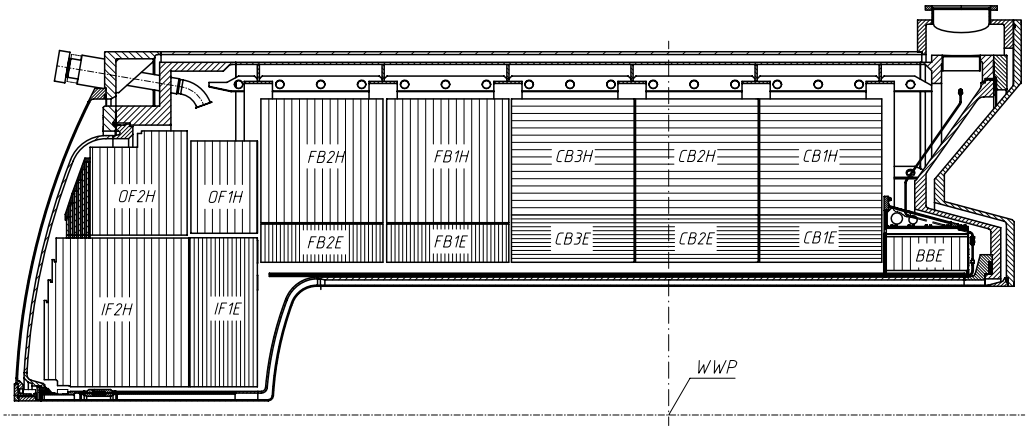

Figure 3.6: *Longitudinal view of LAr calorimeter.*

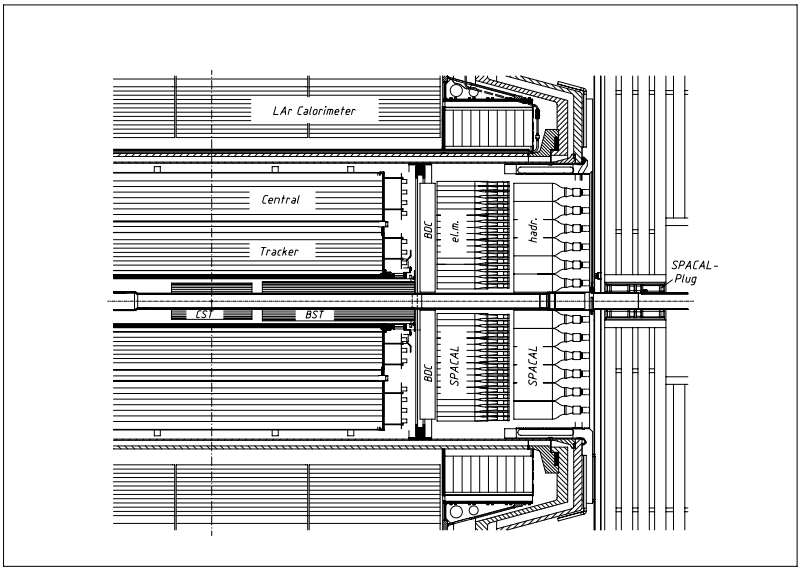

Figure 3.7: *Side view of part of the H1 detector showing the location of the SPACAL sections.*

3.4.2 The SPACAL calorimeter

The Spaghetti calorimeter, SPACAL, [83] shown in figure 3.7 provides energy measurement in the backward region in the range $154° < \theta < 178°$ with full azimuthal coverage. It is a sampling calorimeter with lead as absorber material and scintillating fibers as active material. The SPACAL is divided into an electromagnetic and a hadronic section with a lead to fiber ratio of 2.3:1 and 3.4:1, respectively. The electromagnetic section consists of 1192 cells of the size $40.5 \times 40.5 \times 225$ mm. Each cell consists of grooved lead plates interspersed with 2340 scintillating fibers 0.5 mm in diameter. Incident electrons and photons develop into an electromagnetic shower in the lead which subsequently causes the fibers to scintillate. The light is collected and read out by photomultiplier tubes. The cell size is adopted to the Molière radius of 25.5 mm. The length of the electromagnetic section corresponds to 28 radiation lengths which means that energy leakage of the detected electrons can be neglected. The energy resolution is parametrized [84] in test beam measurements to be $\frac{\sigma(E)}{E} \bigoplus b \sim \frac{0.07}{\sqrt{E}} \bigoplus 0.01$. The spatial resolution of the calorimeter in the transverse plane was measured to be 3.4 mm.

The hadronic (HAD) section is based on a design similar to the electromagnetic (EM) section with lead scintillating fibers but with a larger diameter of 1 mm. There are 136 cells of typical dimension 119.3 x 119.3 mm^2 which reflects the greater lateral dimension of hadronic showers. The hadronic resolution of the combined HAD and EM calorimeter is $\frac{\sigma(E)}{E} \sim \frac{0.3}{\sqrt{E}}$.

3.5 The Time of Flight devices

There are a number of relatively simple systems included in H1 which reject backgrounds on the basis of Time of Flight (ToF). The path length, and therefore the flight time, of interacting particles arriving at various parts of the detector differs from that of particles arising from beam-induced background, providing a useful method of discriminating between the two. The signals, information with a time resolution of $\approx$ 2 ns, are strobed against predefined "windows", corresponding to signal and background time periods. The ToF systems, constructed from plastic scintillators, are located near the beam-pipe in the backward endcap of the return yoke (BToF) and near the FMD (see section 3.6) (FToF). In addition, the "Veto Wall", a double set of scintillators positioned backward of the return yoke, detects particles from the proton beam-halo, which are mostly muons caused by inelastic collisions of the protons with the residual gas. The efficiency of the device for minimally ionizing particles has been measured to be 98$\pm$1% from studies of independently triggered beam-halo muons arriving nearly parallel to the proton beam. The Time of Flight information from the SPACAL calorimeter is also used to reject backgrounds and is described in section 3.9.

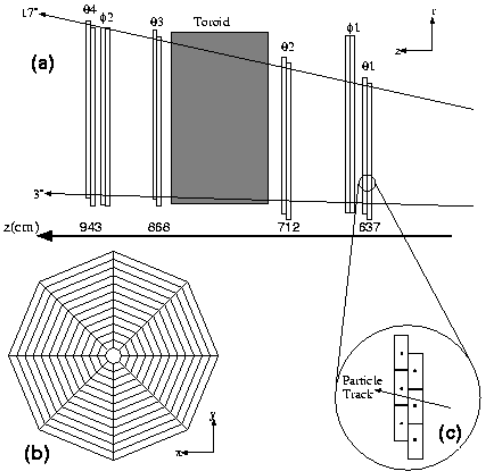

Figure 3.8: Schematic overview of the forward muon detector: a) rz projection; b) xy projection of single θ layer; c) rz projection of drift cell

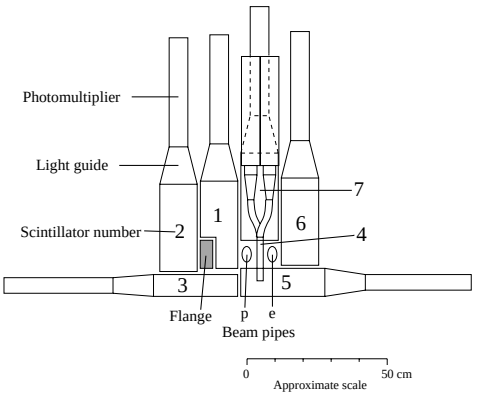

Figure 3.9: Schematic view of proton remnant tagger as seen from the interaction point

3.6 The Forward and Very Forward Detectors

The detectors grouped under this heading are used to distinguish proton elastic processes from proton dissociative processes. In proton elastic processes, the protons are scattered under very small angles and hence remain in the proton beam-pipe and leave the main detector undetected. Only a small fraction of them is tagged by the forward proton spectrometer (see section 3.6.3). Proton dissociative fragments however can sometimes be seen in the main forward muon detector (FMD). When the fragments are not detected in the FMD, they still can be detected by the forward proton tagger (PRT).

3.6.1 Forward Muon Detector (FMD)

The FMD situated outside the IRON on the outgoing proton side of the detector (see figure 3.8) was designed to measure the energy of high energetic muons originating from heavy quark decays produced in the forward direction. The detector has an angular coverage of $3^\circ < \theta < 17^\circ$ and consists of six double layers of drift chambers, four with wires strung tangentially around the beam-pipe to measure θ and two with wires strung radially to give a ϕ measurement. Three layers are situated on either side of a toroidal magnet (i.e. the pre- and post-toroid layers), designed to bend the muons to allow momentum measurement in the range $5 < \mathrm{p} < 100$ GeV. As shown in figure 3.8c, each layer consists of two planes of drift chambers, staggered from one another by half a cell. A paired hit in one of the layers is seen if two adjacent (in z) sense wires measure a signal.

Particles which are scattered under small angles into the forward region can hit collimators which are situated in the beam-pipe to protect the main detector from synchrotron

radiation. These secondary interactions produce a bunch of particles which then leaves signals in the FMD. The probability for elastically scattered protons to hit the collimators is very low. The geometrical acceptance of the FMD corresponds to the region $1 < \eta < 2.5$. Due to the position of the collimators this acceptance is extended to the region $3.2 < \eta < 5.5$. Therefore signals in the FMD are a good signature for events where the proton does not scatter elastically.

Only three pre-toroid layers from the FMD device are used to select diffractive events, since the post-toroid layers are suffering from high background rates due to synchrotron radiation originating from the bending in the electron beam before the interaction point.

3.6.2 Proton Remnant Tagger

The proton remnant tagger (PRT) (see figure 3.9) is situated 24 m from the nominal interaction point in the forward direction. It consists of seven individual scintillators arranged around and between the electron and proton beam-pipes, as shown in figure 3.9. Each scintillator comprises 2 parallel sheets of plastic scintillators. The PRT is sensitive to particles which originate from secondary interactions of hadrons emerging from proton dissociation events which extends the sensitivity for particles detected up to η=7.5.

3.6.3 Forward Proton Spectrometer

The Forward Proton Spectrometer (FPS) consists of four Roman pot stations. A schematic view of one station is shown in figure 3.10. In every station there are two fibre detectors each of which measure a uv-coordinate of a passing charged particle with a resolution of $\sigma_x = \sigma_y = 120$ μm. The stations located at 81 and 90 m approach the beam vertically, those at 64 and 80 m approach the beam horizontally. The vertical and horizontal pots cover a different kinematic range, but the acceptance for both the horizontal and vertical pots is small ($< 10\%$). Measurement of the position and angle of the through going particle and knowledge of the beam-optics allow the momentum vector of the scattered proton to be reconstructed.

3.7 The luminosity system

Measuring a cross section necessitates a precise determination of the integrated luminosity. Normally the measurement of a process with a well known cross section is used to satisfy this demand. At HERA the Bethe-Heitler process $ep \to e\gamma p$ (where the electron and the photon are produced in the same direction as the incoming electron) is used for the luminosity measurement for which a precise cross section calculation exists in the highly relativistic limit and small angle approximation [86].

Figure 3.11 shows the luminosity system. It consists of the electron tagger (ET33) located at z=-33.4 m and the photon detector (PD) at z= -102.9 m which are two electromagnetic calorimeters. Both hodoscopes are crystal Cerenkov counters with high radiation

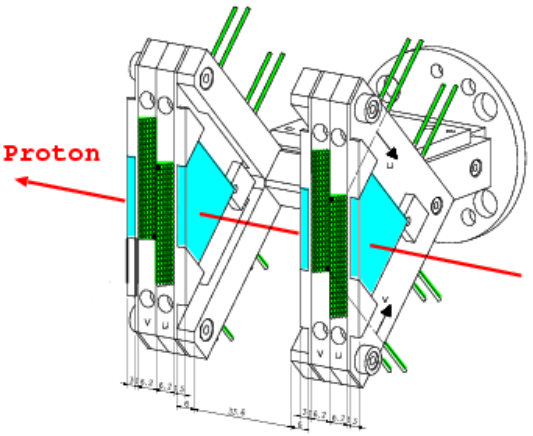

Figure 3.10: *A schematic view of a Roman pot station with 2 horizontal scintillating fiber detectors.*

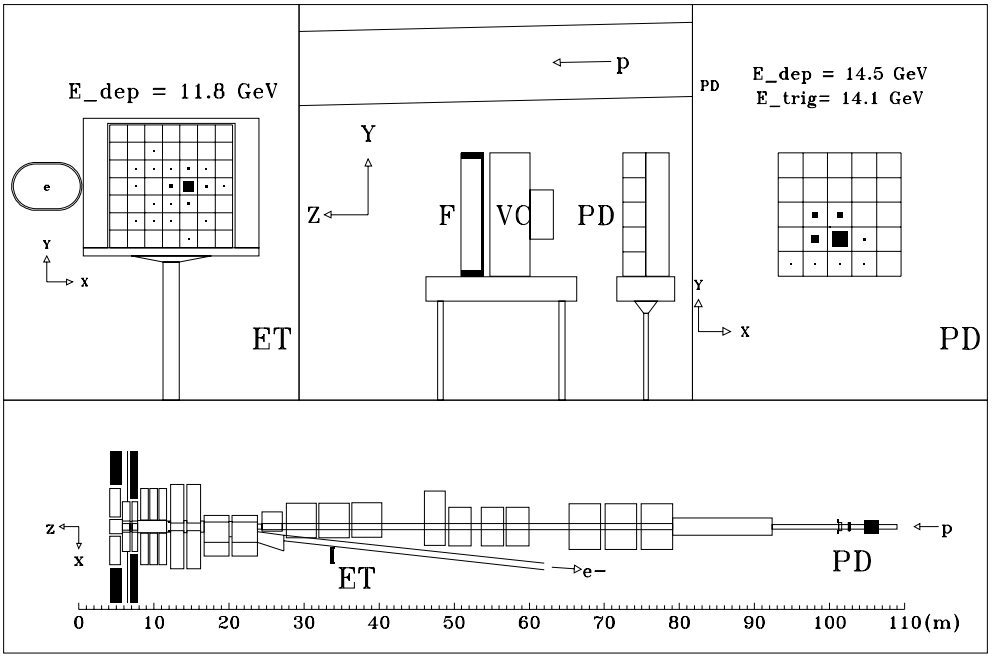

Figure 3.11: *The layout of the lumi system. On the left top figure the ET33 calorimeter , in the middle a side view of the photon arm, consisting of a lead filter (F), a water Cerenkov counter (VC) and the main photon detector (PD), on the right a x-y projection of the photon detector (PD) is displayed. In the lower part a global overview of the system is shown with their positions relative to the interaction point.*

	ET33	*ET44*	*PD*
Material	TlCl + TlBr		
Size in mm	154 x 154	44 x 66	100 x 100
Granularity	7 x 7	2 x 3	5 x 5
Length of a crystal	20 cm		
Interaction length X_0	0.93 cm		
Moliere-Radius R_M	2.10 cm		
σ_E/E	1% + 10% / $\sqrt{E}$, E in GeV		
Acceptance in y (Q^2 < *0.01 GeV*^{2})	0.2 - 0.8	0.04 - 0.2	

Table 3.3: *Some parameters of the calorimeters related with the luminosity system.*

resistance and good energy, spatial and time resolution. The scattered electrons from the Bethe-Heitler process are bent by a set of quadrupole magnets before they leave the beam-pipe at z= -27.3 m through an exit window and hit the electron tagger. The scattered photons are dominantly scattered under small angles. The photons, scattered at very small angles, leave the proton beam at z = -92.3 m, where the beam-pipe bends upwards, and are absorbed in the photon detector (PD). The PD is shielded from synchrotron radiation by a lead filter (F), which is followed by a water Cerenkov Veto counter (VC) which rejects events with photons originating from interactions in the filter. The ET33 and the PD are mounted on movable platforms which are retracted during injection to protect the system from radiation damage.

A second electron tagger at $z = -44$ m (ET44) is built in a similar way, however spatially smaller than the electron tagger at 33 m. Technical details are given in table 3.3.

Both electron taggers are also used to tag photoproduction events. When the scattered electron is measured near the boundary of the electron tagger (ET33), there is a high probability that only part of its total energy is contained in the detector, this leads to a wrong electron energy. Therefore a cut on the local x coordinate $|x_{tag}| < 6.5$ cm in the electron tagger (ET33), of the centre of gravity of the electron cluster, is applied. This means that events in which the energy deposit is within 1.5 cm of the edge of the detector are rejected. Due to the small geometrical size of ET44, the total energy of a scattered electron is never fully contained in this detector. However due to the small acceptance of the ET44 (see figure 4.5) a fixed energy value of 24.5 GeV can be assigned to the scattered electron which was triggered by the tagger. A cut on the position of the center of gravity is therefore not necessary for this electron tagger.

3.7.1 Luminosity measurement

The luminosity collected by the experiment can be measured by two different methods [87] based on the radiative process, $ep \to ep\gamma$:

- **Coincidence method:**
  The simultaneous measurement of an electron in the ET33 and a photon in the PD is required.

- **Photon method:**
  The luminosity is measured from the rates of detected photons alone.

The advantage and drawbacks of both methods can be found in [88]. For the online luminosity measurement by the H1 monitor system the coincidence method is applied. For the off-line determination of the final value of the integrated luminosity $\mathcal{L}$, the single photon method is used. The luminosity integrated over the time interval Δt is determined using the formula:

$$\mathcal{L} = \frac{\mathcal{N}_{BH}^{ep}(\Delta t, E_\gamma > E_{min})}{\sigma_{BH}(E_\gamma > E_{min})} \tag{3.1}$$

where $\mathcal{N}_{BH}^{ep}(\Delta t, E_\gamma > E_{min})$ denotes the number of selected ep events with an energy E_γ larger than a minimal energy E_{min} measured by the photon detector. $\sigma_{BH}(E_\gamma > E_{min})$ denotes the cross section for the production of photons in that kinematic range. $\mathcal{N}_{BH}^{ep}(\Delta t, E_\gamma > E_{min})$ has to be corrected for trigger efficiencies, acceptance of the photon detector which depends on the run dependent tilt of the beam and the pile up effect where more than one Beite-Heitler process in a bunch crossing happens. The final systematic uncertainty is 1.5%.

3.8 Triggering and data acquisition

The purpose of the H1 trigger is to select interesting ep events and to reject high rate background events. At the designed luminosity of 1.5x10^{31} cm^{-2}s^{-1}, the rate of DIS events is ∼5 Hz and the rate of the dominant physics process (photoproduction) is ∼100 Hz. The interesting physics channels are inundated by a background with a thousand times higher rate, consisting of three basic types:

- synchrotron radiation from the electron beam,
- proton-gas interactions in the beam-pipe vacuum of about 10^{-9} mbar and
- electron or proton interactions with the beam-pipe walls and with the surrounding equipments.

The essence of the difficult trigger challenge is the disparity between the bunch crossing interval of 96 ns and the different response and read-out times of the detector components, meaning that the experiment could be 'dead' to events in the detector for a large fraction of time if every event were processed in full. The background conditions as well as the short bunch time interval of 96 ns and the request for low dead time of the read-out system results in a multilevel centrally clocked trigger system.

3.8.1 Level 1 trigger system (L1)

The level 1 trigger consists of a hardwired trigger logic with 128 subtriggers. These are built by logical combinations from 128 trigger elements provided by the different detector subsystems. The L1 trigger is fully pipelined and thus dead time free. Its decision time is 2.3 μs. After a positive trigger decision at level 1 the pipelines are stopped and the trigger data are submitted to the level 2 trigger systems.

When a "L1-keep" signal is given, the dead time for the experiment begins. This can be interrupted after 20 μs by a rejection from level 2 or after 210 μs by level 3, and the pipelines are re-enabled.

3.8.2 Level 2 trigger system (L2)

The level 2 trigger is divided into two sections, the topological trigger (L2TT) and the neural network trigger (L2NN). Both systems use the combination of signals from the different detector subsystems. The topological trigger takes a decision on the basis of pattern recognition which is hardwired in the electronics. The data for the neural network trigger are preprocessed and subsequently used as input for fast processors on which beforehand trained neural networks are implemented. The decision time for this trigger level is 20 μs in which the detector is not able to take events. Those level 2 triggers were not used in the collection of the minimum bias data which were used to perform this analysis.

3.8.3 Level 3 trigger system (L3)

This trigger system being an option to re-enable the pipeline after 210 μs was not operational in 1997.

3.8.4 Level 4 trigger system (L4)

The level 4 trigger consists of a farm of processors on which event reconstruction is performed and subsequently decision algorithms decide whether an event is taken or not. Up to 40 events are processed asynchronously with a processing time of about 100 ms for each event. After the acceptance of an event the data are submitted to the DESY computing centre where they are written to tape at a rate of about 10 Hz and an average size of 130 KBytes per event. Approximately 1% of the events rejected at the level 4 stage are allowed through the filter, to monitor the effect of cuts. As reconstructed data of the whole detector merge in L4 for the first time, it is well suited for monitoring and calibrations: numerous monitor histograms are filled there, which can be inspected online.

3.8.5 Level 5 trigger system (L5)

Although all the data passing L4 is written to tape and permanently stored, further selection takes place to prepare the data sets for physics analysis and to remove the remaining

background events. A full reconstruction and classification is done off-line and is referred to as level 5 (L5). This is performed by a dedicated workstation, typically within 24 hours of the time when the data was recorded at L4. On L5 a detailed linking of charged track segments and energy cluster is performed to complete the overall description of the event. All the events are classified in at least one of the different physics classes (event classification), before being written to Production Output Tapes (POTs) and stored. The output after reprocessing of the data is written to Data Summary Tapes (DSTs) which contain compressed data that reflects the characteristics of the event in a simple format useful for analysis, such as tracks and calorimeter clusters, rather than the raw sub-detector information. The typical size of an event on the DST is reduced to 10 KBytes, thus allowing the events to be stored on disk, enabling easy and rapid access for analysis.

3.9 Trigger sub-system

The trigger sub-systems, which produce trigger elements used in this analysis are discussed in this section. The systems are the z-vertex trigger and the SPACAL trigger.

3.9.1 The z-vertex trigger

The z-vertex trigger [89] reconstructs the primary interaction vertex along the z-coordinate which is very useful in rejection of non-ep induced backgrounds. The z-vertex trigger is able to provide this information at the level 1 trigger stage. It is used in two of the four subtriggers in this analysis, and operates on the signal from the double cylindrical MWPC layers of CIP and COP along with the double layer of the planar MWPC of the first super-module of the forward tracker.

The basic principles of the z-vertex trigger is illustrated in figure 3.12. For every bunch crossing, "rays" reconstructed from the pads hit and their intercept with the z-axis are input to a 16 bin (5.4 cm wide) histogram. Tracks originating from one vertex will produce a peak in the histogram; background tracks resulting from outside the H1 detector will produce a flat z-distribution. Similarly "fake tracks" resulting from accidental pad combination also produce a flat distribution.

The 16-fold ϕ-segmentations of the chambers corresponds to 16 independently built histograms, one for each segment. The choice of 16 ϕ-segments is a compromise between suppressing random coincidences and accepting low momentum particle traces. The 16 histograms from the different ϕ-segments are summed and the combined histogram is used to define trigger elements to be sent to the first level trigger.

The presence of a good vertex is then signalled by a peak in the z-vertex histogram, with a predefined signal/background ratio.

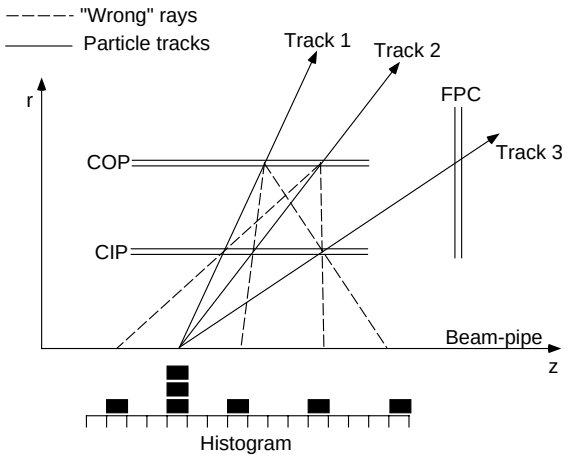

Figure 3.12: *Vertex reconstruction, which displays a peak at the true vertex location, showing a single segment in ϕ for a hypothetical event with 3 tracks. Rays made from wrong combinations form a random pedestal.*

3.9.2 The SPACAL trigger

The SPACAL trigger provides two functions in the H1 experiment; a trigger for events containing electron candidates and a veto for events originating from beam-induced background. The system therefore consists of the Inclusive Electron Trigger (IET) for the electromagnetic (EM) section, plus AToF veto and ToF total energies for both the EM and hadronic (HAD) section. The IET is not used in this analysis and will not be described.

The ToF/AToF trigger is separated into two distinct branches for both EM and HAD sections; the Anti-ToF (AToF) veto which is designed to reject out-of-time background events at the level of minimum ionizing particles, and the ToF/AToF energy sums (E_{tot}) which generate trigger information from the global energies in SPACAL. Four E_{tot} bits (ToF/AToF for EM and HAD) are sent to L1. In order to ensure that physics events with a small ToF contribution are not triggered, the E_{tot} triggers are validated by comparing the magnitude of the ToF and AToF energies.

For the EM section, upstream proton induced beam-gas and beam-wall background interactions and physics interactions are separated by approximately 10 ns.

Chapter 4

Data selection

In this chapter the event selection used to extract the differential diffractive photoproduction cross section will be presented. First, the kinematical variables describing diffractive processes at vanishing Q^2 will be reviewed. Afterwards the different triggers which are used to collect the minimally biased photoproduction events are introduced as well as two Monte Carlo models, i.e. PHOJET and PYTHIA which are used to correct the data for limited detector acceptances, resolutions and smearing effects. Analysis cuts to select clean photoproduction samples are reviewed, followed by the diffractive cuts used to select proton elastic events. The method used to reconstruct the invariant mass of the photon dissociative system is discussed. Control plots to check that the Monte Carlo describes the data are discussed at the end of the chapter.

4.1 Introduction to the kinematic variables

The invariants describing the different processes (see figure 2.7) involving the diffractive photoproduction cross section are W^2, t, M_X^2 and M_Y^2 and will be reviewed below, neglecting the proton and electron masses.

In the photoproduction limit $Q^2 \to 0$, the square of the centre of mass energy of the γp-system, can be expressed in terms of the Bjorken variable y and the centre of mass energy of the ep-system s, as

$$W^2 = y\, s. \tag{4.1}$$

The Bjorken scaling variable y becomes in the photoproduction limit where the scattered electron has very small angles with respect to the beam,

$$y = \frac{E_\gamma}{E_e} = \frac{E_e - E_e'}{E_e} \tag{4.2}$$

here E_γ denotes the energy of the exchanged photon, being the difference of the incoming electron energy E_e and the scattered electron energy E_e'. Invoking energy and momentum conservation, the variable y, may also be obtained from the full hadronic final state, h,

according to

$$y = \frac{(E_h - p_{z,h})}{2E_e} \tag{4.3}$$

where E_h and $p_{z,h}$ represent the total energy and the momentum allong the z-axis of the hadronic final state. Substituting formula 4.2 into 4.1 expresses W in terms of the energy of the scattered electron energy

$$W = \sqrt{s\ \left(\frac{E_e - E'_e}{E_e}\right)}. \tag{4.4}$$

The square of the momentum transfer t,

$$t = (P - Y)^2, \tag{4.5}$$

where P and Y denote the initial and final proton four-momenta respectively, can be seen as the invariant mass of the propagator, here generically referred to as the pomeron. The invariant mass at the photon vertex is given by,

$$M_X^2 = (q + (P - Y))^2, \tag{4.6}$$

while the invariant mass at the proton vertex is given by,

$$M_Y^2 = (P - (P - Y))^2. \tag{4.7}$$

Experimentally the invariant mass M_X^2 is reconstructed by summing up all particles detected in the photon fragmentation region using following expression:

$$M_X^2 = \sum_i (E_i^2 - p_i^2). \tag{4.8}$$

Another extensively used variable is the pseudo rapidity (η) of a particle, deduced from the rapidity,

$$y = \frac{1}{2} \ln \frac{E + p_z}{E - p_z} \tag{4.9}$$

when the particle mass is small compared to p_z and is given by the expression:

$$\eta = -\ln \left(\tan \frac{\theta}{2}\right). \tag{4.10}$$

Here θ is the polar angle of the particle with respect to the proton beam-axis. To illustrate the particle acceptance of the various H1 detector components which are important in the present analysis, figure 4.1 shows the detector boundaries for the LAr and SPACAL calorimeters as well as for the forward detectors FMD and PRT as a function of rapidity and angle. It should be emphasized that the figure only gives the geometrical acceptance. In practice the acceptance is increased due to re-interactions of forward going particles with beam-collimators and/or beam-magnets. To discuss acceptances, event topologies and rapidities, Monte Carlo generators are needed.

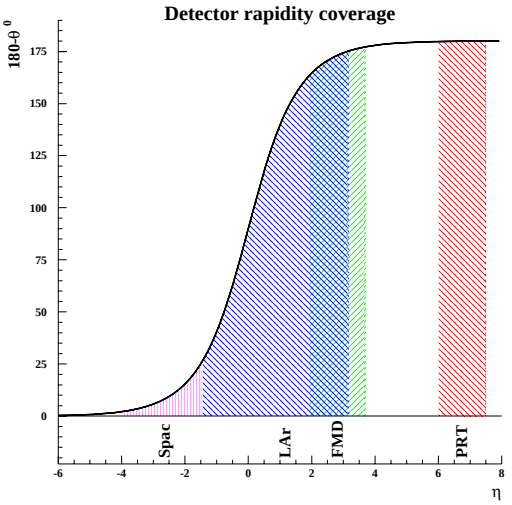

Figure 4.1: *180 - polar angle versus pseudo rapidity. The geometrical detector acceptances for the detectors of interest are indicated.*

4.2 Monte Carlo models

Detailed Monte Carlo simulations are indispensable for the extraction of physical quantities. They are used to correct for limited geometrical acceptance of the detectors and to understand the effects of the measurement resolution on kinematical variables.

They are indicative in developing the data selection cuts to separate signal from background events. In developing the cuts and determining the acceptance corrections, it is necessary that the Monte Carlo simulations describe the data well. This means that detailed simulations of the detector apparatus must be performed, including active as well as inactive materials. To know what the effect is on the acceptance correction factors obtained from one Monte Carlo model with respect to another model, at least two Monte Carlo models should be used. The mean of both acceptance correction factors can be used to correct the data with, and the difference can be assigned as an uncertainty on the derived cross section coming from the uncertainty on the different models.

The two event generators used in this analysis to simulate photoproduction reactions are those coded in the PHOJET [90] and the PYTHIA [91] Monte Carlo. Those generators are designed to describe both direct and resolved photoproduction processes. In both generators perturbative QCD calculations are used for hard sub-processes. However, the bulk of photoproduction processes contain no hard scale, and the minimally biased part of both models are based on Regge phenomenology. The unified treatment of soft and hard sub-processes, allowing a continuous transition between them, is based on an unitarization scheme in both generators. The two Monte Carlos produce all four types of interactions shown in figure 2.7 as well as non-diffractive events. An overview of how the generators produce soft diffractive events is given in the following subsections.

4.2.1 PYTHIA generator

The centre of mass energy dependence of the total γp cross section is calculated using the parameterisation of Donnachie and Landshoff (see equation (2.37)) with $\alpha_{I\!P}(0) = 1.081$ and $\alpha_{I\!R}(0) = 0.453$. In this approach the intercepts are expected to be universal, whereas the normalization parameters $A_{I\!P}$ and $A_{I\!R}$ are specific to each initial state. The total cross section is further subdivided according to

$$\sigma_{tot}(s) = \sigma_{EL}(s) + \sigma_{GD}(s) + \sigma_{PD}(s) + \sigma_{DD}(s) + \sigma_{ND}(s). \tag{4.11}$$

At not too large momentum transfers squared, t , the elastic cross section is approximated by the following exponential fall-off:

$$\frac{d\sigma_{EL}}{dt} = \frac{\sigma_{tot}^2}{16\pi} exp\,(B_{EL}t) \tag{4.12}$$

with a slope parameter $B_{EL} \sim 11$ GeV^{-2} at HERA energies. The diffractive cross sections are given by

$$\frac{d\sigma_{GD}}{dt\; dM_X^2} = \frac{g_{I\!P I\!P I\!P}}{16\pi}\beta_{\gamma I\!P}\beta_{pI\!P}^2\frac{1}{M_X^2}\; exp\,(b_{GD}t)\, F_{GD}(M_X^2, s) \tag{4.13}$$

$$\frac{d\sigma_{PD}}{dt\; dM_Y^2} = \frac{g_{I\!P I\!P I\!P}}{16\pi}\beta_{\gamma I\!P}^2\beta_{pI\!P}\frac{1}{M_Y^2}\; exp\,(b_{PD}t)\, F_{PD}(M_Y^2, s) \tag{4.14}$$

$$\frac{d\sigma_{DD}}{dt\; dM_X^2\; dM_Y^2} = \frac{g_{I\!P I\!P I\!P}^2}{16\pi}\beta_{\gamma I\!P}\beta_{pI\!P}\frac{1}{M_X^2}\frac{1}{M_Y^2}\; exp\,(b_{DD}t)\, F_{DD}(M_X^2, M_Y^2, s). \tag{4.15}$$

Since these Regge formulae for single and double diffractive events are supposed to be valid in certain asymptotic regions of the total phase space, arbitrary factors F_{GD}, F_{PD} and F_{DD} are introduced in order to obtain sensible behavior in the full phase space. The expressions for the factors can be found in [91] and contain free parameters which are extracted from fits to pp- and $p\overline{p}$-data. They suppress production close to the kinematical limit $M_X^2 \to s$ and DD configurations where the two diffractive systems overlap in rapidity space. Finally they contain a term which gives an enhancement of the low-mass region where a resonance structure is observed in the data. The triple pomeron coupling $g_{I\!P I\!P I\!P}$ and the couplings of the pomeron to the external particles $\beta_{\gamma I\!P}$ and $\beta_{pI\!P}$ are constrained by low energy data. The slope parameter of the single dissociation processes is weakly mass dependent, and is given by

$$b(s) = 2b_0 + 2\alpha' \ln\left(\frac{s}{M_X^2}\right) \tag{4.16}$$

giving a logarithmic shrinkage in s/M_X^2, with $\alpha' = 0.25$ GeV^{-2}. The b_0 term protects single dissociation from breaking down. The slope parameter for PD, b_{PD}, is taken to be approximately one unit larger than that for GD at the same final state mass, and both are typically around half of the value for the elastic process. The slope parameter for double dissociation has a logarithmic dependence on the square of both dissociation masses, and is typically around 2 GeV^{-2}.

The kinematic range in t depends on all the masses of the problem. GD events are generated starting at a threshold of $M_X = M_\rho + 0.2$ GeV. A light diffractive system, with a mass less than 1 GeV above the mass of the ρ meson, is allowed to decay isotropically into a two-body state. Single-resonance diffractive states, such as the ρ' are therefore not generated explicitly but are assumed described in an average, smeared-out sense.

A more massive diffractive system is subsequently treated as a string stretched along the γp-interaction axis, with quantum numbers of the original hadron. The particles produced in the string development are distributed in a longitudinal phase space with limited transverse momentum.

4.2.2 PHOJET generator

Also in the PHOJET generator the total cross section is modeled as a sum of pomeron and reggeon contributions. The effective pomeron and reggeon intercepts are determined in fits to pp- and $p\overline{p}$-data.

The elastic cross section is treated in a similar way to the PYTHIA case. The differential elastic cross section is also given by equation (4.12). The default slope parameters used for HERA energies are for quasi-elastic ρ, ω and ϕ production $b_\rho = 11$ GeV^{-2}, $b_\omega = 10$ GeV^{-2} and $b_\phi = 6$ GeV^{-2}. The mass distributions of the vector mesons are calculated from the relativistic Breit-Wigner resonance formulae. In case of ρ^0 photoproduction, the mass is sampled from the Ross-Stodolsky parameterization.

In single diffractive dissociation, the mass M_D of the diffractively produced particle system is calculated according to the triple pomeron kinematics. In the case of diffractive dissociation of particle A with a quasi-elastically deflected particle B the differential cross section is generated following:

$$\begin{aligned}\frac{d^2\sigma}{dt\, dM_D^2} &= \frac{1}{16\pi} g_{I\!P,A}(0) g_{I\!P I\!P I\!P}(0) g^2_{I\!P,B}(0) \left(\frac{s}{s_0}\right)^{2\alpha_{I\!P}-2} \left(\frac{s_0}{M_D^2}\right)^{\alpha_{I\!P}} \\ &\quad \times \exp\{2b_{I\!P}(M_A^2, M_B^2, M_D^2)t\}. \end{aligned} \tag{4.17}$$

This formula is valid in the triple regge limit. The limits for the diffractively produced mass in a collision with centre of mass energy $\sqrt{s}$ are given by the mass m_A of the diffractively dissociating particle itself

$$M^2_{D,min} = (m_A + M_\Delta)^2 \tag{4.18}$$

and

$$M^2_{D,max} = (m_\pi/m_B)s. \tag{4.19}$$

The t-dependence is sampled from a single exponential distribution with mass dependent slope

$$b = 2b_{I\!P}(m_A^2, m_B^2, m_{A'}^2, m_{B'}^2) \tag{4.20}$$

$$\begin{aligned} &= b_A e^{-c(m_A - m_{A'})^2} + b_B e^{-c(m_B - m_{B'})^2} \\ &\quad + 2\alpha'(0) \ln\left(2 + \frac{s s_0}{(m_A + m_{A'}^2)(m_B + m_{B'}^2)}\right) \end{aligned} \tag{4.21}$$

where m_A, m_B and $m_{A'}$, $m_{B'}$ are the masses of the incoming and outgoing particles or the diffractive excitations respectively. This slope parameterization gives a steady transition from elastic scattering to single and double diffractive dissociation. For quasi-real photons the ρ mass is used instead of the photon virtuality since it acts as hadronic scale of the photon. The parameters b_A, b_B and c are determined by cross section and slope fits and are given in [90].

The low mass resonance structure is approximately taken into account by a suppression factor for low masses, which is compensated afterwards by adding resonances to the mass distribution according to the finite mass sum rules (FMSR). Those are an extension of the finite energy sum rules (FESR) which are based on duality. In the dual description of the total cross sections the low energy region is best described by s-channel resonance production while at high energy the behavior is well described by reggeon t-channel exchanges. FESR states that the two descriptions are equivalent implying that the high energy behavior extrapolated in the low energy region describes well the average cross section behavior. A similar description applies to the diffractive cross section where the relevant variable is M_X^2 rather than s, hence the name FMSR.

4.3 Event topology

As shown in equation (2.59), the differential cross section in $\xi = x_{I\!P}$ due to a single Regge trajectory $\alpha(t)$ is given by;

$$\frac{d\sigma}{d\xi} \propto \left(\frac{1}{\xi}\right)^{2\alpha(t)-1} \tag{4.22}$$

where $\xi = M_X/W$. As the pomeron has the largest intercept of all trajectories, the events with a large rapidity gap are mainly of diffractive origin and favor small values of ξ. This explains why in the past diffractive process measurements have been studied in the range $\xi \in [0.05, 0.1]$.

From the rapidity definition, equation (4.9), one also deduces that $\ln \xi$ is the rapidity of an undecayed state X with mass M_X in the centre of mass system with energy W:

$$\eta_X^\star = \ln \xi = \ln \frac{M_X}{W}. \tag{4.23}$$

If the mass M_X decays isotropically in the centre of mass, the resulting rapidity distribution has an approximately Gaussian distribution with a half width $\Delta\eta$ with little dependence on M_X such that the maximum rapidity is given by:

$$\eta_{max}^\star = \ln \frac{M_X}{W} + \Delta\eta. \tag{4.24}$$

To calculate the η_{max} in the laboratory system an additional term ΔY has to be introduced to account for the Lorentz boost between the frames. The values ΔY for the different centre of mass energies W are given in table 4.1

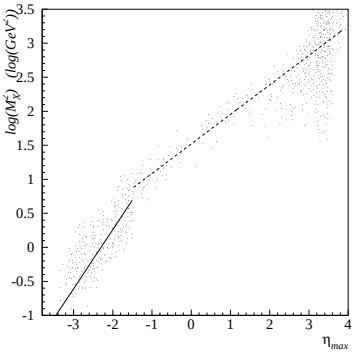

Figure 4.2 *The correlation between η_{max} and $log(M_X^2)$.*

$\langle W \rangle$	ΔY
231 GeV	1.96
187 GeV	2.17
91 GeV	2.90

Table 4.1 *The Lorentz boost factor ΔY between the centre of mass reference system and the laboratory system as a function of the centre of mass energy $\langle W \rangle$.*

For larger dissociative masses M_X, corresponding to the triple Regge region, multi-peripheral models [92] give a good description of the rapidity distribution which are flat and have a half width at half max of:

$$\eta_{max} \propto \ln\left(\frac{M_X^2}{\mu\, W}\right). \tag{4.25}$$

Both equations (4.24) and (4.25) describe the data well for $\Delta\eta$= 0.7 units and μ= 1500 MeV as extracted from figure 4.2.

Not only diffractive but also non-diffractive events can exhibit a large rapidity gap. However the larger gaps are exponentially suppressed in contrast to the diffractive events. Indeed, from the triple Regge expansion one finds that $dN/dM_X^2 \propto 1/M_X^2$ which combined with equation (4.25) shows that:

$$\frac{dN}{d\eta_{max}} = \frac{dN}{dM_X^2}\frac{dM_X^2}{d\eta_{max}} \propto \frac{1}{M_X^2} M_X^2 \propto \text{constant}. \tag{4.26}$$

4.4 Cross section definition

If we would extract the differential photon dissociative cross section $d\sigma(\gamma p \to Xp)/dM_X^2$ from the rapidity gap data by subtracting the others like non-diffractive and double dissociative events as background, it is clear that the result will depend strongly on the modeling of the processes in the given Monte Carlo. In order to minimize uncertainties resulting from Monte Carlo background subtractions, a cross section definition will be introduced which is experimentally well defined.

To this end, each event, diffractive or not, will be interpreted in terms of the generic process $\gamma p \to XY$, where X and Y represent two systems separated by the largest rapidity gap in the event. Y is defined as the system closest to the proton direction.

In order to reject the proton dissociative, double dissociative events and non-diffractive events from the event sample, the forward detectors and the forward part of the LAr are used. Although the mass of the Y-system can not be measured, it can be shown that dissociative masses with $M_Y > 1.6$ GeV and $\mid t \mid < 1$ GeV^2 can be detected in the forward detectors. Only 3% of the proton dissociative events (i.e. PD and DD) where no signal in the forward detectors was observed, had an $M_Y > 1.6$ GeV or $\mid t \mid > 1$ GeV^2. Hence the photon dissociation cross section that will be measured is given by the expression:

$$M_X^2 \left. \frac{d\sigma(\gamma p \to XY)}{dM_X^2} \right|_{M_Y<1.6 \text{ GeV}, \ |t|<1 \text{ Gev}^2} . \tag{4.27}$$

This expression is completely defined at the hadron level and fairly insensitive to Monte Carlo process modeling. As the separation of the final state by the largest event gap into system X and Y are fundamental to the cross section definition, one can ask the question whether the largest gap in the event always coincides with the separation of the photon and proton system at generator level from the diffractive event. Figures 4.3.a-d show the difference between the generated mass of the photon system M_γ^{gen} and the generated mass of the X-system M_X^{gen} as a function of M_γ^{gen} for the respective generic processes, EL, PD, GD and DD. From figure 4.3.a and c one concludes that the masses M_X^{gen} and M_γ^{gen} for the event samples EL and GD where $Y \equiv p$ are identical. In contrast, for the event samples where the Y-system fragments, i.e. PD and DD (figures b and d), the masses M_X^{gen} and M_γ^{gen} differ substantially, indicating that the largest gap found in the event does not coincide with the "diffractive" gap separating the photon and proton final state particles, and hence resulting in a wrong M_X^{gen}, M_Y^{gen} mass estimate. This is indeed understandable since for high proton dissociative masses M_P^{gen} the Y-system will be spread out in the polar angle θ, entering the particles from the photon system. This means that restricting the masses of the photon and proton system, i.e. M_γ^{gen} and M_P^{gen} to low values, the largest gap should coincide with the generic "diffractive" gap of the event, leading to good estimates of the generated masses. This can be seen in figure 4.4 where the difference between M_X^{gen} and M_γ^{gen} for PD events is shown as a function of the mass of the proton system M_P^{gen}, from which it is clear that the gap finding algorithm starts to fail to find the right mass for M_P^{gen} values above 25 GeV. In order to make a largest gap separation for DD events coinciding with the "diffractive" gap, both M_P^{gen} and M_γ^{gen} have to be small, since otherwise final state particles from the photon system would overlap in the polar angle θ with final state particles from the proton system, leading to the destruction of the "diffractive" gap and thus to a wrong estimate of the masses from the X and Y-systems M_X^{gen} and M_Y^{gen}.

4.5 Selection of minimally biased photoproduction events

4.5.1 Data selection

The minimally biased tagged photoproduction data used in this analysis were collected during a short dedicated run in 1997. In this period, HERA collided E_p= 820 GeV protons with E_e = 27.5 GeV positrons. Only those events are selected where all components of

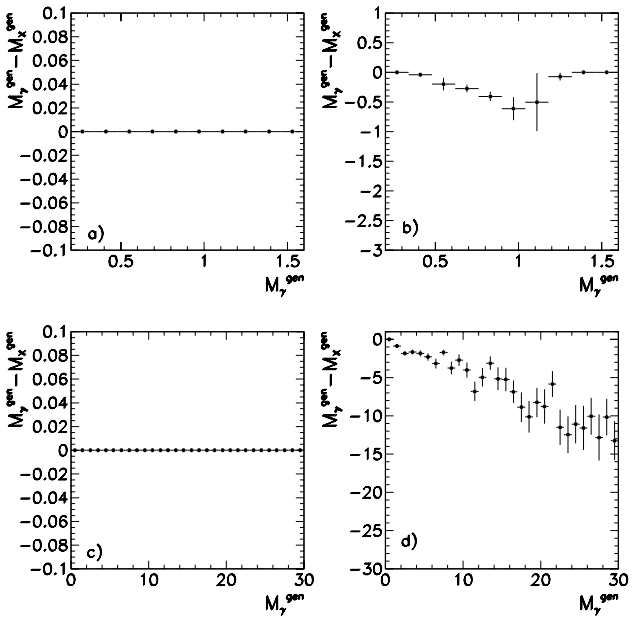

Figure 4.3: *The difference between the true generated mass M_γ^{gen} and the mass M_X^{gen} found after the separation of the X- and Y-system on the basis of the largest gap, presented as a function of M_γ^{gen} for EL processes a) for PD b) for GD c) and for DD d).*

the detector which are relevant for the analysis were fully operational. This is achieved on an event-by-event basis where the status of the following systems was checked: CJC, CIZ, COZ, CIP, COP, SPACAL, BDC, LAr, PRT, FMD and the luminosity system.

Since in photoproduction the incoming electron scatters backwards [1] at very small angles with respect to the incident proton, the scattered electron can be measured either in the electron tagger of the luminosity system at $z = -44$ m in the kinematic domain $Q^2 < 0.01$ GeV^2/c^2 and $0.04 < y < 0.2$ or in the electron tagger at $z = -33$ m covering the same Q^2 domain but for the y-interval $0.3 < y < 0.7$.

Events were collected on the basis of the following 4 subtriggers (see table 4.2). The first subtrigger `S69` requires a coincidence of a signal ($E_{e'} > 7.2$ GeV) from the electron tagger (ET33) of the luminosity system, and a T0 signal from the z-vertex sub-system trigger (see section 3.9.1), indicating activity in the central part of the detector. This trigger is very powerful in selecting ep-interactions in which the photon system dissociates into a high mass system leading to a high track multiplicity in the central detector. The second trigger `S70` requires a coincidence of trigger elements from the electron tagger (ET33) and from the Spacal TOF trigger (see section 3.9.2). Subtrigger `S70` is especially efficient for the detection of particles leaving the interaction region in the backward direction, close to the beam-pipe. Therefore `S70` will be of particular interest in triggering the lowest photon

[1] See definition on page 41.

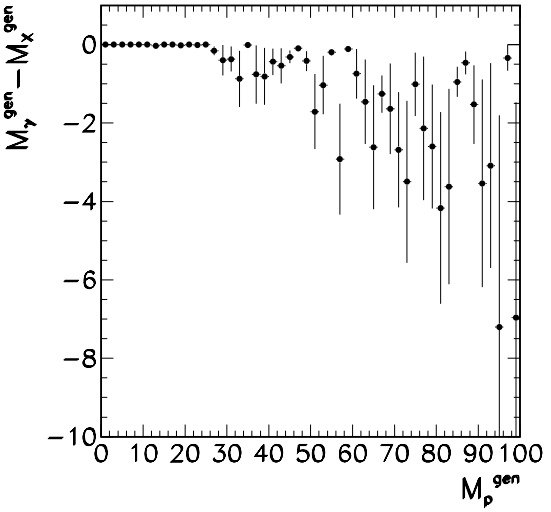

Figure 4.4: *The difference between the true generated mass M_γ^{gen} and the mass M_X^{gen} found after the separation of the X and Y-system on the basis of the largest gap, presented as a function of M_P^{gen} for the PD process.*

Subtrigger	*Trigger element composition*	*Triggers*
S69	eTAG	671 889
S70	eTAG && SPCLe_ToF_E_1	904 719
S80	etag_44	88 814
S105	etag_44 && SPCLe_ToF_E_1	167 933

Table 4.2: *The used Etag triggers and their statistics obtained after the detector status check.*

dissociative masses situated in the backward part of the detector (see figure 4.8). The two subtriggers S80, S105 used in this analysis are similar to the S69 and S70 subtriggers but with the electron tagger (ET33) trigger element substituted by the ET44 trigger element. The ET44 trigger element is set when the energy deposited in the tagger exceeds 10 GeV.

All of the subtriggers used in this analysis, also contain vetoes to reject non-ep-interactions in which signal is detected in the background time window of the TOF and FTOF scintillators (see section 3.5). To suppress events in which a photon was radiated off the incoming electron (Bremsstrahlung), leading to a lower measurement of the electron energy in one of the electron taggers affecting the photon proton centre of mass energy, a veto condition on the photon detector on level 4 of the trigger system was also required ($E_{PD} < 5.6$ GeV).

The subtriggers from table 4.2 are not completely independent. In particular for high photon dissociative masses where a high number of particles will be produced in the central

and backward part of the detector, `S69` and `S70` will both be validated in most cases. This explains why about one third of the events which were validated by subtrigger `S69` were also validated by `S70`.

4.5.2 Downscaled triggers and the event weights

With a high input (event) rate which occurs at the beginning of a luminosity fill and a limited rate of 50 Hz with which the events can be logged to tape, the recorded event sample would be dominated by events at low Q^2. In order to preserve interesting events at high Q^2, all subtriggers corresponding to low Q^2 processes were downscaled. When towards the end of a luminosity fill the event logging rate was reduced well below 50 Hz, the downscale factors were gradually decreased and eventually set to one. Every change in downscale factors was marked by a new "run". The maximum event rate attributed to the minimum bias triggers was limited to 30 Hz. As the S80 and S105 subtriggers are more background contaminated than the subtriggers S69 and S70, the latter downscale factors were reduced first. Due to the variations in the downscaling of various subtriggers in different runs, the events have to be weighted.

If d_{ijk} represents the downscale factor of event i for subtrigger j in run k, then the probability that event i will be triggered is

$$P_{ijk} = \frac{1}{d_{ijk}}. \tag{4.28}$$

If there are several subtriggers simultaneously possible with different downscale factors, then the probability that any of them leads to a trigger is

$$P_{ik} = 1 - \Pi_{j=1}^{N_{subtrig}}(1 - \frac{1}{d_{ijk}}). \tag{4.29}$$

Using the inverse of P_{ik} as an event weight, would attribute the correct rate to all triggers as if not downscaled. However some of those weights could be large in runs with a large downscale factor and a small luminosity. These large uncertainties can be avoided by weighting the triggering probabilities over the full run range. If L_k is the luminosity of run k we define the overall event weight by

$$w_i = \frac{\sum_{k=1}^{N_{runs}} L_k}{\sum_{k=1}^{N_{runs}} L_k P_{ik}}. \tag{4.30}$$

These are the event weights used in this analysis.

4.5.3 Electron tagger acceptance

The electron tagger at 33 m performs a double function. It both tags γp-events and provides a measurement of the scaling variable y. Since this analysis is based on a tagged photoproduction sample and the geometrical acceptance of the electron taggers is limited, an acceptance $\mathcal{A}_{ET}(y, Q^2)$ has to be calculated.

This electron tagger acceptance, shown in figure 4.5, depends on the following HERA parameters:

- the electron beam-tilts (θ_x, θ_y)
- the offset of the electron beam-trajectory ($\Delta_{x_{off}}$, $\Delta_{y_{off}}$) with respect to the nominal H1 interaction point.

Due to the bending of the electron beam in the x direction, θ_x and $\Delta_{x_{off}}$ are the most important, while the vertical tilt and offset can be ignored to first order. A method exists to determine the over Q^2 integrated acceptance $\mathcal{A}(y)$ for an inclusive photoproduction data sample. First, the acceptance $\mathcal{A}^{BH}(y)$ for the Beite-Heitler events $ep \to e\gamma p$ is measured. Then the Monte Carlo simulation was tuned to the data by varying $\Delta_{x_{off}}$, being the only free parameter in the procedure since θ_x can be measured by monitoring the position of the photon spot at the photon detector. Finally, the acceptance $\mathcal{A}(y)$ can be calculated using the measured tilt θ_x and the tuned value of $\Delta_{x_{off}}$. A limited range of $0.3 < y < 0.7$ was used in this analysis, to avoid low acceptance regions. Within this interval the integrated tagger acceptance is accurate to 3 - 5 %.

The electron tagger at 44 m being about three times smaller than the electron tagger at 33 m, has a very small acceptance window and as a consequence a very poor energy resolution, such that it only serves as triggering purpose. Once this electron tagger measures an energy above threshold (i.e. 6 GeV) the electron energy had a value of $E_{e'} = 24.5$ GeV, equivalently to a photon proton centre of mass energy of $\langle W \rangle = 91$ GeV.

In this analysis the available y-range of the electron tagger at 33 m is further subdivided into two intervals leading to different mean photon proton centre of mass energies $\langle W \rangle$= 187 and 231 GeV (see table 4.3). While for the electron tagger at 44 m one centre of mass energy bin was obtained, i.e. $\langle W \rangle$= 91 GeV.

ET-detector at	y-interval	$\langle W \rangle$
44 m	$[0.05 - 0.2]$	91 GeV
33 m	$[0.3 - 0.5]$	187 GeV
33 m	$[0.5 - 0.7]$	231 GeV

Table 4.3: *The y-intervals with their corresponding γp centre of mass energies.*

4.5.4 Photoproduction event sample

Analysis cuts are applied to the data samples obtained with the four different subtriggers, to remove events from background sources and events for which the scattered electron energy is poorly measured.

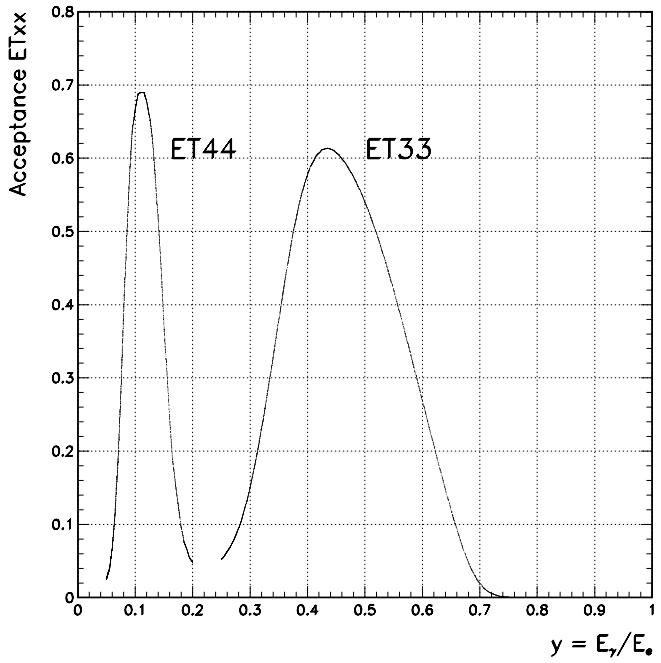

Figure 4.5: *The electron tagger acceptances as a function of the inelasticity variable y. For each of the electron tagger calorimeters an acceptance curve is shown.*

A cut on the local x-coordinate of the centre of gravity of the electron cluster, $|x_{tag}| < 6.5$ cm, in the electron tagger (ET33), is applied (see section 3.7). This is a typical cut to avoid that the scattered electron energy is poorly measured.

Because of the high rate, Bremsstrahlung events ($ep \to ep\gamma$) can overlap in time with an ep-interaction in which a z-vertex T0 or a `SPCLe_ToF_E_1` has fired and hence constitute a serious background in the photoproduction event sample. However these events can easily be rejected by imposing a cut on the energy (E_{PD}) deposited in the photon detector of the luminosity system. The energy measured in the photon detector (E_{PD}) was required to be below 2 or 0.6 GeV for respectively the ET33 or ET44 sample. These values correspond to those used in the determination of the electron tagger acceptances.

After these cuts the main background in the photoproduction event sample is due to beam induced background; mainly electron beam interactions with residual gas. Most of these events can be eliminated using the following two criteria.

The first criterion is based on the vertex distribution. As beam-gas interactions have a uniformly distributed vertex, in contrast to the genuine ep-interactions for which a peaked z-vertex distribution around the interaction point is seen, the following requirement was imposed: if a vertex was present it was constrained to be in the interval $[-30, 30]$ cm. With such a conditional cut, events with low multiplicities still remain after the cut.

The second criterion is based on the quantity $y_{had} = \sum_i (E_i - P_{z,i})/2E_e$ where the index i runs over all final state particles excluding the final state electron and with E_e the incoming electron energy. Figure 4.6.a and b show the quantity y_{had} for the z-vertex and SPACAL triggered event sample at $\langle W \rangle = 231$ GeV. One sees that for genuine ep-interactions at a mean centre of mass energy $\langle W \rangle = 231$ GeV the distribution is centered around a value of 0.6, while for e-residual beam-gas interactions this mean value is expected to be at lower values and should be identical to the distribution obtained with the "e-pilot bunch" event sample. The beam induced background is clearly visible in the SPACAL triggered event sample which dominates the genuine ep events, and is well reproduced by the e-pilot event sample [2]. Comparison of figure 4.6.a and b shows that the requirement of a z-vertex T0 trigger (see section 3.9.1) vastly suppresses the background.

To reject these beam induced background events a cut is performed on y_{had} (see table 4.4). In order to calculate whether the fraction of beam-gas events to genuine photoproduction ep events remaining after the cuts of table 4.4, the beam-gas events have to be normalized following the corresponding luminosity. To be able to normalize these number of electron beam-gas events a quite uncertain method exist taking the electron beam-current, the density of the beam-gas and the length over which both can interact with each other into account. Here another experimental method is used, fitting the normalization of the "pilot events" in a way that the Monte Carlo events plus the "pilot events" describe the data. The remaining beam induced background is small and amounts to 1% and 2% at respectively $\langle W \rangle$= 231 GeV and 187 GeV in the SPACAL triggered event sample. The background is even smaller in the z-vertex triggered events.

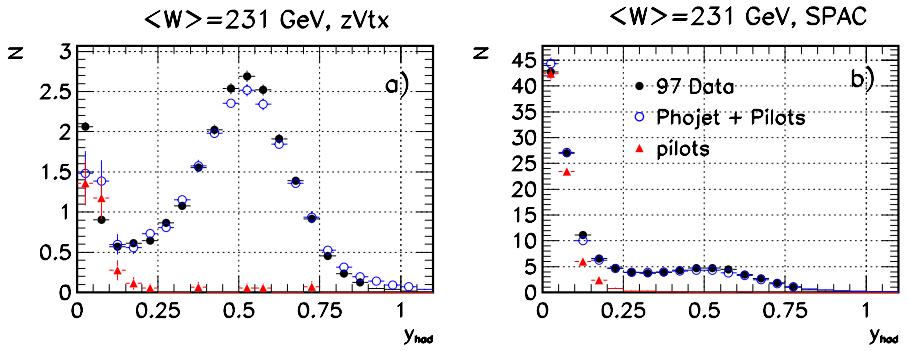

Figure 4.6: *y_{had}-distribution at $\langle W \rangle$=231 GeV for a) z-vertex triggered events and b) SPACAL triggered events.*

For the data at $\langle W \rangle$= 91 GeV, this background reducing cut on y_{had} could not be applied. The reason is that at lower W energy, the genuine ep-events have a mean value of y=0.09 and merge with the beam-gas peak. No sensible cut to reject the beam-gas can be

[2] For the normalization see next paragraph

Cut	*Purpose*
$E_{PD} < 2.0$ / 0.6 GeV	Bremsstrahlung rejection
$\|x_{tag33}\| < 6.5$ cm *	Containment of the electron energy
$0.2 < y_{had}$*	Beam induced background rejection
$\exists$ z-vertex $\in$ [-30,30] cm	Beam induced background rejection

Table 4.4: *Cuts used to select a clean photoproduction event sample. The cuts with an asterix are only applied to the ET33 triggers.*

introduced. As a result the beam induced background is large in this sample and amounts to 23% in the case of the SPACAL triggered event sample.

4.6 Selection of diffractive events

Proton elastic diffractive events are selected on the basis of a non observation of activity in the forward detector components, PRT, FMD and the forward part of the LAr and hence these detectors are used as a veto. Therefore it is important to understand their noise level, which can be investigated using "random trigger" files which contain data randomly triggered and where no specific trigger was requested. About 1% of all events written to tape are randomly triggered. Since noise in the detector components can vary in time, the study of these random triggered events is done on a sample that corresponds to the same run range as the selected data.

Figure 4.7.a shows the percentage noise level in the PRT detector as a function of the cumulative hit multiplicity. Because the low noise level, less than 0.54 % of the events will give at least one hit, the PRT "no-hit" condition was put to;

$$N_{PRT} < 1. \tag{4.31}$$

Figure 4.7b) shows the percentage noise in the FMD detector as a function of the cumulative paired hit multiplicity, where the paired hits refer only to the pre-toroid layers (see section 3.6.1). As the noise level in this detector is rather high, the condition for no signal in the FMD was set to;

$$N_{FMD} \leq 2. \tag{4.32}$$

Figure 4.7c) shows the energy distribution of the noise clusters deposited in the LAr calorimeter as a function of the polar cluster angle θ. As can be seen the noise level differs between the central ($\theta > 10^o$) and the forward part ($\theta < 10^o$) of the detector. Therefore two different noise cuts were applied: E^{thr}_{LAr}= 0.4 GeV for clusters with $\theta > 10^o$ and 0.7 GeV for clusters with $\theta < 10^o$.

The maximum pseudo rapidity of a cluster that can be measured in the LAr is set to;

$$\eta_{max} < 3.2. \tag{4.33}$$

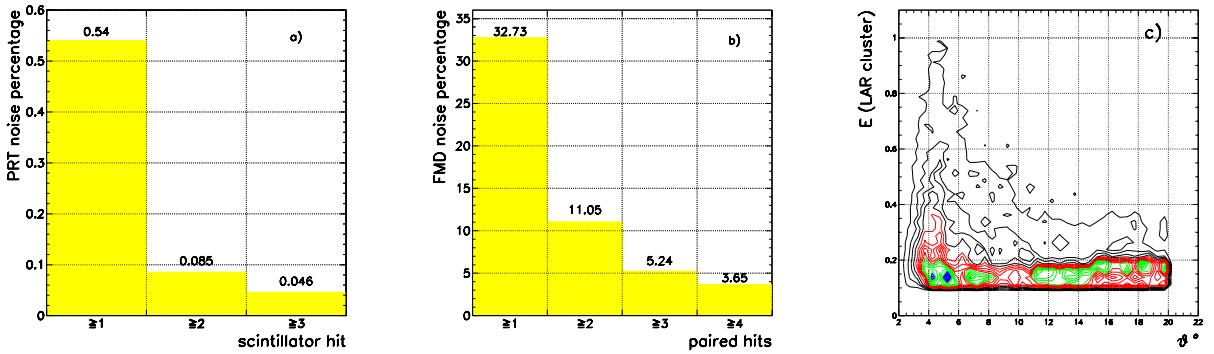

Figure 4.7: *Percentage loss of proton elastic events a) as a function of allowed number of fired scintillators of the PRT, b) as a function of the allowed paired hits in the pre-toroid layers of FMD due to random noise in the device. The energy distribution of the noise clusters is shown in c) as a function of the polar angle θ.*

Although the acceptance of the LAr is somewhat larger, the value of 3.2 was taken to guarantee full containment of the most forward cluster energy.

Figure 4.8 shows the η_{max}-distribution as predicted by the PHOJET Monte Carlo for event samples respectively tagged by the ET at 33 m and ET at 44 m. The figure also shows the contribution from the different processes: EL, GD, ND and the total contribution. Non-diffractive events producing hadronic activity in between the photon and proton fragmentation regions produce mostly energy deposits in the LAr calorimeter very near to the edge of its forward acceptance. Therefore by applying the η_{max}-cut given under (4.33) most of the non-diffractive events are rejected. A small fraction remains with an η_{max} very close to 3.2, and decreasing exponentially towards lower η_{max} values.

A second peak at low η_{max} is dominated by vector meson production since the decay particles of the vector meson are detected more in the backward region of the detector giving negative η_{max} values. In between these two peaks a relatively flat region (see equation (4.26))of predominantly GD and DD events is observed. One also sees that the maximal pseudo-rapidity shifts towards higher values for decreasing centre of mass energies, as represented by the full and dashed curve in figure 4.8.a for a centre of mass energy of respectively $\langle W \rangle = 200$ GeV (i.e. $y \in [0.3, 0.7]$) and 91 GeV.

Applying the η_{max} cut, diffractive events can be rejected due to electronic noise in the calorimeter. This effect exists but the resulting efficiency loss for diffractive events is correctly taken into account in the Monte Carlo simulations, since the random noise in the LAr is monitored over regular periods of the data and incorporated into the detector simulation automatically.

A summary of the proton elastic diffractive cuts can be found in table 4.5.

As the Monte Carlo is used to calculate the acceptance of the forward detectors, a detailed study to check the forward detectors description has been performed. In this

Cut	Description
$\eta_{max} < 3.2$	No activity in forward LAr
FMD ≤ 2	No activity in L1+L2+L3
PRT $= 0$	No activity in PRT

Table 4.5: *Selection criteria to select proton elastic diffractive events.*

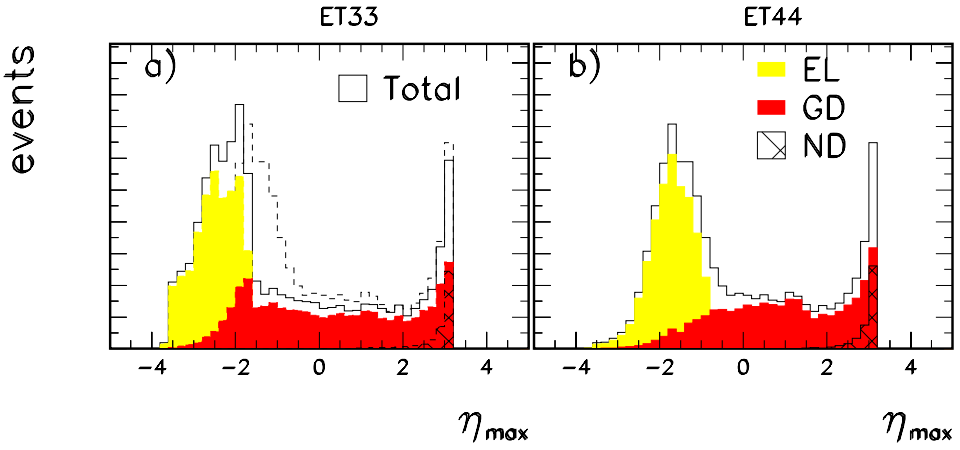

Figure 4.8: *η_{max}-distribution from the PHOJET Monte Carlos representing the ET33 (a) and ET44 (b) sample. No cuts were applied on the Monte Carlo. The hatched, dark hatched and gray distribution shows respectively the ND, GD and EL contribution from the Monte Carlo.*

study, it has been found that the PRT description does not agree with the data. The reason for this is in part due to aging of the scintillators and in part due to bad optical contact between light guide and scintillator which were only revealed after the minimum bias run had taken place. The adjustment of the Monte Carlo will be discussed in the following section.

4.6.1 PRT efficiency correction

In order to estimate the individual PRT scintillator efficiencies from the data and to correct the Monte Carlo simulation, a diffractive data sample with some activity ($E > 500$ MeV) in the forward part of the LAr ($\theta < 10^o$ or $\eta > 2.4$) and a large rapidity gap of more than 2.4 units in pseudorapidity, spanning from η=2.4 till 0, was selected. The seven figures, 4.9.a-g show the hit multiplicity of the 7 PRT scintillators for seven event subsamples,

in which respectively scintillator S_j with j going from 0 to 6 was required to have fired. The Monte Carlo prediction in each histogram is normalized to the hit multiplicity of the firing scintillator in the data. Comparison of data and Monte Carlo clearly indicate that scintillators S3 to S6 are very inefficient with respect to the simulation. The scintillator efficiencies were determined using the hit multiplicity of figure 4.9.c assuming that S2 is 100% efficient. The values obtained are shown in table 4.6. As can be seen from the grey hatched curve in figure 4.9.a, b and d-g, all hit multiplicities are well described after applying the scintillator efficiency factors to the Monte Carlo simulation.

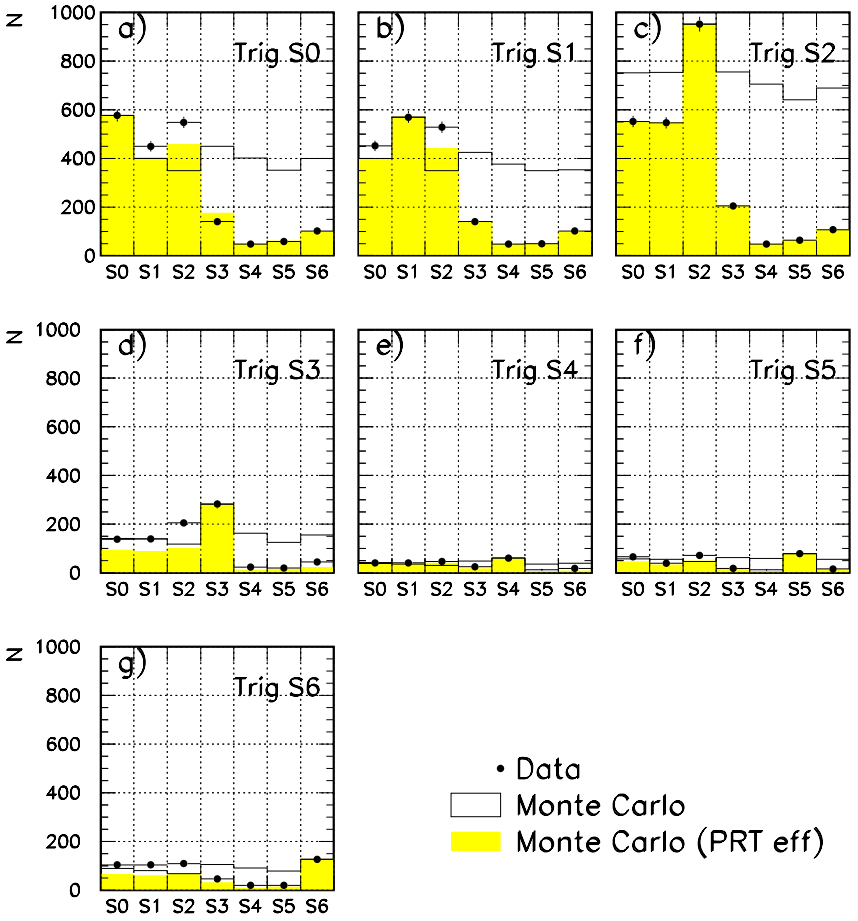

Figure 4.9: *PRT scintillator hit multiplicity for diffractive event subsamples in which respectively S0, S1, S2, S3, S4, S5 and S6 fires; the data (black dots), Monte Carlo (full line) and the PRT efficiency adjusted Monte Carlo (the grey histogram) normalized for each histogram to the multiplicity of the firing scintillator in the data.*

PRT efficiency for scintillator						
S0	S1	S2	S3	S4	S5	S6
0.77	0.78	1.00	0.30	0.08	0.10	0.19

Table 4.6: *PRT efficiencies calculated for the 1997 minimum bias run assuming S2 to be 100% efficient.*

4.6.2 Forward detector description and PRT tagging efficiency

The hit distributions in the PRT and FMD and the energy distribution in the LAr are dependent on the model assumed for the M_Y-distribution in the event generator. To cross check whether the assumed M_Y-dependence fits the data, the conditional probability for one of the forward detectors to fire, given a different forward detector causing the trigger, has been compared in data and Monte Carlo. Again the diffractive sample with $\Delta\eta > 2.4$ units has been used. Figures 4.10.a-f show the various combinations of signals recorded in one of the detectors when triggered by another. Table 4.7 shows the same results numerically. The errors are of the order of 5%. Table 4.7 shows that once a signal is recorded in the FMD or LAr (small η) the probability for recording a signal in the PRT (large η) is underestimated in the Monte Carlo with an averaged efficiency of 80% with respect to the data. In the same way one obtains that once a signal is recorded in the PRT or LAr, the Monte Carlo overestimates the FMD tagging probability with an averaged efficiency of 114%. The Monte Carlo overestimates the LAr tagging probability by 10% with respect to the data. Hence the data seems to indicate that the M_Y^δ-dependence assumed in the Monte Carlo tends to simulate too many events at large M_Y. This discrepancy in the forward detector description will be included in the final analysis as a systematic error by reweighting the M_Y^δ-distribution by $M_Y^{\pm 0.5}$.

Given a reasonable forward detector description between data and Monte Carlo, i.e. by reducing the Monte Carlos PRT estimate, one can also extract from the adapted Monte Carlo the proton dissociation tagging probability which is found to be 82±4%. The error results from a reweighting of the M_Y^δ-distribution in the Monte Carlo by $\delta = \pm 0.5$. As a consequence the background from proton dissociation in the proton elastic sample amounts to 12±6% if the ratio of proton dissociation to proton elastic is taken to be 2/3±1/3 [93]. However noise in the forward detectors may result in the loss of elastic proton events. This can be estimated from random triggered events in which it is found that the fraction of events with a hit in the PRT is 14±3%. Hence the sum of both contributions would result in a correction to the total elastic proton cross section of -2±7%.

4.7 The reconstruction of the invariant mass M_X.

After the identification of a rapidity gap in the forward direction, the invariant mass M_X^2 of the diffracted system is given in terms of the total four-vector, p_h, of the hadronic final

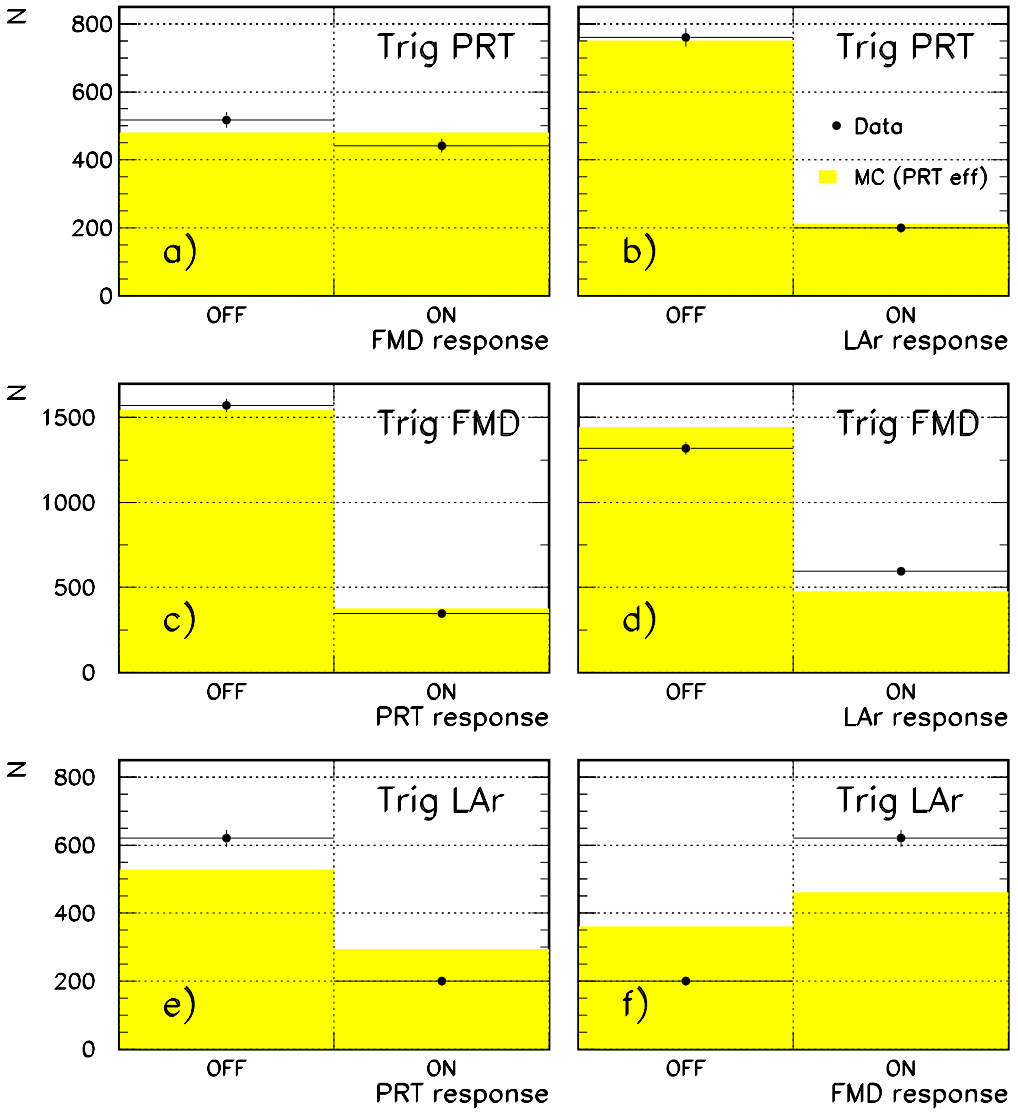

Figure 4.10: *Comparison of the tagging efficiency of one forward detector as a function of the remaining two in data and Monte Carlo. "Response ON" means that a signal has been detected. This means more than zero hits in the seven PRT scintillators, more than two paired hits in the FMD or at least one cluster above 500 MeV is observed in the forward part ($\theta < 10^o$) of the LAr.*

state associated with the photon, by

$$M_X^2 = E_h^2 - (\vec{p_h})^2 = \left(\sum_X E\right)^2 - \left(\sum_X \vec{p}\right)^2 . \tag{4.34}$$

where the sum is performed over the photon dissociation system X. In photoproduction where $Q^2 = 0$ the incident photon is colinear with the beam-axis and thus the overall

PRT tagging efficiency		
Triggered on	$\epsilon = data/MC$	combined efficiency
FMD	0.92	
LAr	0.68	$\Rightarrow$ 0.80
FMD tagging efficiency		
Triggered on	$\epsilon = data/MC$	combined efficiency
PRT	0.92	
LAr	1.35	$\Rightarrow$ 1.14
LAr tagging efficiency		
Triggered on	$\epsilon = data/MC$	combined efficiency
PRT	0.95	
FMD	1.26	$\Rightarrow$ 1.10

Table 4.7: *Tagging efficiencies for each individual forward detector determined from an event sample in which one of the two other forward detectors produced a trigger. The mean of these two efficiencies is considered as the combined tagging efficiency*

transverse momentum of the state X is zero. Equation (4.34) can be rewritten as

$$M_X^2 = (E_h + p_{z_h})(E_h - p_{z_h}). \tag{4.35}$$

The factor $(E_h + p_{z_h})$ is insensitive to particles lost in the backward beam-pipe for which $E \simeq -p_z$, while $(E_h - p_{z_h})$ is affected maximally. Therefore $(E_h - p_{z_h})$ was replaced by $2yE_e = 2(E_e - E_{e'})$ using equation (4.3) where y is calculated using the electron energy measured in one of the electron tagger calorimeters. This results in the final expression for the mass:

$$M_X^2 = 2(E_{e'} - E_e)(E_h + p_{z_h}). \tag{4.36}$$

The hadronic final state h is reconstructed by combining associations of neighboring calorimeter cells, called clusters, in the LAr and SPACAL calorimeters and tracking information [94]. The selected clusters and tracks are combined by the following procedure:

- The selected central tracks fitted to the primary vertex are extrapolated into the calorimeter.
- For each track, the energies of clusters within an extrapolated cylinder around the extrapolated impact point in the calorimeter are summed up. The radius of the cylinder is 25 cm (50 cm) in the electromagnetic (hadronic) section of the calorimeter.
- If the track energy is greater than the summed energy in the extrapolated cylinder, only the track's four-vector will be kept.
- If the track energy is smaller than the summed energy in the extrapolated cylinder, all those clusters which are near to the extrapolated track and for which the summed energy equals the track energy are removed from the cluster list.

- Calorimeter clusters behind a muon track are masked.

This procedure leads to an improved reconstruction of the hadronic final state with respect to a reconstruction in which only calorimeter information is used.

To determine the quality of the mass reconstruction the quantity δ,

$$\delta = \frac{M_X^{rec} - M_X^{gen}}{M_X^{gen}} \tag{4.37}$$

is used. Figures 4.11.a-f show δ as a function of the generated invariant mass M_X^{gen} for the two Monte Carlos, PHOJET and PYTHIA. The error bars indicate the standard deviation on the variable δ. The shift of the mean reconstructed mass towards larger negative values for large generated masses indicates that the reconstructed mass is underestimated while for the lowest M_X^{gen}-bin the mass is overestimated. The width of the reconstructed mass $\sigma(\delta)$ is relatively constant except for the lowest masses M_X^{gen}.

The underestimation of the M_X^{rec} value can be explained by a loss of particles in the forward direction. Although an η_{max} cut is applied on reconstructed "objects", it may still happen that the part of the generated particles especially for large M_X^{gen} values, escape the forward part of the LAr calorimeter. To check this hypothesis, events were generated in which all generated particles satisfied the condition $\eta_{max} < 3.2$. The result showed that the observed shift from figure 4.11 is no longer present.

The loss of particles in the forward direction is dependent on the Lorentz boost between the laboratory system and the γp centre of mass system (CMS). The larger the boost (smaller W), the more the particles are projected forward in the laboratory system. This explains why at a mean centre of mass energy of $\langle W \rangle = 91$ GeV the fractional underestimation of the reconstructed mass reaches 50% already for values of M_X^{gen} at 20 GeV, while at $\langle W \rangle = 231$ GeV this fraction is only reached at $M_X^{gen} \approx 50$ GeV. The large "under-reconstruction" will result in large mass migrations between the generated and reconstructed mass bins. In order to avoid this a correction to the reconstructed mass has been introduced.

The M_X^2-binning used in this analysis is similar to one used in a previous analysis [68] for the data at $\langle W \rangle$=231 and 187 GeV. For the lower centre of mass energy, $\langle W \rangle$=91 GeV, data sample, the last two bins have been regrouped to increase the migration/stability in this bin (see section 4.7.4). The M_X^2-binning for all data samples are shown in table 5.2.

4.7.1 Rescaling the reconstructed mass M_X

In order to determine the correction factor to compensate for the particle loss in the forward direction, the following procedure has been adopted. For every reconstructed mass bin the distribution f:

$$f = \frac{M_X(gen)}{M_X(rec)} \tag{4.38}$$

is plotted for all three W-bins and both Monte Carlos. As an example figure 4.12 shows the

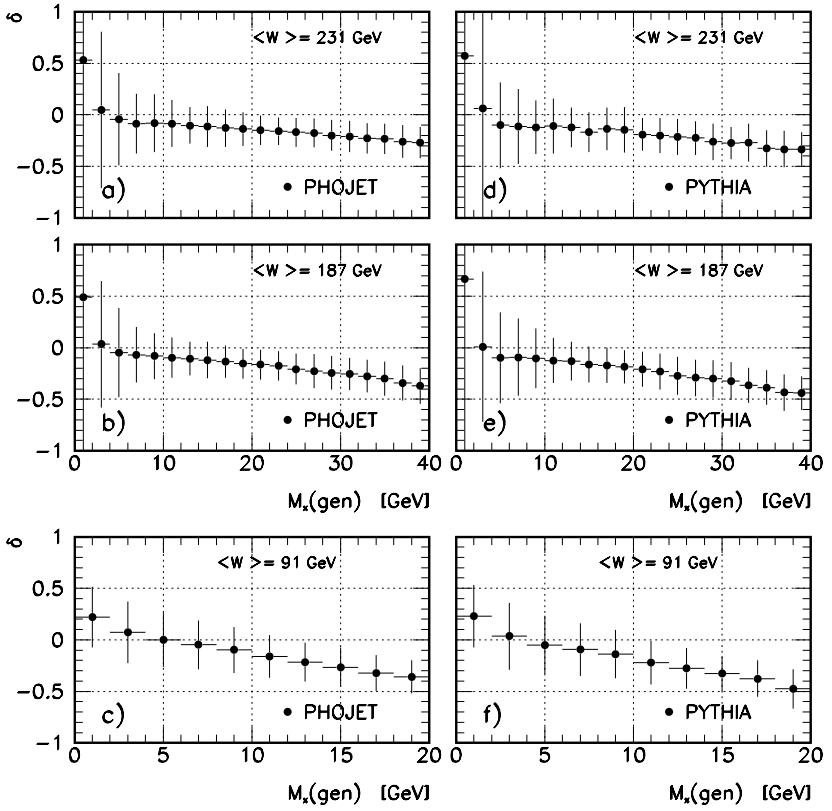

Figure 4.11: *The quantity* $\delta = (M_X^{rec} - M_X^{gen})/M_X^{gen}$ *as a function of* M_X^{gen} *for the three* W*-intervals* W *=231, 187 and 91 GeV for two Monte Carlos, PHOJET and PYTHIA. The error bars indicate the standard deviation on the quantity* δ*.*

f-distribution for $\langle W \rangle = 91$ GeV. The correction factor for each M_X^{rec} bin, being an average correction, is set to the mean value of a Gaussian fit to the f-distribution. Figure 4.13 shows the correction factors as a function of $\log_{10}(M_X^{rec})$ obtained with the two Monte Carlos for the three γp centre of mass energy intervals. From this figure one sees that both Monte Carlo models give the same rescaling factor. And only at high values of M_X^{rec} the rescaling factor deviates significantly from one. This indeed means that at high generated photon dissociative masses M_X^{gen}, particles are lost due to the limited forward acceptance of the detector and leading to lower M_X^{rec} values. This phenomenon is even stronger when the centre of mass energy gets smaller as can be seen from figure 4.13. The final correction factors that have been applied as a function of M_X^{rec} are the averages of the correction curves given by the two Monte Carlos.

The result of the application of these average correction factors on the quality of the mass reconstruction is shown in figure 4.14. Whereas the under-reconstruction of M_X^{rec} with respect to M_X^{gen}, for the two highest centre of mass energy bins started already around 5 GeV before the correction procedure was applied (see figure 4.11) it now remains flat till

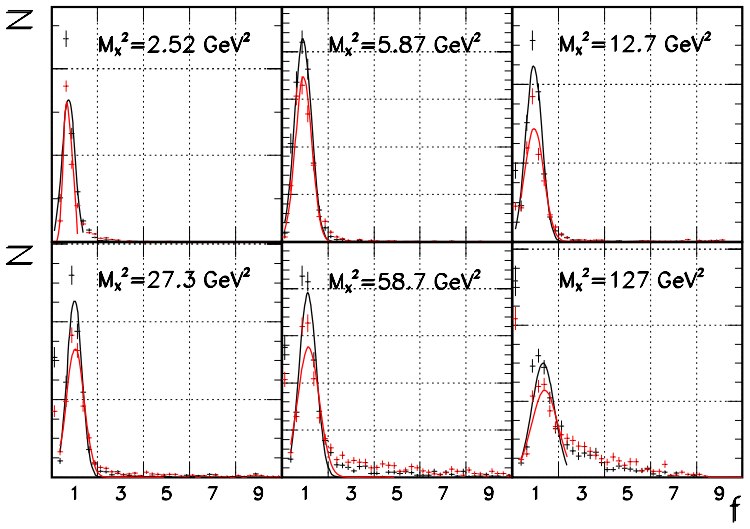

Figure 4.12: *Gaussian fit on the $f = M_X^{gen}/M_X^{rec}$-distribution for W =91 GeV for both Monte Carlos, PHOJET (black line) and PYTHIA (red line).*

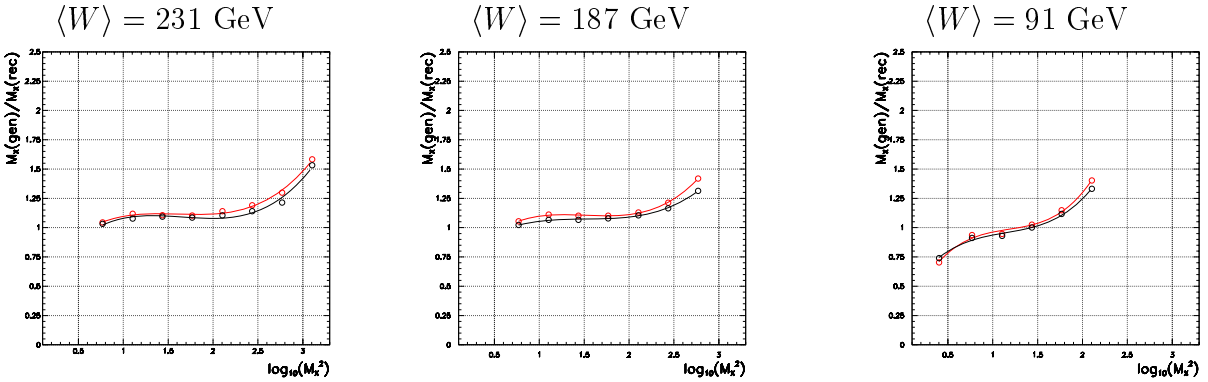

Figure 4.13: *The correction function for the mass losses in the forward part of the detector, being the mean of the f-distributions, as a function of $log_{10}(M_X^2)$. Both MC's show the same correction curve for one specific centre of mass energy.*

generated masses of 40 GeV (see figure 4.14). Also the reconstruction of the dissociating mass for the centre of mass energy $\langle W \rangle = 91$ GeV improves a lot over the whole generated mass range for both MC's.

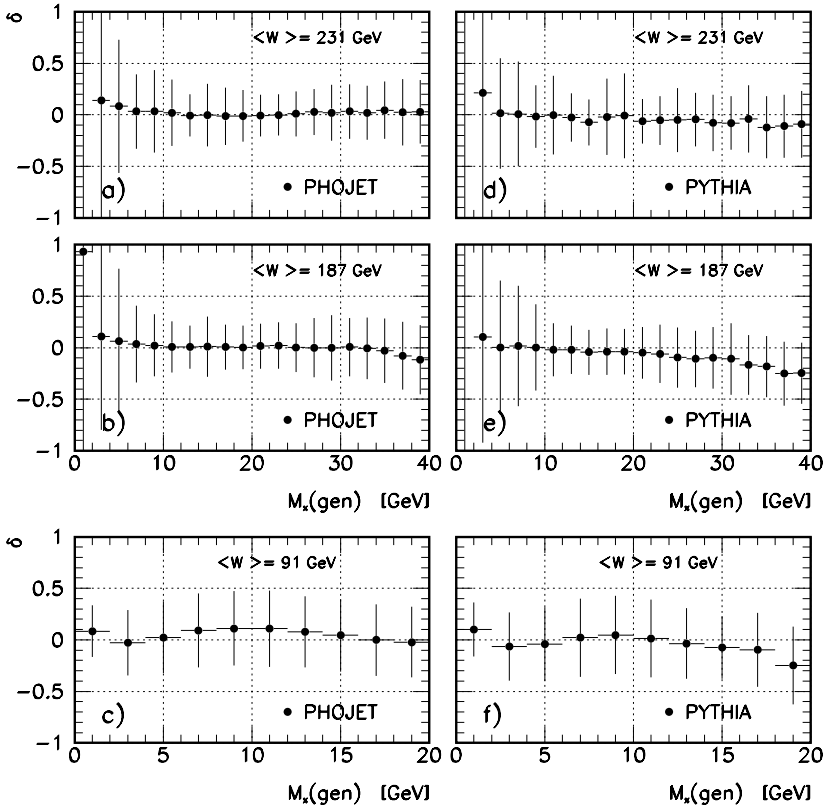

Figure 4.14: *The quantity* $\delta = (M_X^{rec} - M_X^{gen})/M_X^{gen}$ *as a function of* M_X^{gen} *for the three W-intervals W =231, 187 and 91 GeV for two Monte Carlos, PHOJET and PYTHIA after the correction for the particle losses in the forward part of the detector. The error bars indicate the standard deviation on the quantity* δ.

4.7.2 Control plots of mass distribution

After all cuts (see tables 4.4 and 4.5) and corrections, the Monte Carlo models are compared to the data, in order to test the level to which the physics and detector simulations are able to describe the data. Figure 4.15 shows the uncorrected mass distributions for the spacal sample at the three different centre of mass energies $\langle W \rangle$=231, 187 and 91 GeV. The description of the central M_X^2 values by the Monte Carlos is in good agreement with the data. Since the low mass resonances are included in the Monte Carlo simulation in a smeared out way (see section 4.2), a deviation in this low mass region can be expected between Monte Carlo and data. Also at high dissociative masses one can expect deviations between data and Monte Carlo since a boundary condition is put on the ratio M_X/W in the simulation. These discrepancies can be attributed to an incomplete process description in the Monte Carlos and hence the option was taken to reweight the mass distribution at the generator level such that the reconstructed mass in the Monte Carlo would describe the data.

The request for a good model description for M_X^{rec} is the extraction of the process acceptance. However, reweighting M_X^{gen} requires knowledge of the acceptance. Therefore in order to reweight the Monte Carlo an iterative procedure was used; the acceptance obtained in iteration i is applied to the invariant mass distribution of the data sample to recalculate an invariant mass distribution at generator level which is the input invariant mass to iteration $i+1$.

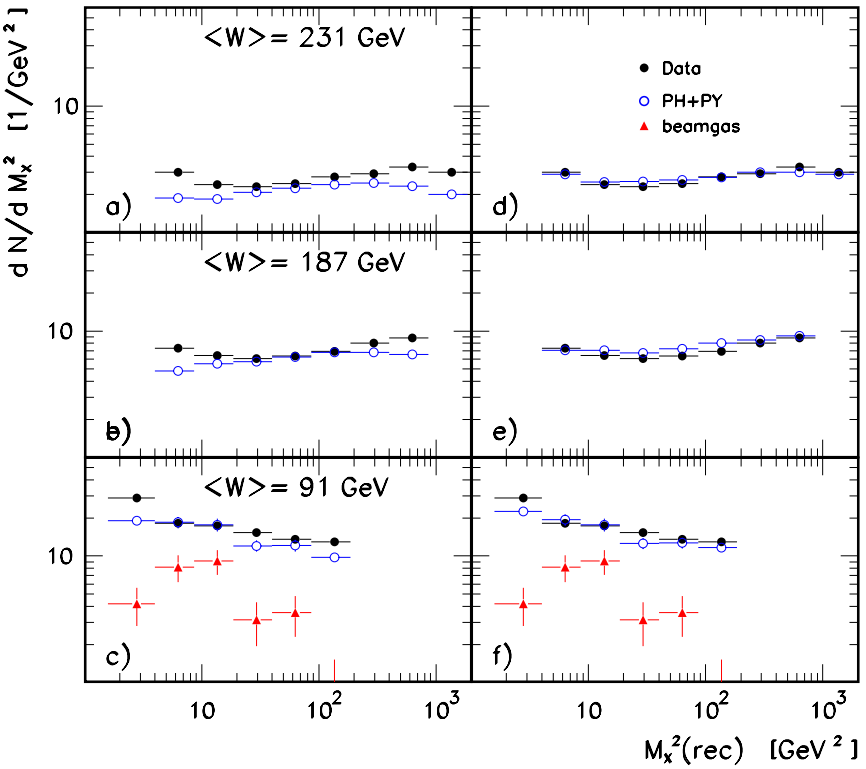

Figure 4.15: *The M_X^2-distribution for the three centre of mass energies $\langle W \rangle$ = 231, 187 and 91 GeV are shown from top to bottom. Figure a), b) and c) compare the data with the mean of the PHOJET and PYTHIA Monte Carlo, figures d), e) and f) show the improvement after the iterative reweighting procedure performed on both Monte Carlos.*

Formally:

1. The differential cross section $M_X^2\ d\sigma/dM_X^2$ for $M_Y < 1.6$ GeV and $\mid t \mid < 1$ GeV^2 of the initial Monte Carlo (MC(0)), i.e. the Monte Carlo without any weight taken into account, is determined by taking into account the bin width ΔM_X^2, the luminosity $\mathcal{L}$ and the Weizsäcker-Williams flux factor $\mathcal{F}$ [24]. Since the cross section is calculated using the generated quantities, no detector acceptance has to be considered.

2. The differential cross section is calculated on the data sample (as explained in chapter 5) using the invariant mass distribution and the trigger efficiency from the data, the electron tagger acceptance and the detector acceptance correction factors obtained from MC(0).

3. A simultaneous fit to the mass distribution for the three W-intervals is performed (triple Regge fit see chapter 6) for both Monte Carlos called "MC(0)" and data called "DATA(0)". "DATA(0)" means that data were corrected with the acceptance from MC(0) before the fit was performed.

4. The correction factors for the Monte Carlos were obtained as the ratios of the parameterized mass distributions. The first order Monte Carlo called MC(1) represents the initial generated mass distribution weighted by $w(M_X^{gen,0}) = fit(Data(0))/fit(MC(0))$. Thus,
$$MC(1) = MC(0) \times w(M_X^{gen,0}) \tag{4.39}$$
By construction, the differential cross section calculated on the first order MC is the same as the differential cross section of the data after correction with the acceptance correction factors obtained from MC(0).

The reweighted mass distribution is then used as input to the second iteration and the whole procedure is repeated until the correction factors fit$(Data(i))$/fit$(MC(i))$ converge to one. In this analysis a good convergence is obtained after 3 iterations. The results of this iterative procedure are shown in figure 4.16 for the PHOJET (left) and PYTHIA (right) Monte Carlos. The plots of the first, second and third iteration are shown consecutively. The result of the triple Regge fits, both to the data and the Monte Carlo cross sections together with the weight factor, is represented for two different centre of mass energies $\langle W \rangle = 231$ and 91 GeV. The weights after the third iteration are very close to one.

The final mass distribution after the iterative reweighting procedure is shown in figures 4.15.d), e) and f) for the three centre of mass energy intervals. Both Monte Carlos describe the data reasonably well.

4.7.3 Additional control plots

It is important to verify that the reweighting procedure explained above also leads to a good agreement between the data and Monte Carlo, especially for these variables on which selection cuts are applied. Figures 4.17.a, b, c, d, e and f show the electron energy, $E - P_z$, Y_{had}, the total cluster energy in LAr, the total energy in SPACAL and the P_t of each central track for the SPACAL triggered sample at a centre of mass energy $\langle W \rangle = 231$ GeV. Most data are well described although the prediction for the total SPACAL energy is smaller than exhibited by the data.

4.7.4 Purities, stabilities, migrations and acceptances

After the rescaling of the invariant mass and the reweighting procedure, the Monte Carlos are used to study the migrations, efficiencies and purities. To define the purity, stability

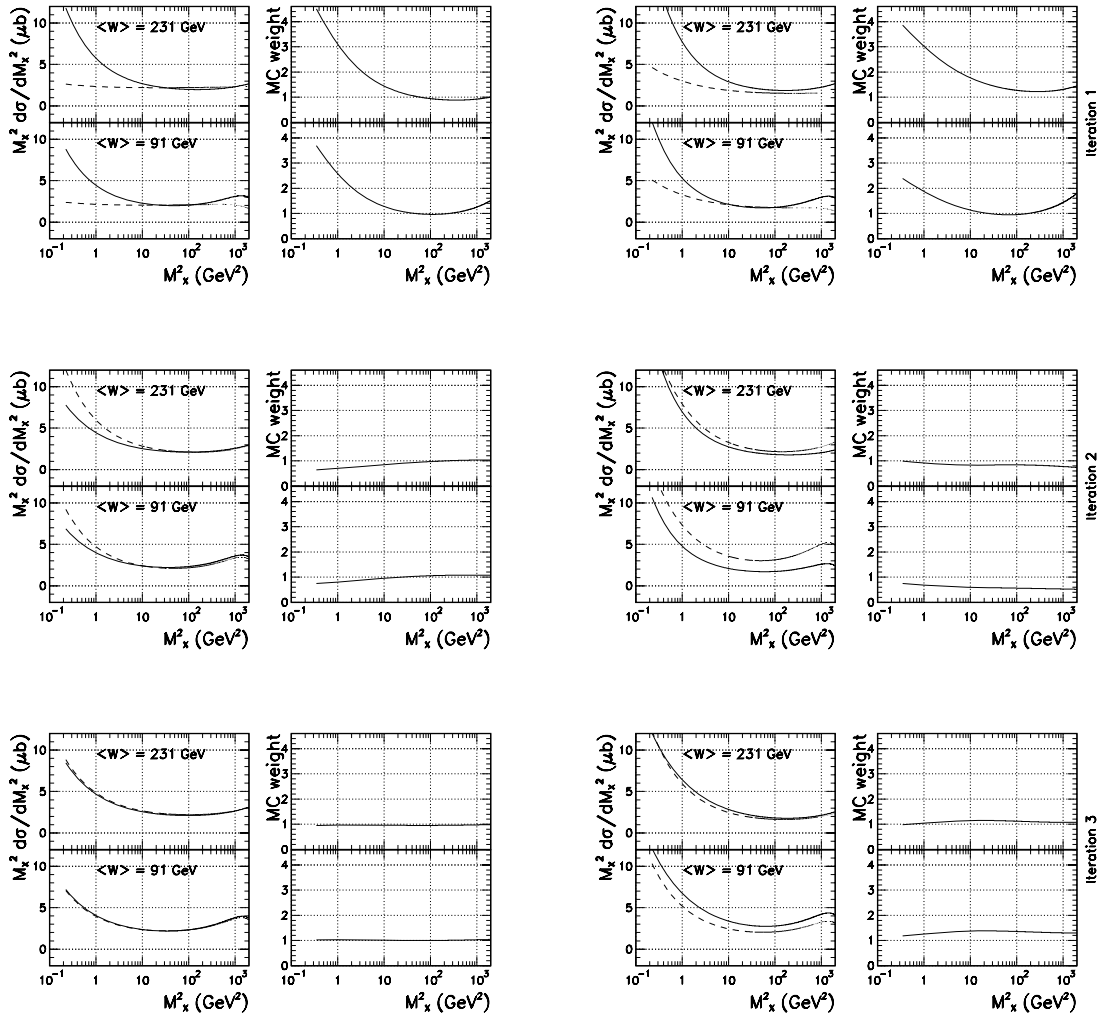

Figure 4.16: *For the three centre of mass energies the first, second and third iteration of the PHOJET reweighting procedure is shown from top to bottom on the left side. For both, data and Monte Carlo, the result of the triple Regge fit with the corresponding weight is represented. On the right side the same histograms are shown performed on the PYTHIA Monte Carlo.*

and migration, the following notations are introduced:

- $RecEvt_{ri/gi}(COND)$: number of events which after passing all cuts, are respectively reconstructed/generated in the invariant mass bin i with condition $COND$, $COND = 0$ means no condition.
- $GenEvt_{gi}(COND)$: number of events generated in the invariant mass bin i with condition $COND$ but with the additional constraint that at the generator level $M_Y < 1.6$ GeV and $\mid t \mid < 1$ GeV^2.

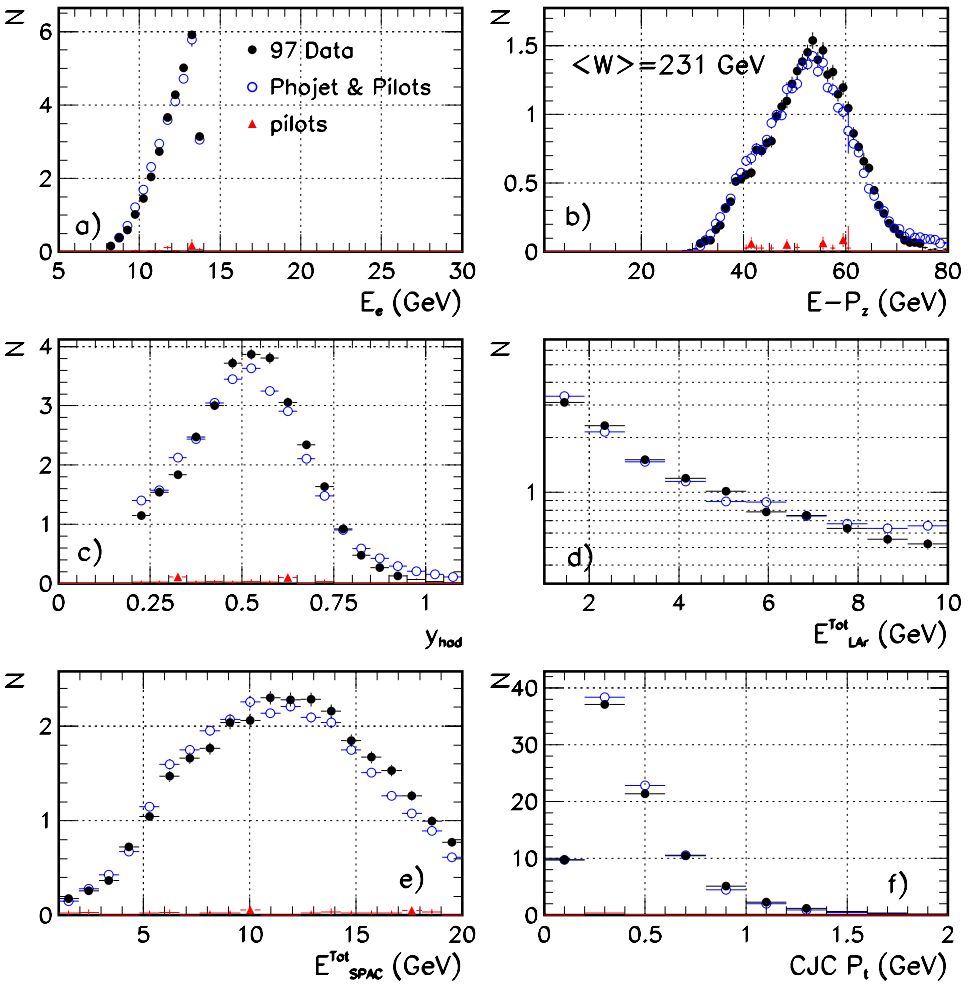

Figure 4.17: *Control distributions, like the scattered electron energy in a), the quantity $E - P_z$ in b), y_{had} in c), the total energy in the LAr calorimeter in d), the total energy in the SPACAL calorimeter in e) and the P_t of each track seen in the CJC in f), between PHOJET and SPACAL triggered data at a centre of mass energy of $\langle W \rangle = 231$ GeV.*

The bin purity can than be defined as:

$$\text{purity} = \frac{RecEvt_{ri}(M_X^{Rec} = M_X^{Gen})}{RecEvt_{ri}(0)} \tag{4.40}$$

being the fraction of events reconstructed in a bin that are also generated in that bin. The condition $(M_X^{Rec} = M_X^{Gen})$ means that the reconstructed mass M_X^{Rec} falls in the same bin

as the generated mass M_X^{Gen}. Similarly the bin stability can be defined as:

$$\text{stability} = \frac{RecEvt_{ri}(M_X^{Rec} = M_X^{Gen})}{RecEvt_{gi}(0)} \tag{4.41}$$

being the fraction of events generated in a bin that are also reconstructed in that bin.

Migrations can be subdivided into migrations into a bin and migrations out of a bin;

$$\text{Migration} \quad \text{IN} = \frac{RecEvt_{ri}(M_X^{gen} \neq M_X^{rec})}{RecEvt_{gi}(0)}, \tag{4.42}$$

$$\text{Migration} \quad \text{OUT} = \frac{RecEvt_{gi}(M_X^{rec} \neq M_X^{gen})}{RecEvt_{gi}(0)}. \tag{4.43}$$

These migrations IN/OUT can even be subdivided into migrations from bins at lower or at higher mass values where the condition $(M_X^{gen} \neq M_X^{rec})$ is replaced by $(M_X^{Gen} < M_X^{rec})$ and $(M_X^{Gen} > M_X^{rec})$.

As a consequence the acceptance, which takes only the cut into account and not the migrations, is defined as:

$$\text{Acc}^{\text{Cuts}} = \frac{RecEvt_{gi}(0)}{GenEvt_{gi}(0)} \tag{4.44}$$

and finally the total acceptance to correct the data with, taking into account the detector acceptance, analysis cuts and migration corrections, is defined as:

$$\text{Acc}^{\text{Total}} = \frac{RecEvt_{ri}(0)}{GenEvt_{gi}(0)}. \tag{4.45}$$

Hence the total acceptance can be parameterized as:

$$Acc^{Total} \quad = \quad Acc^{Cuts} \times (\text{Stability} + \text{Migration IN}) \tag{4.46}$$

The migrations are shown in figure 4.18 where the migrations IN and OUT are of the order of 50% except for the highest and lowest M_X^2-bin. Especially at very low M_X^{gen} values one noise cluster in the forward direction can give a relatively large contribution to the reconstructed value. Therefore the "migration IN" increases at very low M_X^{gen} values. The effect is especially seen at $\langle W \rangle = 91$ GeV since this centre of mass energy interval has a measurement at a lower M_X-bin compared to the measurement at $\langle W \rangle = 231$ and 187 GeV. The high mass generated events suffered from the fact that not all clusters were contained in the geometrical acceptance of the LAr calorimeter as can still be seen from the δ-distribution shown in figure 4.14.

The purities and stabilities are shown in figure 4.19. Due to the large migrations in the first and last M_X^2-bin for $\langle W \rangle$ =231 and 187 GeV the purity drops from about 60 % to 30%. For the centre of mass energy bin $\langle W \rangle = 91$ GeV the purity is over the whole M_X^2-range constant to 40 % as well as the stability apart from the lowest M_X^2-bin where it reaches a higher value of 60 %. All purities and stabilities shown in figure 4.19 are obtained with the PHOJET Monte Carlo. Similar results are obtained for the PYTHIA Monte Carlo.

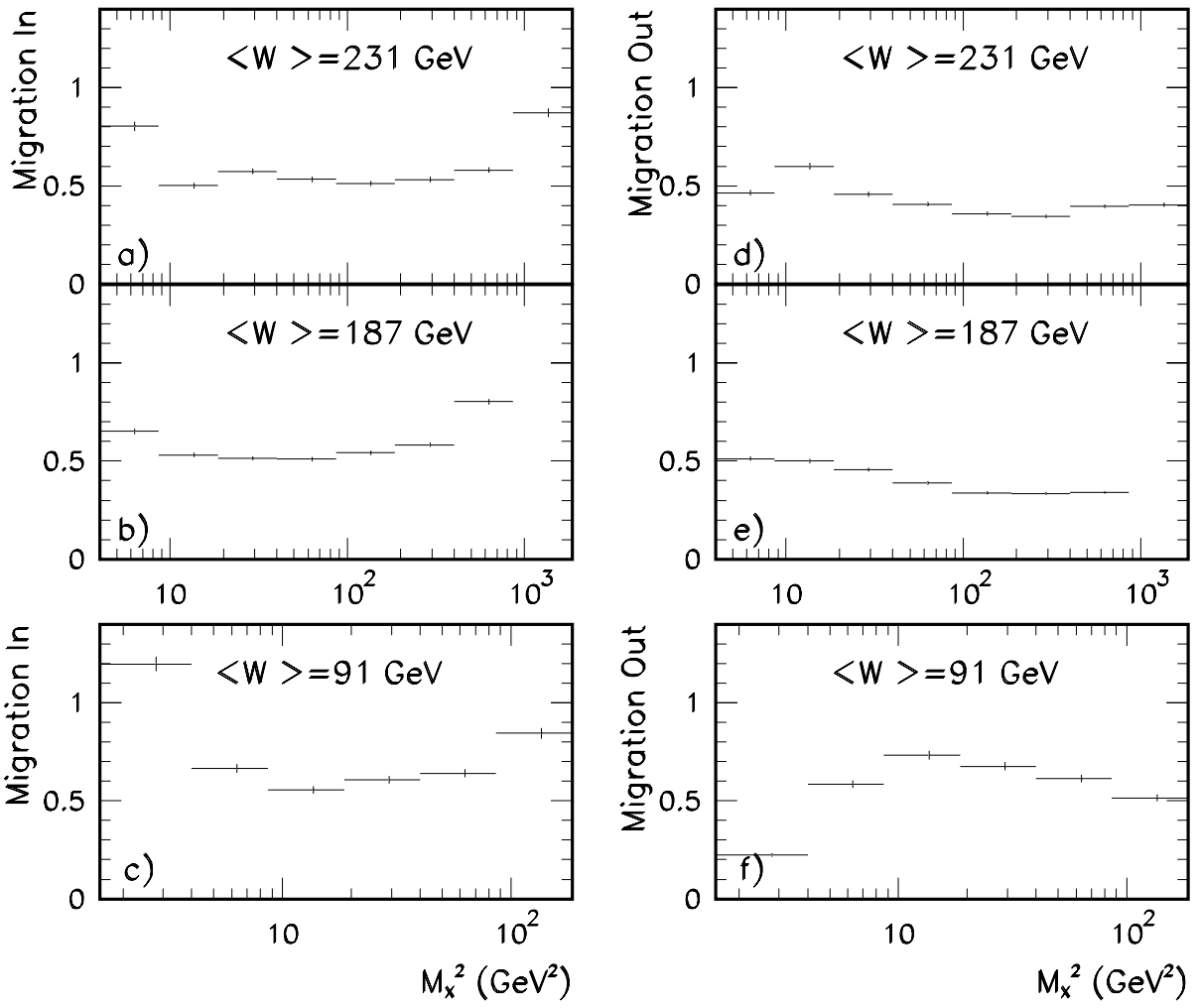

Figure 4.18: *The migrations IN (a-c) and migrations Out (d-f) are shown for the three centre of mass energies obtained with the PHOJET Monte Carlo. Similar results were obtained for the PYHTIA Monte Carlo.*

The result of the acceptance study is shown in figure 4.20. The acceptance effect of doing the analysis cuts is negligible at central values of M_X^2, while the acceptance decreases at high generated M_X^2-values due to the fact that those events will pass the forward detector cuts less frequently. Also at low generated invariant masses the acceptance will decrease since the gap finding at generator level can differ from that at reconstruction level.

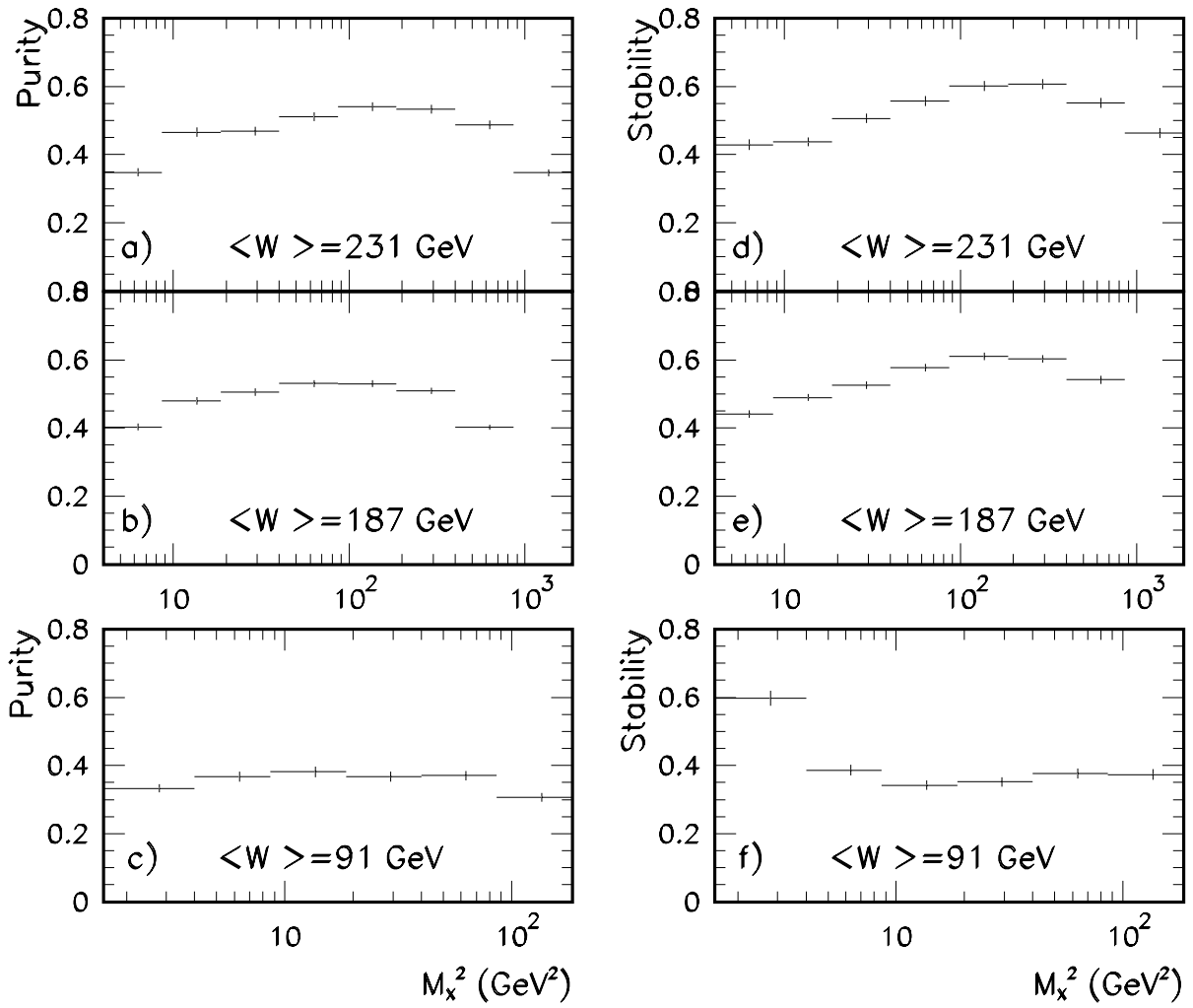

Figure 4.19: *The purities (a-c) and stabilities (d-f) are shown for the three centre of mass energies obtained with the PHOJET Monte Carlo. Similar results were obtained for the PYHTIA Monte Carlo.*

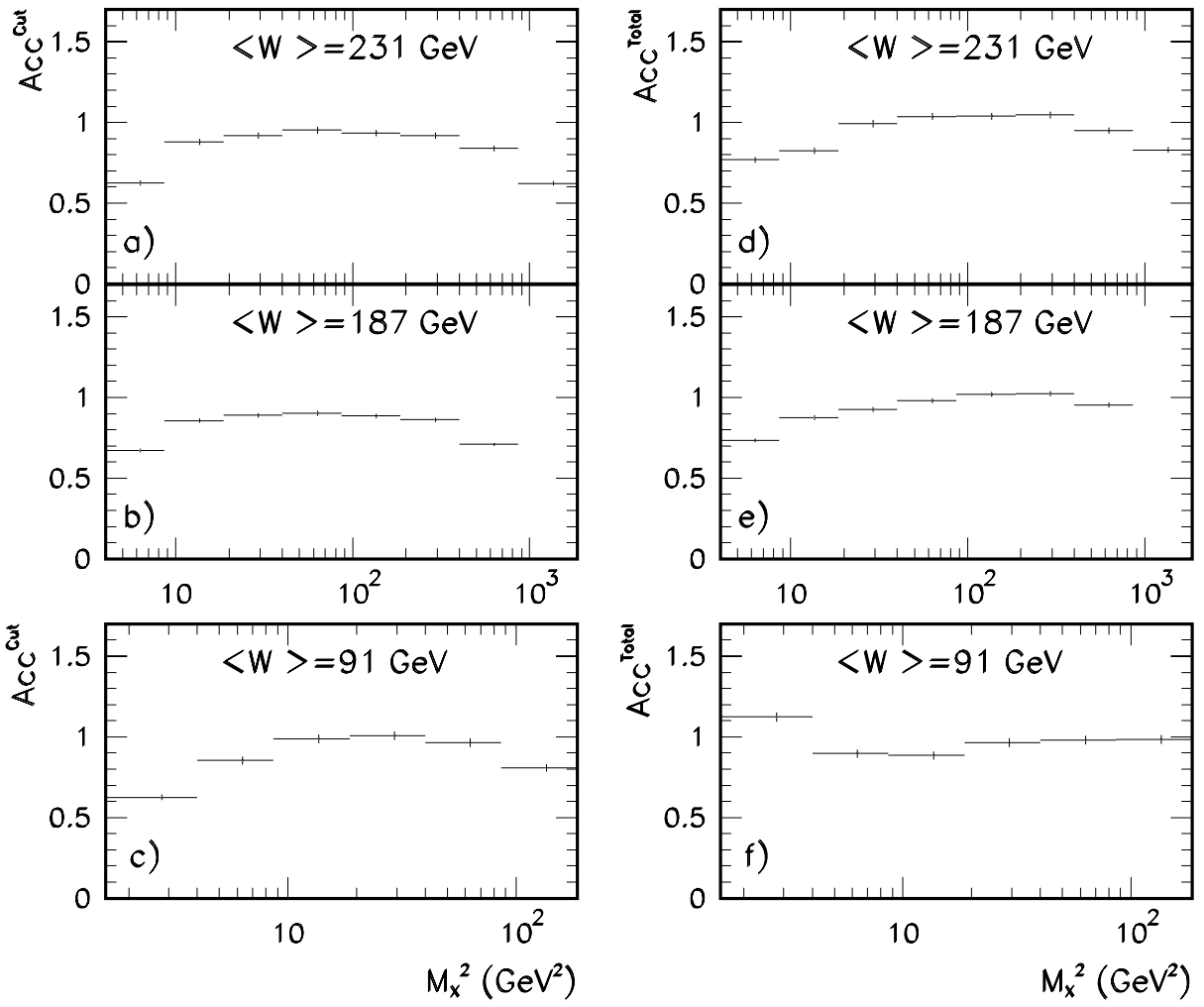

Figure 4.20: *The Acc^{Cuts} (a-c) and Acc^{Total} (d-f) are shown for the three centre of mass energies obtained with the PHOJET Monte Carlo. Similar results were obtained for the PYHTIA Monte Carlo.*

Chapter 5

The diffractive cross section

5.1 Extraction of differential cross section

The cross section that will be determined at three different centre of mass energies $\langle W \rangle =$ 231, 187 and 91 GeV will be extracted using the expression,

$$M_X^2 \left. \frac{d\sigma(ep \to eXY)}{dM_X^2} \right|_{M_Y<1.6 \text{ GeV}, \ |t|<1 \text{ GeV}^2} = M_X^2 \frac{(N - N_{backgr})}{\mathcal{L} \, \mathcal{A} \, \mathcal{T} \, \mathcal{W}} \tag{5.1}$$

where N, N_{backgr}, $\mathcal{A}$, $\mathcal{T}$ and $\mathcal{W}$ represent for every mass bin respectively the number of reweighted events (see section 4.5.2), the number of background events resulting from beam-gas interactions (see section 4.5.4), the calculated Monte Carlo acceptance (see section 5.1.2), the trigger efficiency (see section 5.1.3) and the M_X^2-bin width. $\mathcal{L}$ represents the integrated luminosity for the minimum bias 1997 event sample (see section 3.7.1) and amounts to 1.98 ± 0.03 pb^{-1}. It should be emphasized that the Monte Carlo acceptance calculation also includes the effect of smearing of events between bins due to the finite M_X mass resolution as well as the electron tagger acceptance. As explained in section 4.4, the cross section obtained through equation (5.1) very closely measures the differential cross section $M_X^2 \frac{d\sigma(ep \to eXp)}{dM_X^2}$ using a well defined experimental definition.

5.1.1 γp cross section and the photon flux factor $\mathcal{F}_{\gamma/e}$

As the coupling of the electron to the photon is perfectly known, the dynamics of the ep-interaction is contained in the γp-interaction. To convert the ep photoproduction cross section into a γp cross section the Weizsacker-Williams approximation is used [24, 25], following:

$$M_X^2 \frac{d\sigma(ep \to epX)}{dM_X^2} = \mathcal{F}_{\gamma/e} \times M_X^2 \frac{d\sigma(\gamma p \to epX)}{dM_X^2}, \tag{5.2}$$

where $\mathcal{F}_{\gamma/e}$ is the flux of quasi real photons and has to be estimated using:

$$f_{\gamma/e} = \frac{\alpha_{em}}{2\pi} \left[\frac{1 + (1-y)^2}{y} \ln \frac{Q^2_{max}}{Q^2_{min}} - 2m_e^2 \left(\frac{1}{Q^2_{min}} - \frac{1}{Q^2_{max}} \right) \right] \tag{5.3}$$

$\mathcal{F}_{\gamma/e}(\Delta\, y)$	y-range	$\langle W \rangle$
4.57×10^{-3}	0.5 - 0.7	231 GeV
9.03×10^{-3}	0.3 - 0.5	187 GeV
4.07×10^{-2}	0.05 - 0.2	91 GeV

Table 5.1: *Calculated values for the flux factors integrated over different y ranges corresponding to centre of mass energies $\langle W \rangle$ = 231, 187 and 91 GeV.*

with

$$Q^2_{min} = \frac{(m_e y)^2}{(1-y)}. \tag{5.4}$$

The analytically calculated values, integrated over the y-range for the considered W-bins, are represented in table 5.1, together with the corresponding y-range and the mean value of W.

5.1.2 The acceptance $\mathcal{A}$

The acceptance per bin entering equation (5.1) is a product of 2 acceptances: the acceptance of the electron tagger at 33 m or at 44 m and the detector acceptance. The detector acceptance is extensively discussed in section 4.7.4. The electron tagger acceptances are shown in figure 5.1 for the three centre of mass energies $\langle W \rangle$ = 231, 187 and 91 GeV and amount to respectively 30%, 40% and 35%. As expected, they are independent of M_X.

5.1.3 The trigger efficiency $\mathcal{T}$

To calculate the trigger efficiency one could rely on the Monte Carlo simulation. This implicitly assumes that the firing of the trigger elements is well described in the simulation. A different approach which avoids this Monte Carlo dependence is to calculate the trigger efficiency from the data by using an independent subtrigger, so called monitor triggers (MT). Since the trigger efficiency can be biased when determined with a background contaminated data sample[1], due to a different event topology with respect to the interested ep-interactions, the cuts to reject these backgrounds were applied on the reference sample, indicated in equation (5.5) by $Cuts$. This means that the SPACAL trigger efficiency can be calculated, using the z-vertex as the monitor trigger (MT_{zVtx}), following:

$$\mathcal{T}_{SPAC} = \frac{N(MT_{zVtx} + Cuts)|_{TE_{SPAC}}}{N(MT_{zVtx} + Cuts)} \tag{5.5}$$

where the denominator represents the number of selected events after applying all the cuts of table 4.4 and 4.5 and the numerator represents the same number of events for which also

[1]Even after the cuts, the data sample at $\langle W \rangle$=91 GeV was still highly contaminated with beam-gas background events.

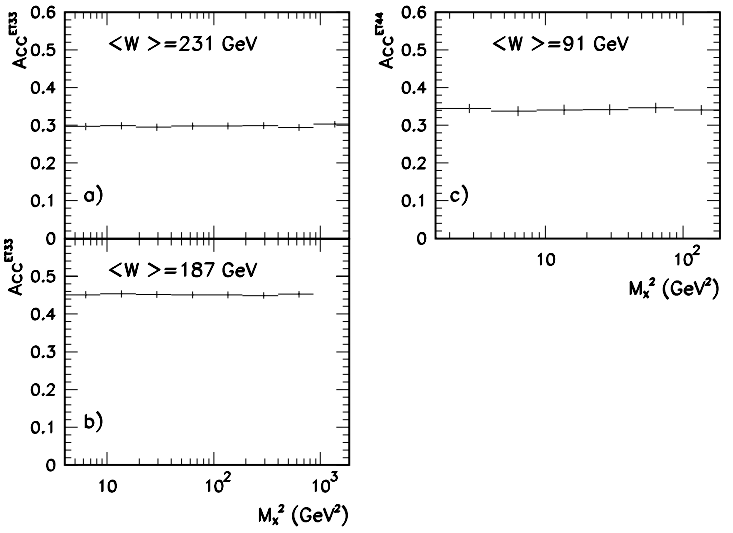

Figure 5.1: *Electron tagger acceptance as a function of M_X^2 for $\langle W \rangle$ = 231, 187 and 91 GeV.*

the SPACAL trigger fired. This SPACAL trigger efficiency was calculated as a function of the invariant mass M_X^2 and is shown in figure 5.2.a-b for the two highest centre of mass energies, labeled "data".

A cross check was made (also shown in figure 5.2.a-b) with the trigger efficiency obtained with both Monte Carlos, using a similar expression to (5.5) except that no monitor trigger is required, resulting in the same trigger efficiency. This indicates that the SPACAL trigger element is well described in the Monte Carlo. For the lowest centre of mass energy bin, $\langle W \rangle$=91 GeV, determining the trigger efficiency on the data sample will give an inadequate result since the beam-gas background events (25% of the total sample, see section 5.1.4) biases the trigger efficiency outcome. Therefore one has to rely on the trigger efficiency obtained from the Monte Carlos. Both Monte Carlos give a similar trigger efficiency (as can be seen in figure 5.2.c) so that the mean of the trigger efficiencies from PHOJET and PYTHIA is taken to correct the differential cross section with.

The trigger efficiency for finding a total energy in the SPACAL calorimeter above the trigger threshold, for the two highest centre of mass energies, is almost 100% in the whole range of M_X^2. While the efficiency decreases to about 50% for the centre of mass energy bin $\langle W \rangle$= 91 GeV. This comes from the fact that the X-system for this lower centre of mass energy was produced more centrally in the detector leaving less total energy in the backward region.

Similarly, the z-vertex trigger efficiency for the two highest centre of mass energies, $\langle W \rangle$=231 and 187 GeV, was determined on the data samples with the SPACAL trigger serving as the monitor trigger. For the lowest centre of mass energy, $\langle W \rangle$=91 GeV, the

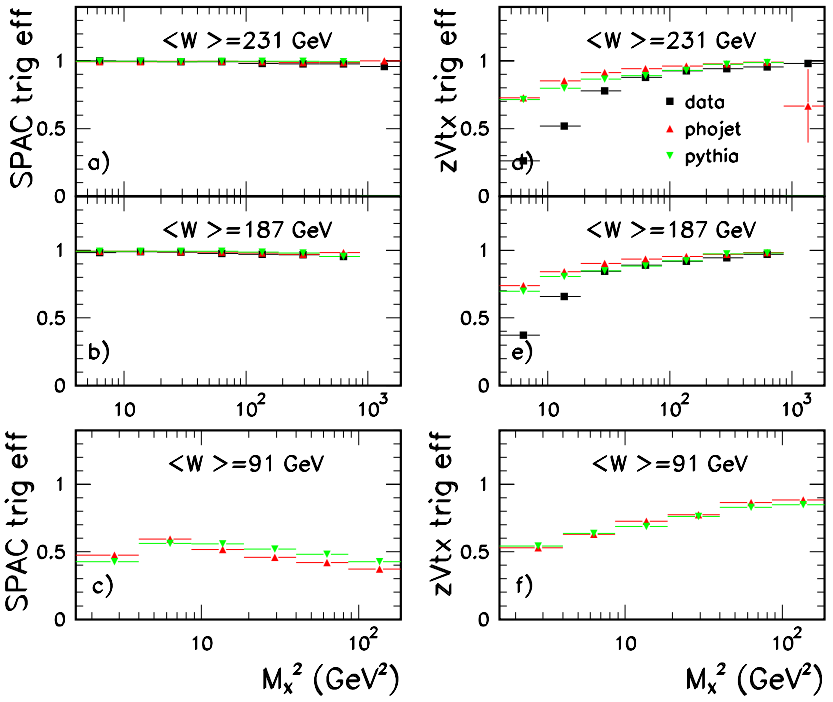

Figure 5.2: *The SPACAL (figures a-c) and z-vertex (figures d-f) trigger efficiency shown for the three centre of mass energies $\langle W \rangle$ = 231, 187 and 91 GeV. The squares represent the trigger efficiency determined on the data. The triangles represent the trigger efficiency determined on the Monte Carlos.*

Monte Carlos are used for the same reason as is given in the discussion of the SPACAL trigger efficiency. The result is shown in figure 5.2.d-f for the three centre of mass energies.

The acceptance of the z-vertex trigger is particularly sensitive to the extent of the fragmentation region of the photon. At relatively large M_X, tracks are produced in the central region of the laboratory system (see equation (4.25), and the z-vertex trigger is efficient. In this region the trigger efficiency for the two highest centre of mass energies obtained with PHOJET and PYTHIA or with the data is very similar[2]. At small values of M_X, corresponding to low multiplicities in the central tracker region, low efficiencies are observed. In this region the z-vertex efficiency from both Monte Carlos is not in good agreement with the trigger efficiency obtained with the data. Therefore the z-vertex trigger can only be used for the study of diffractive processes yielding final states at relatively large M_X and was originally meant as a cross check sample with respect to the SPACAL triggered sample. For the lowest centre of mass energy, the z-vertex trigger efficiency is determined from the Monte Carlos, since the data contain still a large fraction of beam-gas background events after the cuts from table 4.4 and 4.5. As in the case of the SPACAL trigger efficiency

[2]As in the case of the SPACAL trigger efficiency, the z-vertex trigger efficiency obtained with the Monte Carlo is based on expression (5.5) where no monitor trigger is required.

both Monte Carlos show a similar result, such that the mean of both Monte Carlos is taken as the trigger efficiency with which the cross section will be corrected.

5.1.4 The background N_{backgr}

The numbers of beam-gas background events, already mentioned in an integrated M_X^2 way in section 4.5.4, have to be known as a function of M_X^2 in order to subtract them statistically from the number of measured events. This has to be done for the three centre of mass energy bins for both the SPACAL triggered sample as well as for the z-vertex triggered sample. The result for the SPACAL triggered sample is shown in figure 5.3 where the background contribution[3] is normalized to the number of measured events.

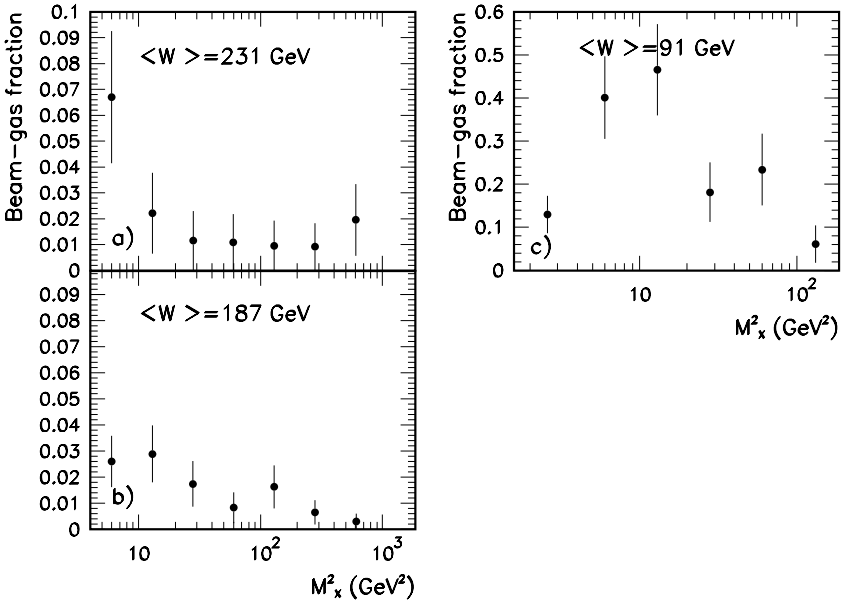

Figure 5.3: *Beam-gas background fraction with respect to the number of selected data events in function of* M_X^2.

The determination of the number of beam-gas background events in bins of M_X^2 for the z-vertex sample was not possible. Due to the high prescale factors for the z-vertex etag44 trigger, i.e. for some runs the prescale factor was set to 10000, and the very low statistics sample of pilot data, i.e. sometimes less than 2 or 3 events, the uncertainty of the subtraction is huge. This can be seen from the z-vertex distribution shown in figure 5.4. Here the number of events normalized to the luminosity is shown as a function of the

[3]The beam-gas background contribution itself is absolutely normalized as explained in section 4.5.4 using the y_{had}-distribution.

position in z of the primary vertex. The data are compared with the PHOJET Monte Carlo to which the beam-gas background was added. One sees from the figure that the statistical uncertainty coming from the beam-gas events is huge and no adequate beam-gas subtraction will be possible for the z-vertex sample. Therefore we decided not to use the z-vertex trigger to define the differential cross section. In any case, with the SPACAL triggered sample the differential cross section could be measured in an even larger domain of the photon mass M_X^2.

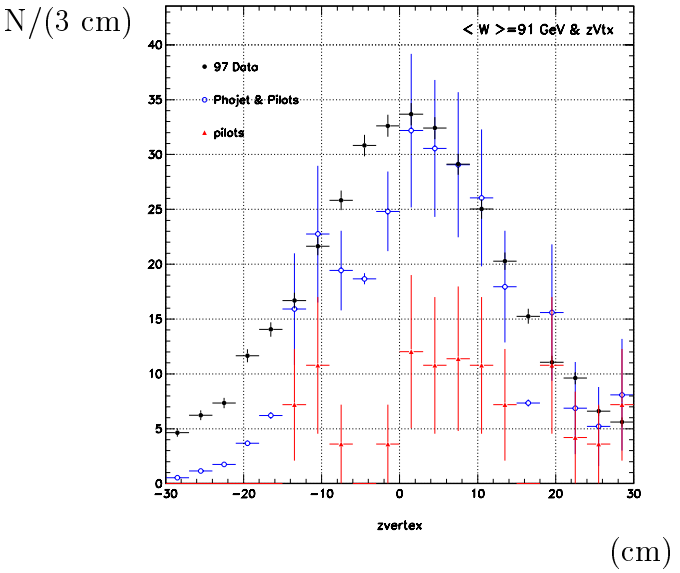

Figure 5.4: *The z-vertex distribution for the z-vertex trigger at a centre of mass energy of* $\langle W \rangle = 91$ *GeV, shown for the data, PHOJET with the beam-gas contribution added to it and the beam-gas events only.*

5.2 Systematic errors

The measurement of cross sections is always subjected to systematic uncertainties. Below follows the list of uncertainties considered. Two groups of uncertainties can be distinguished, i.e. the uncertainties varying from bin to bin and global uncertainties. In these two groups the uncertainties associated with the detector simulation will be mentioned first followed by the uncertainties coming from the Monte Carlo modeling.

Calibration of hadronic energies

The uncertainty in the hadronic calibrations of the LAr and SPACAL calorimeters are 4% [95] and 7% [96], respectively. To take these uncertainties into account the energy of all clusters in the LAr and SPACAL are once rescaled by respectively $\pm 4\%$ and $\pm 7\%$. The M_X-dependent uncertainty on the cross section can be seen in figure 5.6.a. The effect is especially seen at large centre of mass energies and at the lowest M_X since

there the multiplicity forming the dissociative mass is very small and the relative effect on the dissociative mass is visible. The resulting uncertainties in the cross sections reach the 10% level with a mean value of 5% for the LAr and SPACAL together.

PRT efficiency

The efficiency of the PRT in the Monte Carlo was degraded using the scintillator efficiencies explained in section 4.6. As those efficiencies are known only approximately, an uncertainty of ±30% was attributed to them, resulting in a PRT efficiency varying between 50% and 100%. The effect on the differential cross section is shown in figure 5.6.b as a function of M_X^2. At the highest M_X when the dissociative system is populating the forward part of the detector, the acceptance will be sensitive to the assumed PRT efficiency since the forward detectors are required to be empty.

Model dependence

The different generator models as used in the PHOJET and PYTHIA Monte Carlo result in differences in the calculated acceptances as was shown in section 4.7.4. To account for these model dependences, a systematic error has been introduced equal to the difference between PHOJET and PYTHIA Monte Carlo acceptances and the nominal acceptance, being the weighted average of the acceptances of the two Monte Carlos in a ratio 70/30 as explained in section 4.7.2. The variation with M_X^2 is shown in figure 5.7.a for the three centre of mass energy bins. The 70/30 weight explains the larger deviation of the PYTHIA Monte Carlo with the nominal value.

Assumptions on dissociation mass spectra

Both Monte Carlo models, PHOJET and PYTHIA, assume a distribution in M_X and M_Y beyond resonance regions of the form $d\sigma/dM^2 \propto 1/M^2$. All processes in the Monte Carlos, i.e. EL, GD, PD, DD and ND, are reweighted by $(1/M_X^2)^{\pm 0.15}$ and $(1/M_Y^2)^{\pm 0.30}$. The effect of this reweighting on the differential cross section is shown in respectively figure 5.8.a and b.

Beam-gas background uncertainty

The threshold energy for the LAr clusters was varied by 25 % and the resulting systematic errors to the cross section measurement are shown in figure 5.7.b.

Forward Muon uncertainty

An 8 % normalization uncertainty is attributed to the cross section due to the uncertainty on the forward muon detector by varying the forward muon efficiency by ±5% and due to the cut on $M_Y < 1.6$ GeV causing migrations or smearing of events across this boundary.

Acceptance of the electron taggers

A 3 (5)% systematic error is assumed on the acceptance of the 33m (44m) electron tagger, averaged over the different periods of beam-optics, and the measured range in y.

Luminosity

The uncertainties in the determination of the ep luminosity affect the total normalization by 1.5 %.

5.3 Measured differential cross section $M_X^2\ d\sigma_{\gamma p\to XY}/dM_X^2$

Figure 5.5.a-c shows $M_X^2\ d\sigma_{\gamma p\to XY}/dM_X^2$ at three centre of mass energy bins, $\langle W\rangle$ = 231 GeV, 187 and 91 GeV, measured in bins of M_X^2 in the range $1.58 < M_X^2 < 1860$ GeV^2 with $M_Y < 1.6$ GeV and $\mid t \mid < 1$ GeV^2. The exact values of the differential cross section measurement as well as the statistical and systematical errors can be found in table 5.2. The statistical error mentioned is composed by the number of selected events and the number of subtracted beam-gas events weighted with their corresponding prescale factors. From this table one sees that the statistical error on the measurement at the centre of mass energy of $\langle W\rangle$=187 GeV is smaller than those at $\langle W\rangle$=231 GeV, which results from the fact that the electron tagger acceptance is bigger at $\langle W\rangle$ = 187 GeV with respect to $\langle W\rangle$ = 231 GeV leading to a higher statistics sample. The larger statistical errors at $\langle W\rangle$=91 GeV are due to the large prescale factors in the etag 44 m triggered sample. At the centre of mass energy bins $\langle W\rangle$ =231 and 187 GeV, the systematical error is the dominant one with respect to the statistical error, while at $\langle W\rangle$ = 91 GeV they are of the same size.

At sufficiently large M_X^2 the measurement in all three W-ranges displays an approximate $d\sigma/dM_X^2 \propto 1/M_X^2$-dependence. The differential cross section $d\sigma/dM_X^2$ was therefore multiplied by M_X^2 to see the deviation from this dependence. This more complex structure of the differential cross section will be investigated within the triple Regge model (see Chapter 6).

$\langle W \rangle = 231$ GeV				
M_X^2 (GeV^2)	Bin Limits (GeV^2)	$M_X^2\, d\sigma/dM_X^2$ (μb)	Stat.	Syst.
5.97	4.00-8.62	2.922	± 0.133	$^{+0.393}_{-0.423}$
12.9	8.62-18.6	2.390	± 0.101	$^{+0.336}_{-0.292}$
28.1	18.6-40.0	2.061	± 0.084	$^{+0.267}_{-0.191}$
59.9	40.0-86.2	2.022	± 0.082	$^{+0.251}_{-0.305}$
129	86.2-186	2.299	± 0.088	$^{+0.222}_{-0.502}$
280	186-400	2.422	± 0.090	$^{+0.255}_{-0.551}$
606	400-862	3.141	± 0.117	$^{+0.395}_{-0.640}$
1313	862-1860	3.454	± 0.213	$^{+0.557}_{-0.586}$
$\langle W \rangle = 187$ GeV				
M_X^2 (GeV^2)	Bin Limits (GeV^2)	$M_X^2\, d\sigma/dM_X^2$ (μb)	Stat.	Syst.
5.98	4.00-8.62	2.751	± 0.072	$^{+0.446}_{-0.334}$
13.0	8.62-18.6	2.091	± 0.059	$^{+0.307}_{-0.209}$
27.9	18.6-40.0	1.912	± 0.053	$^{+0.240}_{-0.195}$
60.1	40.0-86.2	1.870	± 0.049	$^{+0.204}_{-0.317}$
129	86.2-186	1.950	± 0.051	$^{+0.201}_{-0.418}$
280	186-400	2.384	± 0.056	$^{+0.285}_{-0.513}$
607	400-862	2.922	± 0.067	$^{+0.381}_{-0.437}$
$\langle W \rangle = 91$ GeV				
M_X^2 (GeV^2)	Bin Limits (GeV^2)	$M_X^2\, d\sigma/dM_X^2$ (μb)	Stat.	Syst.
2.58	1.58-4.00	2.589	± 0.304	$^{+0.495}_{-0.243}$
6.00	4.00-8.62	1.713	± 0.337	$^{+0.262}_{-0.213}$
12.9	8.62-18.6	1.853	± 0.426	$^{+0.242}_{-0.218}$
27.9	18.6-40.0	2.480	± 0.346	$^{+0.230}_{-0.401}$
60.2	40.0-86.2	2.206	± 0.347	$^{+0.222}_{-0.456}$
131	86.2-186	2.712	± 0.325	$^{+0.318}_{-0.671}$

Table 5.2: *The measured differential cross section $M_X^2\, d\sigma_{\gamma p \to XY}/dM_X^2$ in the range $M_Y < 1.6$ GeV and $\mid t \mid < 1$ GeV^2. All measurements quoted are bin center corrected in $log(M_X^2)$.*

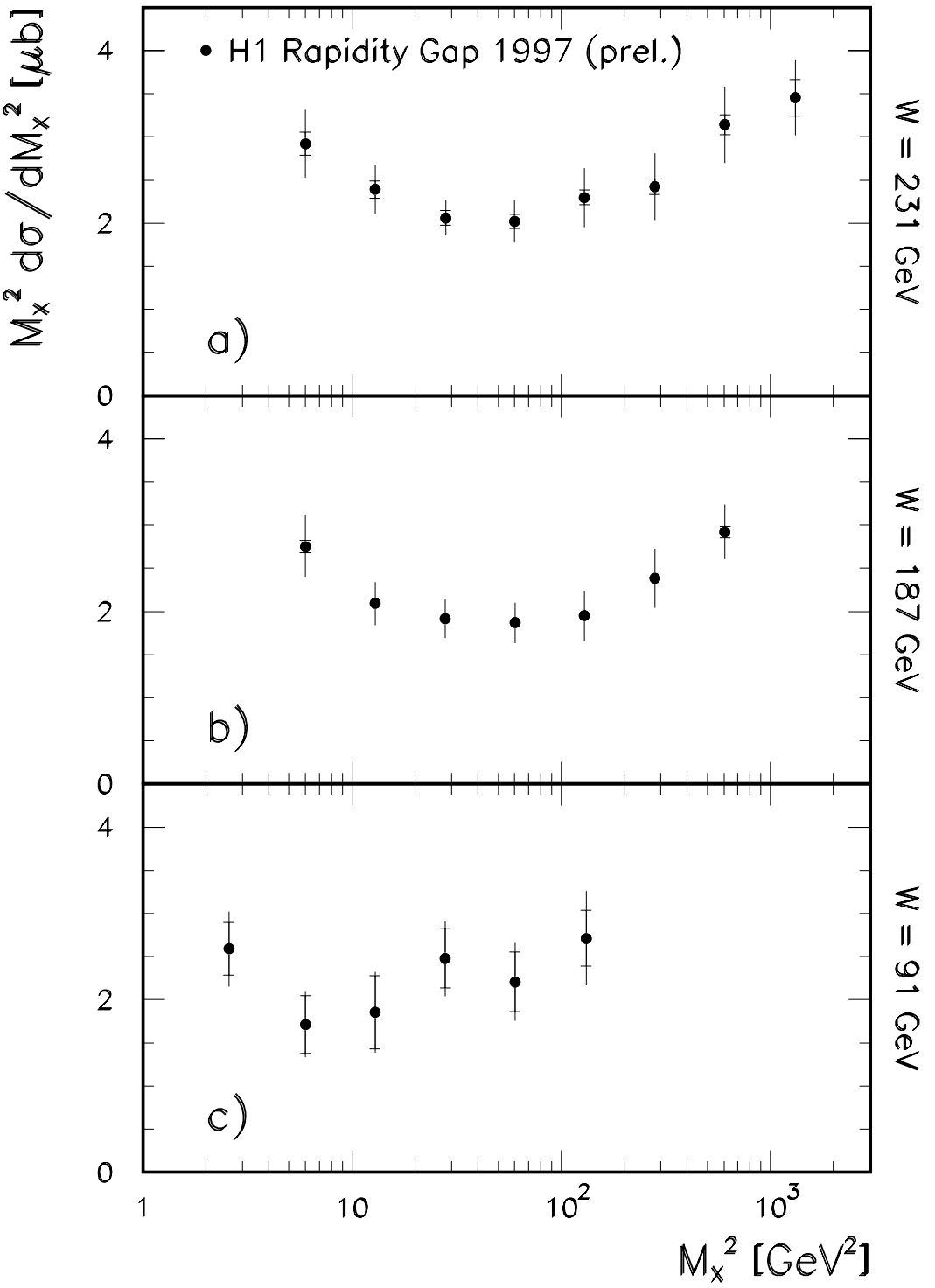

Figure 5.5: *The present measurement of the quantity $M_X^2\ d\sigma_{\gamma p \to XY}/dM_X^2$ with $M_Y < 1.6$ GeV and $\mid t \mid < 1$ GeV^2 for the three centre of mass energies. The inner error bars are statistical and the outer error bars show statistical and systematic errors added in quadrature.*

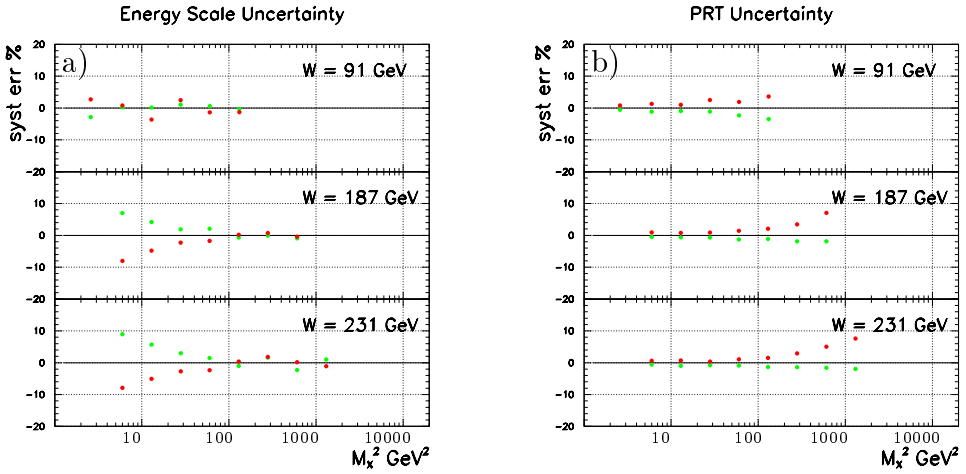

Figure 5.6: *Percentage systematic error on the differential cross section measurement for the three centre of mass energies $\langle W \rangle$=91, 187 and 231 GeV as a function of M_X^2 due to a) the energy calibration errors in LAr and SPACAL of respectively +4% and +7% (light grey) and -4% and -7% (red) and b) PRT efficiency of 100% (green) and 40% (red).*

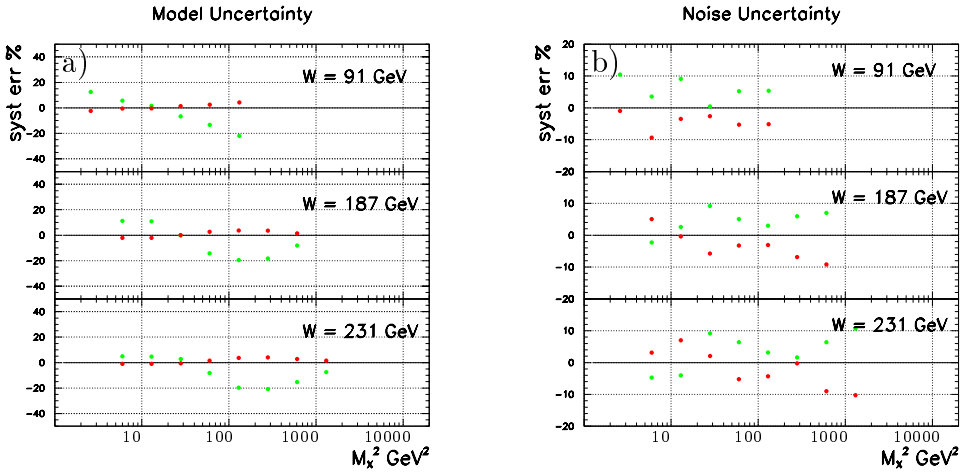

Figure 5.7: *Percentage systematic error on the differential cross section measurement for the three centre of mass energies $\langle W \rangle$=91, 187 and 231 GeV as a function of M_X^2 due to a) the model uncertainty defined as the difference between the nominal Monte Carlo (i.e. mixture of 70% PHOJET and 30% PYTHIA) and PHOJET (red) and the nominal Monte Carlo and PYTHIA (green) and b) the uncertainty on the noise. The noise threshold value is varied by -25% (green) and +25% (red).*

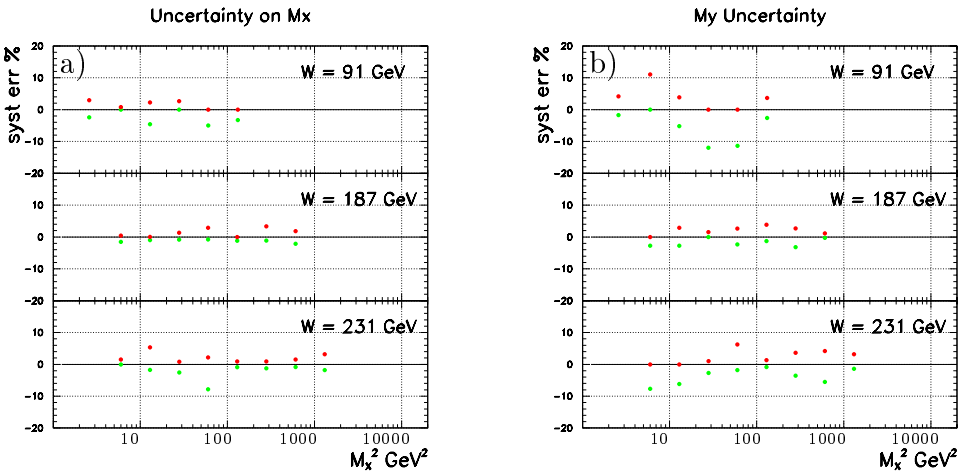

Figure 5.8: *Percentage systematic error on the differential cross section measurement for the three centre of mass energies $\langle W \rangle$=91, 187 and 231 GeV as a function of M_X^2 due to a) the uncertainty on the assumed M_X^2-distribution and b) the uncertainty on the assumed M_Y^2 distribution. Green represent the effect on the cross section if the mass distribution was reweighted by $(1/M)^{+\alpha}$ and red by $(1/M)^{-\alpha}$.*

Chapter 6

Triple Regge analysis

In this chapter the diffractive dissociation cross section will be subjected to a triple Regge analysis. First an effective intercept will be determined from the rapidity gap data (RG) only (see chapter 5), afterwards a more complete triple Regge fit will be performed on a combined dataset, i.e. rapidity gap data (RG), leading proton data (called FPS for H1 and LPS for ZEUS) and fixed target data (FT). At the end the extracted γp triple Regge couplings will be compared to those extracted from pp-data. Finally both set of triple Regge couplings will be used in a first attempt to describe $F_2^{D(3)}$, F_2^{LP} and F_2^{LN} in deep inelastic scattering within the framework of the triple Regge model, originally meant to describe soft processes.

6.1 Determination of an effective intercept $\alpha_{eff}(0)$

Since the triple Regge fit is a many parameter fit in which the relative importance of the contributing terms is rather complicated (see section 6.2), a more simplified Regge based fit has been performed first. In the normal Regge limit, applicable in the range where $s/M_X^2 \to \infty$ and M_X^2 is fixed, the inclusive cross section can be written as:

$$\frac{d\sigma}{dt\, dM_X^2} \propto \frac{1}{s^2} \sum_{i,j} \beta_{AC}^i(t)\beta_{AC}^j(t) \left(\frac{s}{M_X^2}\right)^{2\alpha_i(t)} \text{Im}\, A_{(iB\to jB)}(\nu, t). \tag{6.1}$$

Instead of taking into account all possible contributing Regge trajectories, we make the simplified assumption that they can be replaced by a single so called *effective* trajectory with an effective intercept $\alpha_{eff}(0)$. Expressing the reggeon couplings with the external particles as $\beta_{AC}^i(t) = \beta_{AC}^i(0)\exp(b_{Ai}t)$, the differential cross section in HERA variables[1] can than be written as:

$$\frac{d\sigma}{dt\, dM_X^2} \propto \left(\frac{W^2}{M_X^2}\right)^{2\alpha_{eff}(0)-2} . \exp(B\, t), \tag{6.2}$$

[1]This means that the centre of mass energy between particle A and B, s_{AB}, is replaced by the photon-proton centre of mass energy W^2.

where all the t-dependences have regrouped in the B-exponential as,

$$B = b_0 + 2\alpha' \ln(W^2/M_X^2). \tag{6.3}$$

In order to compare the predictions of formula (6.2) to the data, a further integration of t is required, as in the rapidity gap data the scattered proton is not tagged and covers a t-range of $t \in [-1, t_{min}]$. Hence the final expression at fixed M_X^2 reads as,

$$\frac{d\sigma}{dM_X^2} \propto \left(W^2\right)^{2\alpha_{eff}(0)-2} \frac{e^{Bt_{min}} - e^{-B}}{B}. \tag{6.4}$$

The values for the constants $b_0 = 4.6 \pm 0.6$ GeV $^{-2}$ and $\alpha' = 0.26 \pm 0.02$ GeV $^{-2}$ are taken from [44]. From a fit of (6.4) to the cross section data for every M_X^2-bin as a function of W, a value $\alpha_{eff}(0)$ as a function of M_X^2 can be extracted. These fits are shown in figure 6.1. Unfortunately for the highest M_X^2-bin only two W-measurements are available reducing the fit to a calculation. In the fit only the statistical errors have been used. The quadratic sum of the statistical and systematical error is represented by the full error bar on figure 6.1.

Figure 6.2 shows the extracted $\alpha_{eff}(0)$ values (black points) as a function of M_X^2 in the range $5.92 < M_X^2 < 281$ GeV^2. The total systematical error shown is the systematical error from the cross section measurement listed in section 5.2 to which the uncertainty from the parameter uncertainties b_0 and α' is added quadratically. In figure 6.2, as a reference to the measured values of α_{eff}, a line and error band are also drawn, which correspond to the value of $\alpha_{I\!P}(0)$ and corresponding error as obtained from a triple Regge fit (see section 6.2). As can be seen the $\alpha_{eff}(0)$ measurements are compatible with an intercept of the pomeron, leaving hardly any room for contributions from secondary reggeon exchanges. This is in contrast with the $\alpha_{eff}(0)$ extracted from the leading proton data as explained in section 2.6.2, which is obtained at much higher values for M_X^2, as shown in figure 6.2. The measured value of $\alpha_{eff}^{FPS}(0) = 0.33 \pm 0.04$ (stat) ± 0.04 (syst), as given by equation (2.77), between the reggeon intercept of $\alpha_{I\!R}(0) = 0.5$ and the pion intercept of $\alpha_\pi(0) = 0$.

6.2 Fits in the triple Regge limit

A triple Regge analysis using only the rapidity gap (RG) data is not possible. Indeed the 18 measurements from six M_X^2-bins and three W-bins are too few in order to determine the various parameters appearing in the triple Regge expansion [38]. Therefore we have enlarged the M_X^2- and W-range by extending the rapidity gap data set with:

- low W fixed target (FT) data $\langle W \rangle = 12.9$ and 15.3 GeV, from Chapin et al. [74].
- leading proton data (called FPS for H1 and LPS for ZEUS) extending the M_X^2-range to larger values $M_X^2 \in [900, 18000]$ GeV^2.

In section 6.2.1 the various aspects in using FT data, RG data and FPS data will be discussed. Unfortunately the FPS and LPS data are presently not consistent and hence the inclusion of FPS data and LPS data lead to different results. The difference in the result caused by the differences in the leading proton cross section measurement (see figure 2.19), will be discussed in section 6.2.2

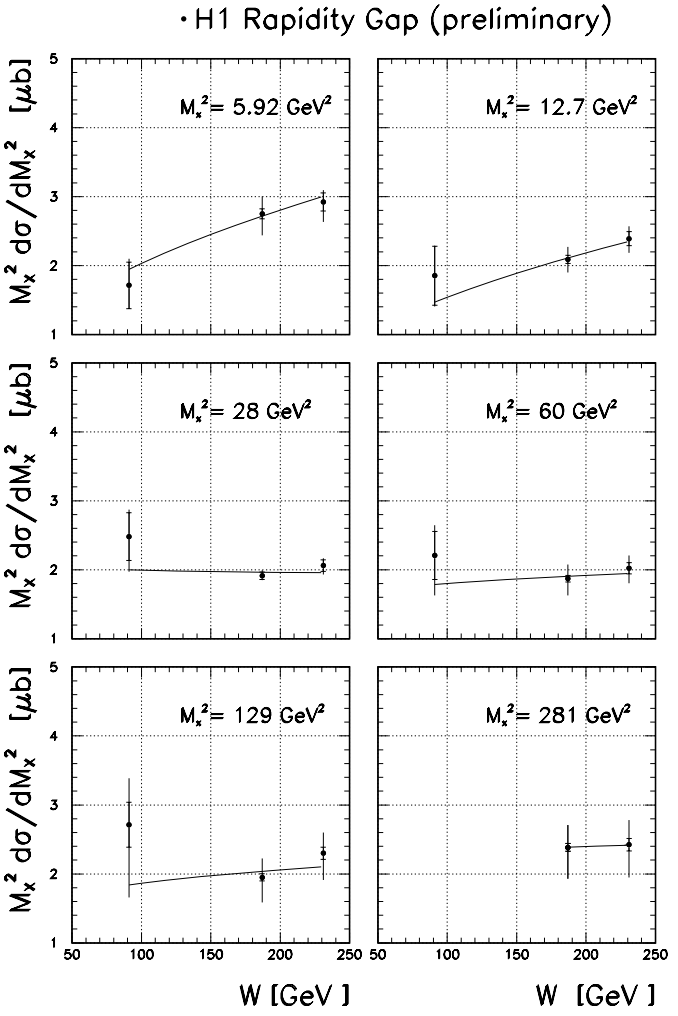

Figure 6.1: *The measured differential cross section $M_X^2 d\sigma/dM_X^2$ is shown in function of the photon-proton centre of mass energy $\langle W \rangle$ for six values of M_X^2. A fit corresponding equation (6.4) is performed to extract for each M_X^2-bin a value $\alpha_{eff}(0)$.*

6.2.1 Triple Regge fit (H1)

In the previous section a fit on the RG data was performed in the normal Regge limit ($W^2 \gg t$ and M_X^2 fixed), extracting an effective intercept by looking at the W-dependence only. Here a more complete fit is performed in the triple Regge limit ($W^2 \gg M_X^2 \gg \mid t \mid$), extracting the triple Regge couplings and the pomeron intercept, taking into account both the W- and the M_X^2-dependence using,

$$W^2 \frac{d^2\sigma}{dtdM_X^2} = \frac{d^2\sigma}{dtdz} = \frac{s_0}{W^2} \sum_{i,k} G_{iik}(0) \left(\frac{W^2}{M_X^2}\right)^{2\alpha_i(0)} \left(\frac{M_X^2}{s_0}\right)^{\alpha_k(0)} exp(Bt), \qquad (6.5)$$

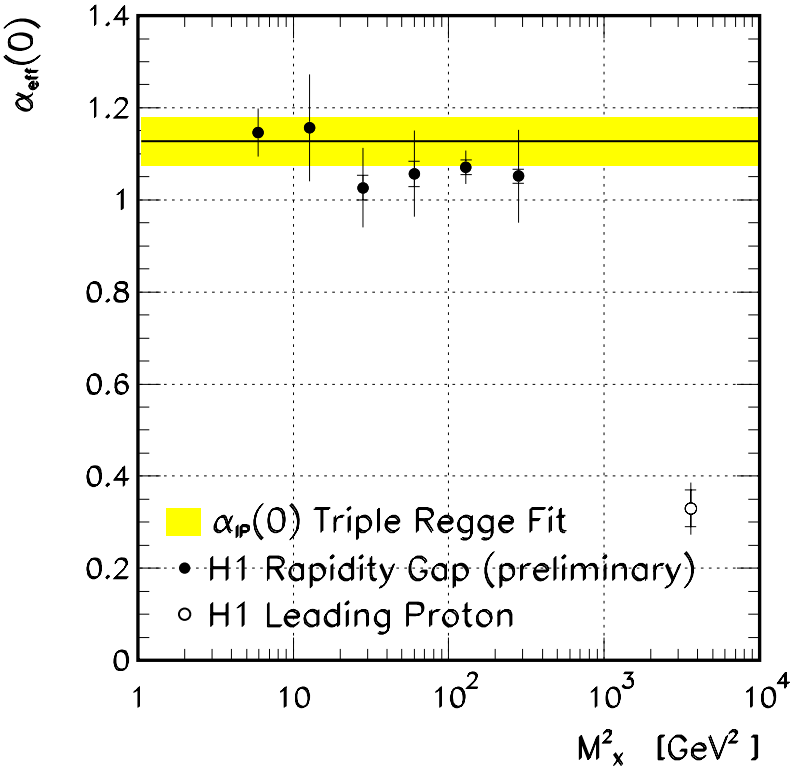

Figure 6.2: *The effective intercept as extracted from a fit in the normal Regge limit as a function of M_X^2 is shown by the black points. The open point represents an effective intercept obtained from the Forward Proton Spectrometer data. The inner error bar represents the statistical error, while the outer error bar represents the quadratic sum of the statistical and systematical error. The band shows the value for the pomeron intercept and its uncertainty obtained from a triple Regge fit (see section 6.2).*

where the t-dependence is absorbed in the exponential with,

$$B \equiv B(M_X^2, W^2) = 2b_{pi} + b_{iik} + 2\alpha_i^{'} \ln\left(\frac{W^2}{M_X^2}\right). \tag{6.6}$$

Equation (6.5) reduces to equation (2.71) under the assumption that the reggeon-proton and the three-reggeon couplings are parameterized as mentioned in equation (2.72)-(2.74). The remaining parameters from equation (6.5) are fixed to previously measured values represented in table 2.3.

t-dependence

The three cross section measurements (RG, FPS and FT) are all measured in different kinematical ranges. For the RG data the cross section is measured up to $\mid t \mid = 1$ GeV^2, for the FPS data up to $\mid t \mid = 0.04$ GeV^2, while for the FT data the cross section is measured at a fixed value of t, i.e. $\mid t \mid = 0.05$ GeV^2. Therefore, the triple Regge formula used in the fit to the RG and FPS data is integrated over the kinematically allowed range in t following:

$$M_X^2 \frac{d\sigma}{dM_X^2} = N \sum_{i,k} G_{iik}(0) \left(W^2\right)^{2\alpha_i(0)-2} \left(M_X^2\right)^{\alpha_k(0)-2\alpha_i(0)+1} \int_{t_{max}}^{t_{min}} \exp(Bt) dt, \tag{6.7}$$

with a normalization factor, N, defined as,

$$N = \frac{\int_0^{t_{max}^{exp}} e^{-b\,|t|}\, d\,|t|}{\int_0^{t_{max}} e^{-b\,|t|}\, d\,|t|}, \tag{6.8}$$

representing the fraction of the cross section which was seen in the respective analysis due to the limited acceptance in t. For the RG data this factor corresponds to 0.999 while for the FPS data, in which $\mid t \mid < 0.04$ GeV^2 instead of 1 GeV^2, the factor N is of the order of 0.24.

The integration limits t_{min} and t_{max} of equation (6.7), correspond to the minimal and maximal kinematically accessible value, being

$$t_{max/min} = \left(\frac{M_X^2}{2W}\right)^2 - \left(\left(\frac{W^2 - m_p^2}{2W}\right) + / - \sqrt{\left(\frac{W^2 + M_X^2 - m_p^2}{2W}\right)^2 - M_X^2}\right)^2. \tag{6.9}$$

Notice that $t_{max} < t_{min} < 0$. Figure 6.3 shows the M_X^2-dependence of t_{min} and t_{max} for three fixed centre of mass energies $\langle W \rangle = 91$, 187 and 231 GeV. It is this integration over t that provides a differential cross section $M_X^2\ d\sigma/dM_X^2$ that goes to zero when M_X^2 approaches the available centre of mass energy squared, W^2.

To fit the fixed target data, expression (6.5) is used taken at the fixed value of $t = -0.05$ GeV^2.

Contributing terms

Since three trajectories are considered in the triple Regge fit, i.e. pomeron, reggeon and pion trajectory, 6 terms, shown in table 6.1 with their M_X^2- and W-dependences of the differential cross section $M_X^2\ d\sigma/dM_X^2$, will be present in the sum of equation (6.7). Here no interference terms are considered since no sensitivity was found to these terms [48], [51]. For completeness, the M_X^2- and W-dependences of the interference terms are however mentioned in table 6.1.

The pomeron exchange terms[2], i.e. $I\!P I\!P I\!P$ and $I\!P I\!P I\!R$, are approximately independent of W^2. In the diagram from figure 2.17.c) with $ijk = I\!P I\!P I\!R$, the k reggeon must have the

[2]This terminology is used since a pomeron is exchanged between the photon and proton and nothing is restricting the k-exchange from figure 2.17 diagram c) to be a pomeron or a reggeon. So both can contribute to the cross section.

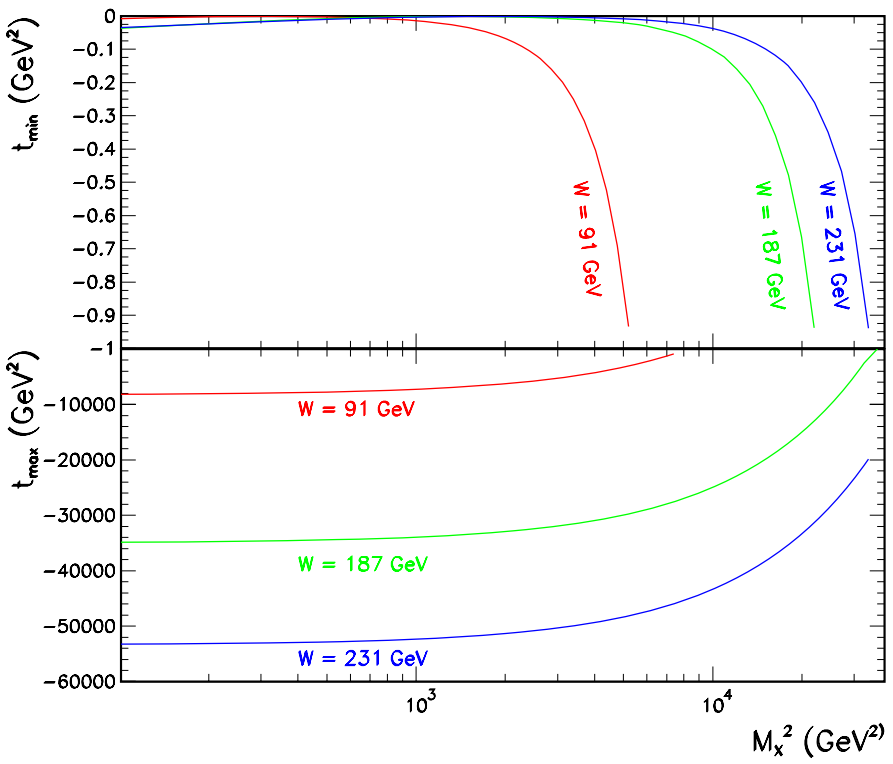

Figure 6.3: *t_{min} and t_{max} variation as a function of M_X^2 for three centre of mass energies.*

quantum numbers of the f (as mentioned in table 6.1 by "Specific terms ijk") in order to satisfy the C-parity conservation at the photon vertex and the C- and G-parity conservation at the three-reggeon vertex. No term like $I\!P I\!P \pi$ has to be considered since the G-parity at the three-reggeon has to be conserved. The $I\!P I\!P I\!P$ term will be approximately independent of M_X^2 while the $I\!P I\!P I\!R$ term will decrease with $1/M_X^2$.

The reggeon exchanged terms[3], here representing the isoscalars f and ω and the isovectors ρ and a, i.e. $I\!R I\!R I\!P$ and $I\!R I\!R I\!R$, are suppressed by factors $1/W^2$ at fixed M_X^2 with respect to the pomeron exchanges. Both terms increase with M_X: the term $I\!R I\!R I\!R$ rises linearly while $I\!R I\!R I\!P$ does it quadratically.

The pion exchange terms, i.e $\pi\pi I\!P$ and $\pi\pi I\!R$, are suppressed by factors $1/W^4$ and will be important at low centre of mass energies although they rise like M_X^4 for the term $\pi\pi I\!P$ and like M_X^3 for $\pi\pi I\!R$.

[3]The pion is considered as an additional exchange due to a different flux parameterization.

Generic term ijk	Specific terms ijk	Approx. W dependence	Approx M_X^2 dependence
$I\!P I\!P I\!P$	$I\!P I\!P I\!P$	W^0	M_X^0
$I\!P I\!P I\!R$	$I\!P I\!P f$	W^0	M_X^{-1}
$I\!R I\!R I\!P$	$ff I\!P$ $aa I\!P^\star$ $\rho\rho I\!P^\star$ $\omega\omega I\!P$	W^{-2}	M_X^2
$I\!R I\!R I\!R$	fff $aaf^\star$ $\rho\rho f^\star$ $\omega\omega f$ afa $\rho\omega a$	W^{-2}	M_X^1
$\pi\pi I\!P$	$\pi\pi I\!P$	W^{-4}	M_X^4
$\pi\pi I\!R$	$\pi\pi f$	W^{-4}	M_X^3
$\{I\!P I\!R\} I\!P$	$\{I\!P f\} I\!P$	W^{-1}	M_X^1
$\{I\!P I\!R\} I\!R$	$\{I\!P f\} f$ $\{I\!P f\} a$	W^{-1}	M_X^0

Table 6.1: *The possible triple Regge amplitudes considering $I\!P$-, $I\!R$- and π-exchange with their W^2- and M_X^2-dependence on the differential cross section $M_X^2 d\sigma/dM_X^2$, under the assumption that $\alpha_{I\!P}(t) = 1$ and $\alpha_{I\!R}(t) = 0.5$. The specific terms are the possible once taking the C- and G-parity conservation into account.*

Isospin consideration

When the final state of the scattered proton is not measured, as in the case for the RG data, higher mass proton excitations like ($Y = n$, $N^\star$, Δ^{++}, Δ^+, Δ^0,...) can be formed or even small dissociative masses can be formed with $M_Y < 1.6$ GeV (see figure 6.4). Since those Δ-states have higher isospin than the proton they can only be produced via isovector exchanges (i.e. $i = j = \rho$, a or $\pi^\pm$). Such processes are described in the same way as processes that are elastic at the proton vertex up to a Clebsch-Gordan coefficient. This can lead to additional exchanges. To take those extra exchanges correctly into account, some additional isospin assumptions are made in the fit, describing the RG data with respect to the tagged proton data. The terms in which isospin is exchanged are marked with a star in table 6.1.

The isospin assumptions for the π- and $I\!R$-exchange will be discussed below:

- **π-exchange**
  In the case of π-exchange (figure 6.5) between the photon and proton[4] the decay in which isospin is exchanged, i.e. $p \to n\pi^+$, is enhanced by a factor of two with respect to the decay where isospin is conserved in the exchange ($p \to p\pi^0$) due to Clebsch-Gordan coefficients. Assuming factorization between the top and bottom vertex in figure 6.4 it is appropriate to multiply the terms $\pi\pi I\!P$ and $\pi\pi I\!R$ from equation (6.7) with a factor of three [63] for the rapidity gap data, in which both decays $p \to n\pi^+$ and $p \to p\pi^0$ have to be considered, with respect to the tagged proton data samples[5] in which only the decay $p \to p\pi^0$ has to be considered.

[4]This is the dominant exchange in the low z-region [63] (z <0.9).

[5]Here the production of higher resonance states of the proton are neglected regarding the lower production probability due to their enhanced masses.

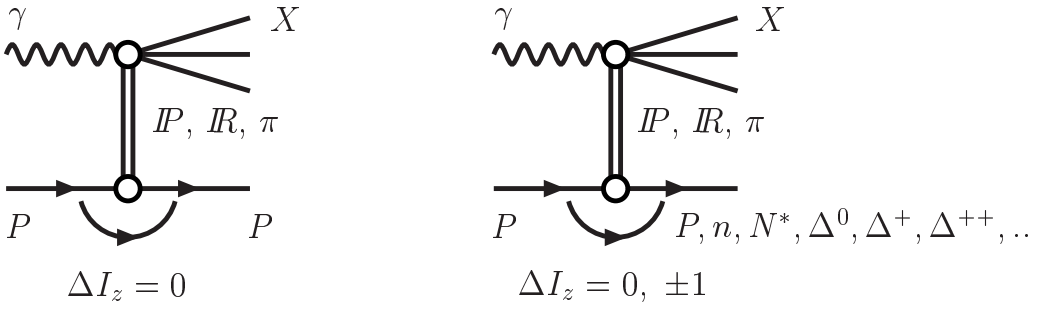

Figure 6.4: *Tagging the scattered proton, only isoscalars can be exchanged between the photon and the proton (left). Isoscalars and isovectors can be exchanged when the final state proton is not tagged (right) which is the case for the rapidity gap data.*

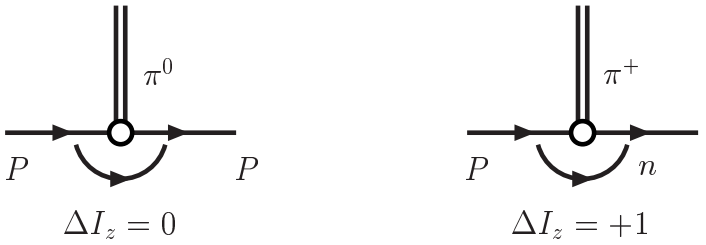

Figure 6.5: $p \to p\pi^0$ *and* $p \to n\pi^+$ *decays will lead to a coupling constant* $G(p \to n\pi^+)$ *which is two times bigger than* $G(p \to p\pi^0)$ *due to the appropriate Clebsch-Gordan factor.*

- **$I\!R$-exchange**
  Due to the unknown mixture of isoscalars (f, ω) and isovectors (a, ρ) in the $I\!R$-exchange case, no single value like in the case of π-exchange can be attributed to those exchanges. Therefore a new fit parameter $\mathcal{R}$, defined as the ratio of the sum $\sum_{k=I\!P,I\!R} I\!R I\!R k$ of the tagged proton to the RG, was introduced to take into account the isospin exchange contributions in the RG data sample which are not present in the tagged proton data samples. This means that the terms $I\!R I\!R I\!P$ and $I\!R I\!R I\!R$ from equation (6.7) are multiplied by the free parameter $\mathcal{R}$ in the fit formula for the RG data sample.

  If there were no isovector contributions to the subleading exchanges, then one expects that $\mathcal{R} = 1$, the presence of the ρ and a isovectors would increase $\mathcal{R}$. If one assumes only isovector contributions to the subleading exchange, then one would expect $\mathcal{R} = 3$ under the same assumption that only the proton and neutron are considered as

the proton final state. Introducing also the isoscalars to the subleading exchange will decrease $\mathcal{R}$[6].

Fit results

The triple Regge fit is obtained using the MINUIT [97] minimization program which performed the χ^2-minimization (using the statistical error on the cross sections only) and the error analysis. The result of the combined triple Regge fit (i.e. RG, FPS [69] and FT [74]) is shown in figure 6.6. The differential cross section extracted from the RG data for the three centre of mass energies $\langle W \rangle$=91, 187 and 231 GeV, from the FPS data for the same centre of mass energies and the differential cross section at fixed t performed on low energy FT data, W= 12.9 and 15.3 GeV, are all shown in figure 6.6. The result of the fit is given by the black line while the individual pomeron, reggeon and pion exchanges are represented by the different linetypes mentioned in the legend. From the combined fit the following qualitative result is derived:

1. Rapidity gap data are dominated by pomeron exchange, while the subleading reggeons contribute at high values of $x_{I\!P}$ (i.e. high M_X^2). Pion exchanges can be neglected completely in this low $x_{I\!P}$-region (i.e. $x_{I\!P} < 0.025$).

2. Leading proton data are dominated by subleading reggeon and pion exchanges.

3. Fixed target data are dominated by subleading reggeon exchanges over the complete mass range considered.

Points 1. and 2. mentioned above are in good agreement with the results obtained from the effective intercept, where the rapidity gap data were also dominated by pomeron exchange and the leading proton data by subleading exchanges and pion exchange.

The extracted values of the triple Regge couplings $G_{iik}(0)$ and the pomeron intercept $\alpha_{I\!P}(0)$ are shown in table 6.2 together with a triple Regge fit using the ZEUS LPS data discussed in section 6.2.2.

Apart from the statistical uncertainty, two types of systematic uncertainties have been considered. The errors labelled under "syst" in table 6.2, are those obtained by shifting the data points over their systematic uncertainties as discussed in section 5.2. The systematic uncertainties listed under "model" in table 6.2 are those obtained by varying the fixed parameters (see tabel 2.3) in the fit by their systematic uncertainties and adding them in quadrature. As can be seen the largest error on the fitted parameters comes from the "model" errors, which in term are dominated by the uncertainty on $\alpha_{I\!R}$ (i.e. about 90% of the total model error).

The correlations between the different parameters are quite large and hence the parameters are quite dependent on each other. This is not totally unexpected when investigating their M_X^2- and W-dependence over the limited M_X^2- and W-range.

[6]When higher proton resonances or even final proton states with a dissociative mass $M_Y < 1.6$ GeV are considered, $\mathcal{R}$ can become bigger than 3.

para	value	stat	syst	mod	Correlation coefficient						
	H1 FPS ("Fit a 1997")				$G_{\mathbb{P}\mathbb{P}\mathbb{P}}$	$G_{\mathbb{P}\mathbb{P}\mathbb{R}}$	$G_{\mathbb{R}\mathbb{R}\mathbb{P}}$	$G_{\mathbb{R}\mathbb{R}\mathbb{R}}$	$G_{\pi\pi\mathbb{P}}$	$G_{\pi\pi\mathbb{R}}$	$\mathcal{R}$
$\alpha_{\mathbb{P}}(0)$	1.127	$\pm$0.004	$\pm$0.025	$\pm$0.046	0.91	-0.99	-0.99	-0.99	0.98	0.98	-0.52
$G_{\mathbb{P}\mathbb{P}\mathbb{P}}$	1.34	$\pm$0.02	$\pm$0.64	$\pm$1.15		-0.92	-0.92	-0.92	0.91	-0.92	-0.49
$G_{\mathbb{P}\mathbb{P}\mathbb{R}}$	1.9	$\pm$0.5	$\pm$1.1	$\pm$1.9			0.99	0.99	-0.98	0.99	0.51
$G_{\mathbb{R}\mathbb{R}\mathbb{P}}$	6.0	$\pm$1.9	$\pm$4.3	$\pm$5.1				0.99	-0.98	0.98	0.48
$G_{\mathbb{R}\mathbb{R}\mathbb{R}}$	660	$\pm$70	$\pm$60	$\pm$450					-0.98	0.99	0.51
$G_{\pi\pi\mathbb{P}}$	40	$\pm$2	$\pm$13	$\pm$18						-0.97	-0.50
$G_{\pi\pi\mathbb{R}}$	910	$\pm$90	$\pm$300	$\pm$480							0.52
$\mathcal{R}$	11.4	$\pm$0.2	$\pm$2.7	$\pm$6.3							
χ^2/ndf	162/48										
	"Fit c 1994"				$G_{\mathbb{P}\mathbb{P}\mathbb{P}}$	$G_{\mathbb{P}\mathbb{P}\mathbb{R}}$	$G_{\mathbb{R}\mathbb{R}\mathbb{P}}$	$G_{\mathbb{R}\mathbb{R}\mathbb{R}}$	$\mathcal{R}$		
$\alpha_{\mathbb{P}}(0)$	1.071	$\pm$0.024	$\pm$0.02	$\pm$0.02	-0.98	-0.93	-0.85	0.92	0.80		
$G_{\mathbb{P}\mathbb{P}\mathbb{P}}$	3.76	$\pm$1.62	$\pm$2.25	$\pm$1.45		0.83	0.83	-0.89	-0.82		
$G_{\mathbb{P}\mathbb{P}\mathbb{R}}$	7.46	$\pm$3.73	$\pm$2.81	$\pm$2.67			0.84	-0.90	-0.75		
$G_{\mathbb{R}\mathbb{R}\mathbb{P}}$	63.8	$\pm$70.7	$\pm$17.7	$\pm$39.7				-0.99	-0.98		
$G_{\mathbb{R}\mathbb{R}\mathbb{R}}$	264	$\pm$344	$\pm$27	$\pm$159					0.95		
$\mathcal{R}$	4.56	$\pm$3.60	$\pm$1.74	$\pm$1.4							
χ^2/ndf	18.4/29										
	ZEUS LPS ("Fit b 1997")				$G_{\mathbb{P}\mathbb{P}\mathbb{P}}$	$G_{\mathbb{P}\mathbb{P}\mathbb{R}}$	$G_{\mathbb{R}\mathbb{R}\mathbb{P}}$	$G_{\mathbb{R}\mathbb{R}\mathbb{R}}$	$G_{\pi\pi\mathbb{P}}$	$G_{\pi\pi\mathbb{R}}$	$\mathcal{R}$
$\alpha_{\mathbb{P}}(0)$	1.084	$\pm$0.006	$\pm$0.03	$\pm$0.033	-0.98	-0.92	0.74	0.77	-0.95	-0.16	-0.68
$G_{\mathbb{P}\mathbb{P}\mathbb{P}}$	3.06	$\pm$0.32	$\pm$2.38	$\pm$1.89		0.84	-0.73	-0.77	0.93	0.14	0.59
$G_{\mathbb{P}\mathbb{P}\mathbb{R}}$	4.1	$\pm$0.7	$\pm$1.4	$\pm$2.9			-0.74	-0.71	0.89	0.19	0.81
$G_{\mathbb{R}\mathbb{R}\mathbb{P}}$	50	$\pm$18	$\pm$22	$\pm$44				0.51	-0.79	0.30	-0.69
$G_{\mathbb{R}\mathbb{R}\mathbb{R}}$	401	$\pm$75	$\pm$164	$\pm$250					-0.72	-0.13	-0.59
$G_{\pi\pi\mathbb{P}}$	92	$\pm$19	$\pm$42	$\pm$78						0.08	0.67
$G_{\pi\pi\mathbb{R}}$	0	$\pm$260	$\pm$0.07	$\pm$0.001							-0.07
$\mathcal{R}$	4.3	$\pm$1.1	$\pm$1.0	$\pm$2.0							
χ^2/ndf	119/38										

Table 6.2: *Obtained values and correlation coefficients for the triple Regge couplings and the pomeron intercept $\alpha_{\mathbb{P}}(0)$ from two combined triple Regge fits. "H1 leading proton" indicates that the fit is performed over RG, H1 FPS and FT data, "ZEUS leading" proton indicates that the fit is performed over RG, ZEUS LPS and FT data. The statistical, systematical and model uncertainties are given together with the values obtained from a similar triple Regge fit performed on RG obtained in 1994 and the same FT data as before. The triple Regge couplings are expressed in $\mu b/GeV^2$.*

As mentioned in the χ^2 fit only statistical errors are considered, which are by far the smallest. Due to the large systematics, the χ^2 value of the fit is rather large, although the triple Regge fit describes the data reasonably well.

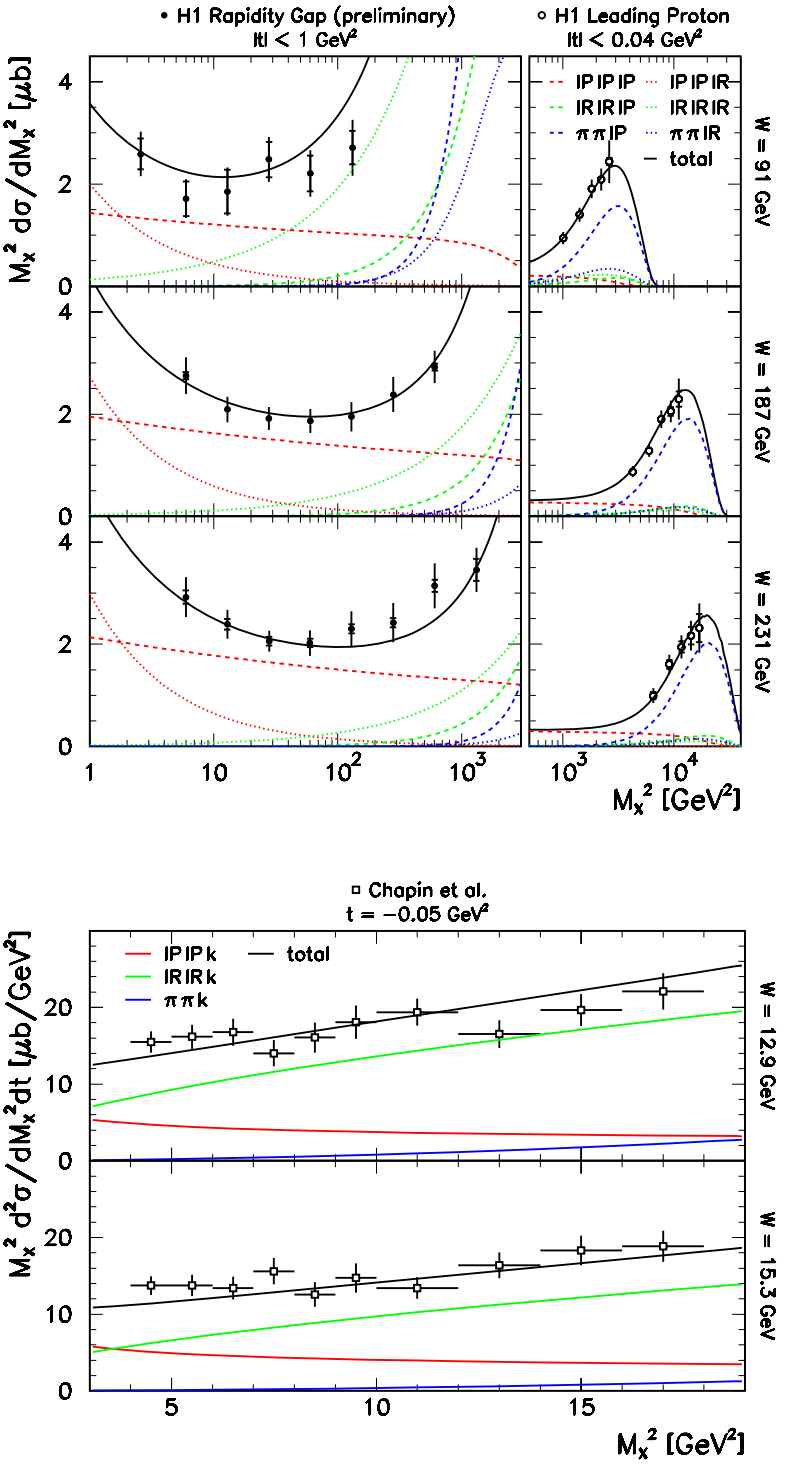

Figure 6.6: *The triple Regge fit performed over the RG data, H1 FPS data and FT data.*

The obtained values are compared with those obtained from an earlier analysis called "Fit c 1994" [68]. In this fit the same assumptions were made except from the fact that no pion exchanges were considered. This is a natural choice since no leading proton data, where pion exchange becomes important, are used in this fit. The pomeron intercept and the couplings obtained in the present analysis are in good agreement with the 1994 result within the errors as shown in table 6.2.

The fit, called "Fit a 1997", yields the result $\mathcal{R} = 11.4 \pm 0.2$ (stat)± 6.8 (syst), significantly larger than the maximum expected value of 3. This suggests that a more complex treatment of the subleading exchanges is required for a complete description, probably including the production of other baryon resonances in the rapidity gap data. However, the value obtained for $\alpha_{I\!P}(0) = 1.127 \pm 0.004$ (stat) ± 0.025 (syst) ± 0.046 (model) is stable with respect to different assumptions concerning the subleading exchanges.

The new measurement of $\alpha_{I\!P}(0)$ from "Fit a 1997", shown in figure 6.7 as a function of Q^2, is in good agreement with previous results from H1 and ZEUS. A possible indication of a rising pomeron intercept is seen as a function of Q^2.

Additional triple Regge fit considerations

To get an idea of how the triple Regge fit depends on the presence of the H1 FPS data, two additional fits will be presented bellow. The first one is based on the RG and the FT data only and the second one is performed on the RG, H1 FPS at only one centre of mass energy (W=187 GeV) and the FT data.

- **Fit to RG and FT**
  The result for which the two pion couplings were constrained to be positive (i.e. the physical domain for a triple Regge coupling) is shown in table 6.3 and figure 6.8. From the figure one sees that if the FPS data are not included in the minimization procedure, the fit result does not describe the very high mass region from the FPS data. This means that the triple Regge fit is really sensitive to the FPS data.

- **Fit to RG, FPS (W=187 GeV) and FT**
  A fit to RG, FPS at only one centre of mass energy ($\langle W \rangle$=187 GeV) and FT was performed, to see the effect on the parameters when the cross section measurement on the FPS data at only one centre of mass energy was used. The coupling $G_{\pi\pi I\!R}$ was forced to stay in the physical zone (i.e. a positive coupling was required for $G_{\pi\pi I\!R}$). The result of the fit is shown in table 6.4 and figure 6.9. The conclusion of this fit is that when the H1 leading proton differential cross section, measured at only one centre of mass energy, is included in the fit the parameter $\mathcal{R}$ becomes much larger then when no FPS data are included in the fit and that the normalization of the triple Regge curves are reasonably described at the two other centre of mass energy measurements although they were not included in the fit.

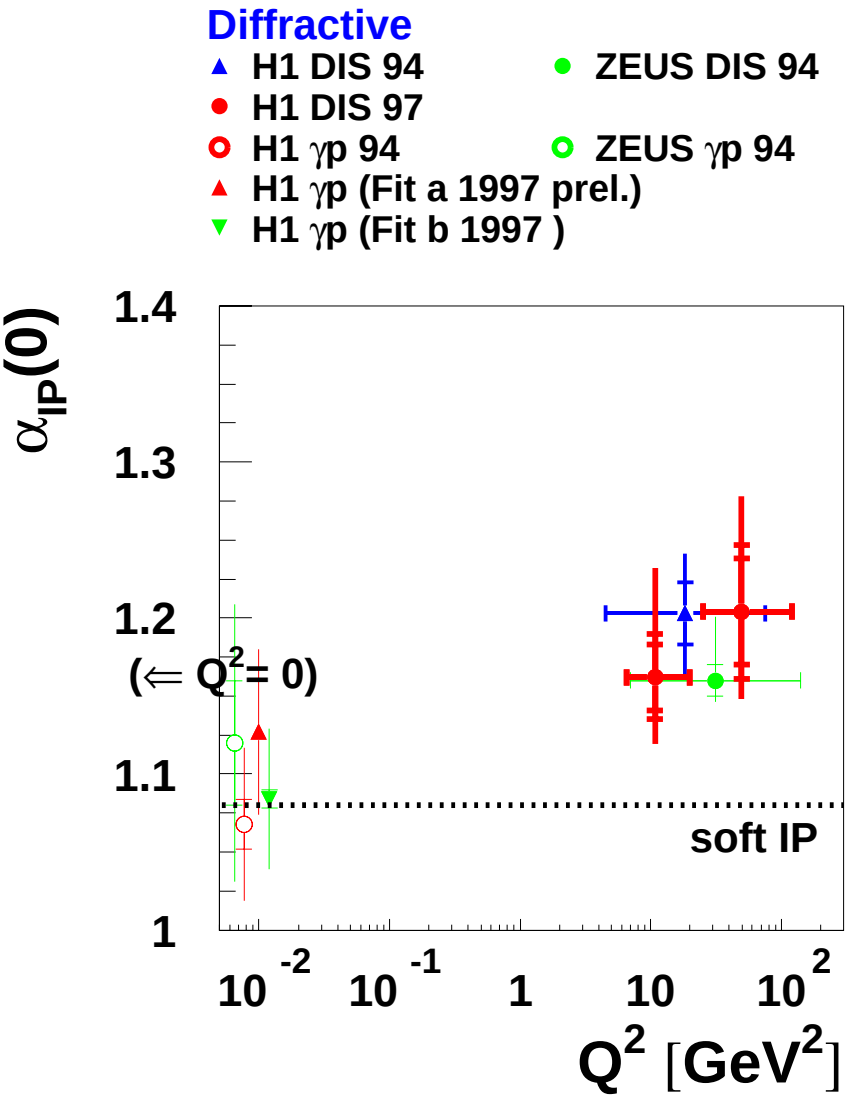

Figure 6.7: *A summary of H1 $\alpha_{I\!P}(0)$ measurements versus Q^2 for $\gamma^{(*)}p \to Xp$. A previous ZEUS result [77] at $Q^2 = 0$ is also shown.*

6.2.2 Triple Regge fit (ZEUS)

Very recently the ZEUS Collaboration came up with their differential cross section measurement based on tagged leading proton data (LPS) [98]. Since the H1 (FPS) and ZEUS (LPS) leading proton measurement differed by a factor of almost two (see section 2.6.2, figure 2.19), I decided to redo the triple Regge fit based on the LPS measurement to see

parameter	value		stat		syst		mod
$\alpha_{I\!P}(0)$	1.0947	$\pm$	0.007	$\pm$	0.0384	$\pm$	0.0321
$G_{I\!P I\!P I\!P}$	2.5026	$\pm$	0.277	$\pm$	2.1122	$\pm$	1.5635
$G_{I\!P I\!P I\!R}$	3.3813	$\pm$	0.631	$\pm$	1.4561	$\pm$	2.4049
$G_{I\!R I\!R I\!P}$	37.122	$\pm$	13.9	$\pm$	23.541	$\pm$	21.145
$G_{I\!R I\!R I\!R}$	496.68	$\pm$	61.9	$\pm$	176.05	$\pm$	329.51
$G_{\pi\pi I\!P}$	0.0002	$\pm$	13.5	$\pm$	0.0001	$\pm$	0.0015
$G_{\pi\pi I\!R}$	0.0025	$\pm$	250	$\pm$	0.0207	$\pm$	0.0069
$\mathcal{R}$	5.6652	$\pm$	1.4	$\pm$	1.5217	$\pm$	2.5881

Table 6.3: *Obtained values for the triple Regge couplings and the pomeron intercept $\alpha_{I\!P}(0)$ from a combined triple Regge fit over RG and FT. No leading proton data were used. The couplings $G_{\pi\pi I\!P}$ and $G_{\pi\pi I\!R}$ were constrained to be positive.*

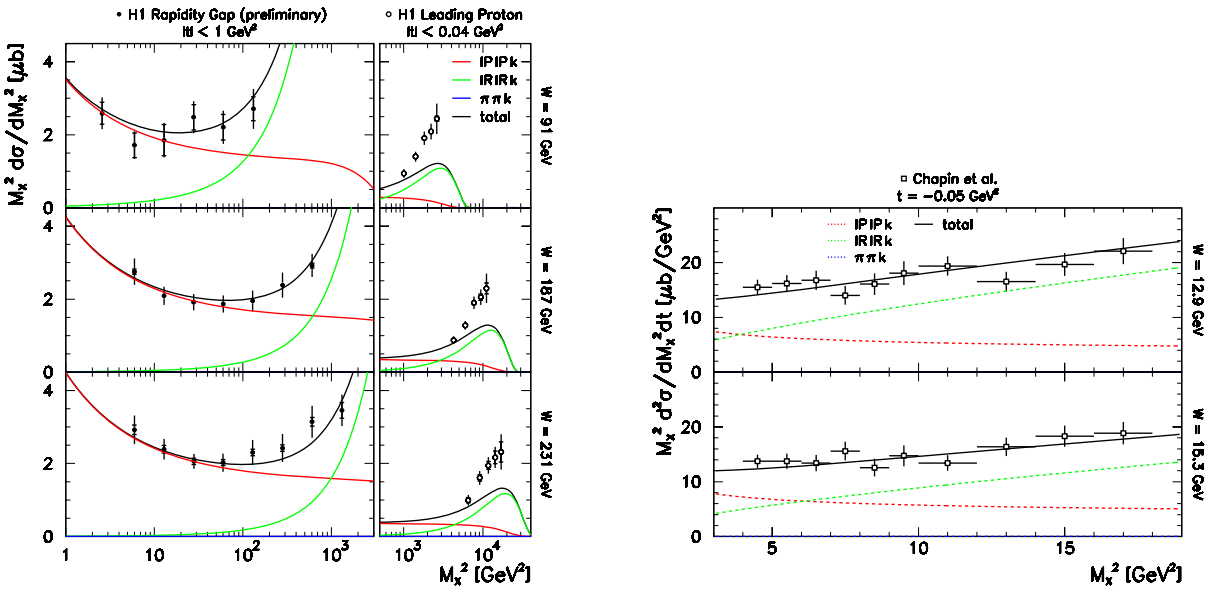

Figure 6.8: *The triple Regge fit performed over the rapidity gap data and fixed target data. The data points from the FPS cross section measurement were added to the figure.*

what the effect on the parameters is. The result of that fit denoted by "Fit b 1997", is given in table 6.2 and represented in figure 6.10. Note that the ZEUS collaboration measured the cross section on the leading proton data at only one centre of mass energy and the result can thus directly be compared with figure 6.9 and table 6.4, where also one centre of mass energy from the FPS data was included in the fit.

"Fit b 1997" yields a slightly softer pomeron of $\alpha_{I\!P}(0) = 1.084 \pm 0.006$ (stat) $\pm$ 0.03 (syst) $\pm$0.033(model) (also shown in figure 6.7) and the result on the isospin parameter,

parameter	value		stat		syst		mod
$\alpha_{I\!P}(0)$	1.1224	$\pm$	0.007	$\pm$	0.028	$\pm$	0.045
$G_{I\!P I\!P I\!P}$	1.5114	$\pm$	0.17	$\pm$	0.902	$\pm$	1.251 μb GeV^{-2}
$G_{I\!P I\!P I\!R}$	1.9527	$\pm$	0.4	$\pm$	0.705	$\pm$	1.886 μb GeV^{-2}
$G_{I\!R I\!R I\!P}$	12.459	$\pm$	3.3	$\pm$	5.121	$\pm$	8.908 μb GeV^{-2}
$G_{I\!R I\!R I\!R}$	662.46	$\pm$	34	$\pm$	58.52	$\pm$	457.8 μb GeV^{-2}
$G_{\pi\pi I\!P}$	37.615	$\pm$	4.3	$\pm$	12.18	$\pm$	17.17 μb GeV^{-2}
$G_{\pi\pi I\!R}$	0.0002	$\pm$	125	$\pm$	0.003	$\pm$	0.002 μb GeV^{-2}
$\mathcal{R}$	8.9357	$\pm$	1.0	$\pm$	1.970	$\pm$	4.500

Table 6.4: *Obtained values for the triple Regge couplings, the pomeron intercept $\alpha_{I\!P}(0)$ and the isospin parameter $\mathcal{R}$ from a combined triple Regge fit over RG, FPS ($\langle W\rangle$=187 GeV only) and FT. The FPS at $\langle W\rangle$= 91 and 231 GeV were not used. The fit constrained $G_{\pi\pi I\!R}$ to be positive.*

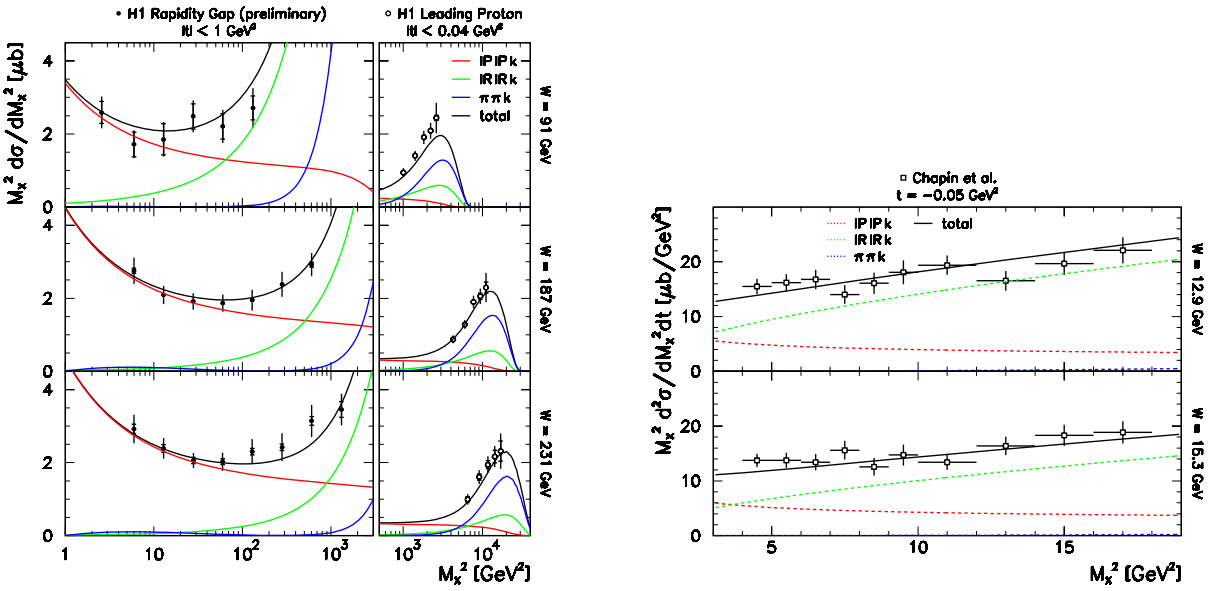

Figure 6.9: *The triple Regge fit performed over the rapidity gap data, H1 leading proton data at $\langle W\rangle$= 187 GeV and fixed target data. The fit constrained $G_{\pi\pi I\!R}$ to be positive.*

$\mathcal{R} = 4.3 \pm 1.1$ (stat) $\pm$ 2.2 (syst), is in better agreement with "Fit c 1994" and the expected value of 3. The pion contribution is still the dominant exchange in the kinematical domain of the leading proton measurement, however a considerable amount from reggeon exchanges is also observed here.

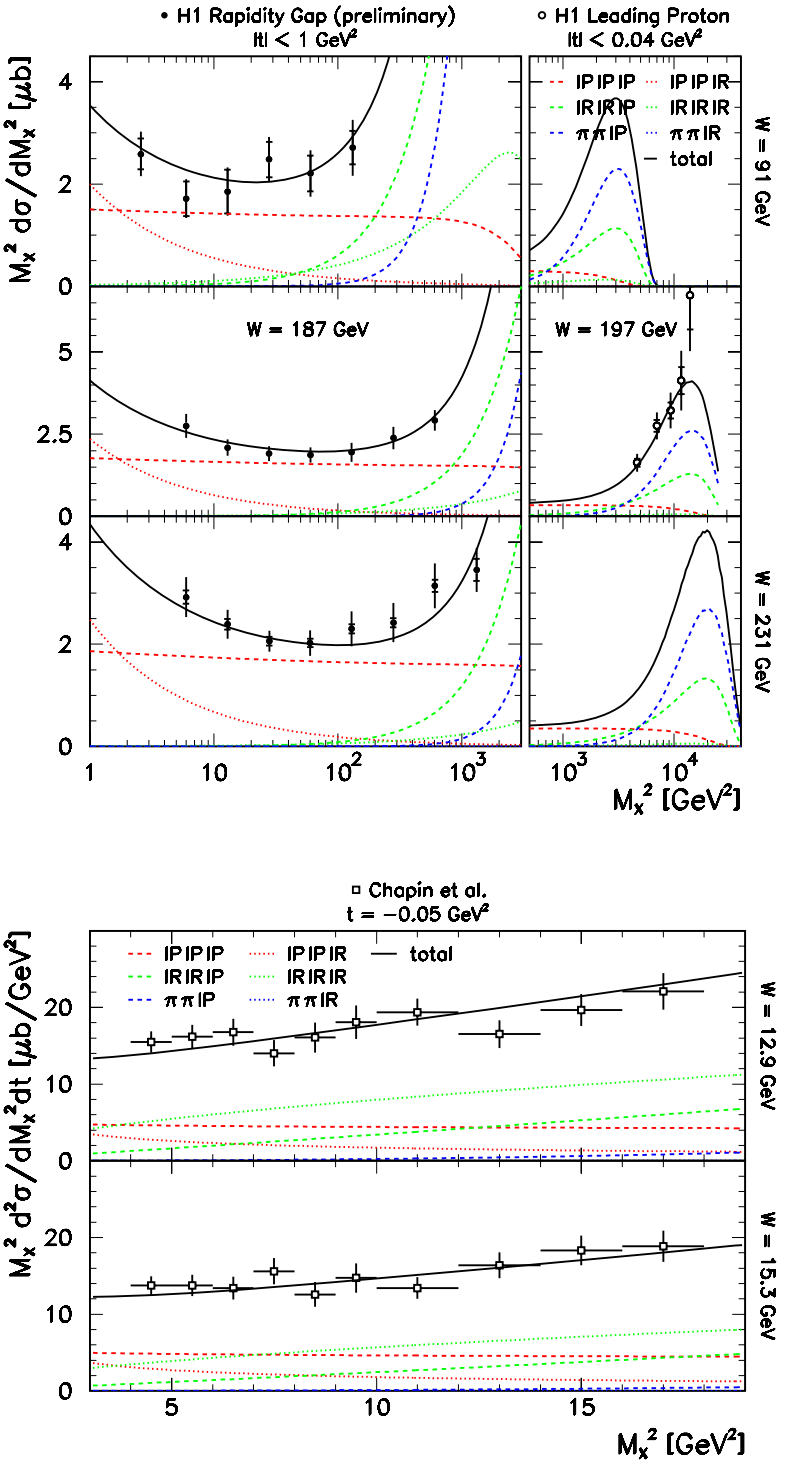

Figure 6.10: *The triple Regge fit performed over the rapidity gap data, ZEUS leading proton data and fixed target data.*

6.3 γp- versus pp-couplings: a comparison

The coupling constants determined in the previous section in γp-interactions have also been determined from inclusive reactions $pp \to X + p'$ (section 2.6.1). Assuming Regge factorization, one expects that both measurements are related in the limit of large s. Indeed, assuming factorization, the coupling $\beta_{\gamma k}(0)$ from equation (2.72) is proportional to $\sigma_{\gamma p}$ and hence the relation between the γp- and pp-couplings is given by,

$$\frac{G^{\gamma p}_{ijk}(t)}{G^{pp}_{ijk}(t)} = \frac{\sigma^{\gamma p}_{tot}}{\sigma^{pp}_{tot}} = 0.0032 \tag{6.10}$$

where $G^{\gamma p}_{ijk}(t) = \beta^2_{pi}(0)\beta_{\gamma k}(0)\ e^{(2b_{pi}+b_{ijk})t}$. The numerical value was obtained using the $\sigma^{\gamma p}_{tot}$ value from [99].

The results are shown in figure 6.11. The pp-data from Ganguli and Roy (section 2.6.1) are shown as a function of t and are also listed in table 2.2. The lines represent the result of an exponential fit to the pp-data. The result obtained from the present two triple Regge analyses[7], called "Fit a 1997" and "Fit b 1997" and renormalized using equation (6.10), are shown at the values of $t = 0$ GeV^2. Although the coupling constants deduced from the γp- and pp-data do not seem to agree very well, this comparison should be taken with care. First, the form of the t-dependence of the coupling constant is not unique; different parameterizations have been tried and result in variations of the values for the couplings at $t = 0$ GeV^2. For the $I\!P I\!P I\!P$-coupling, some models argue that the coupling should vanish at $t = 0$ GeV^2. Second, the Regge trajectories used in the pp-data, $\alpha_{I\!P}(t) = 1.0 + 0.25\ t$, $\alpha_{I\!R}(t) = 0.5 + t$ and $\alpha_\pi(t) = t$, are slightly different from those of the present triple Regge fit. As these parameters are quite strongly correlated to the couplings, this may result in some variations. Given these uncertainties, we conclude the consistency between the γp- and pp-couplings is reasonable.

6.4 Transition from the soft towards the deep inelastic region

As shown in section 6.2, the triple Regge formalism describes well the inclusive diffractive dissociation processes in photoproduction over a large M^2_X- and W-range. It is tempting to investigate to what extend the triple Regge formalism, describing "soft physics", could be extended to explain also the "low" Q^2 deep inelastic diffractive data. Here several measurements exist to test an extrapolation of photoproduction to the deep inelastic region: the diffractive structure function, $F_2^D(3)$[48], the diffractive structure function with a leading proton, F_2^{LP}[70],[102], and the diffractive structure function with a leading neutron, F_2^{LN}[103].

[7]Note that in figure 6.11 the dimension of the triple Regge couplings are expressed in mb/GeV^2 instead of $\mu b/GeV^2$ for the outcome of "Fit a 1997" and "Fit b 1997".

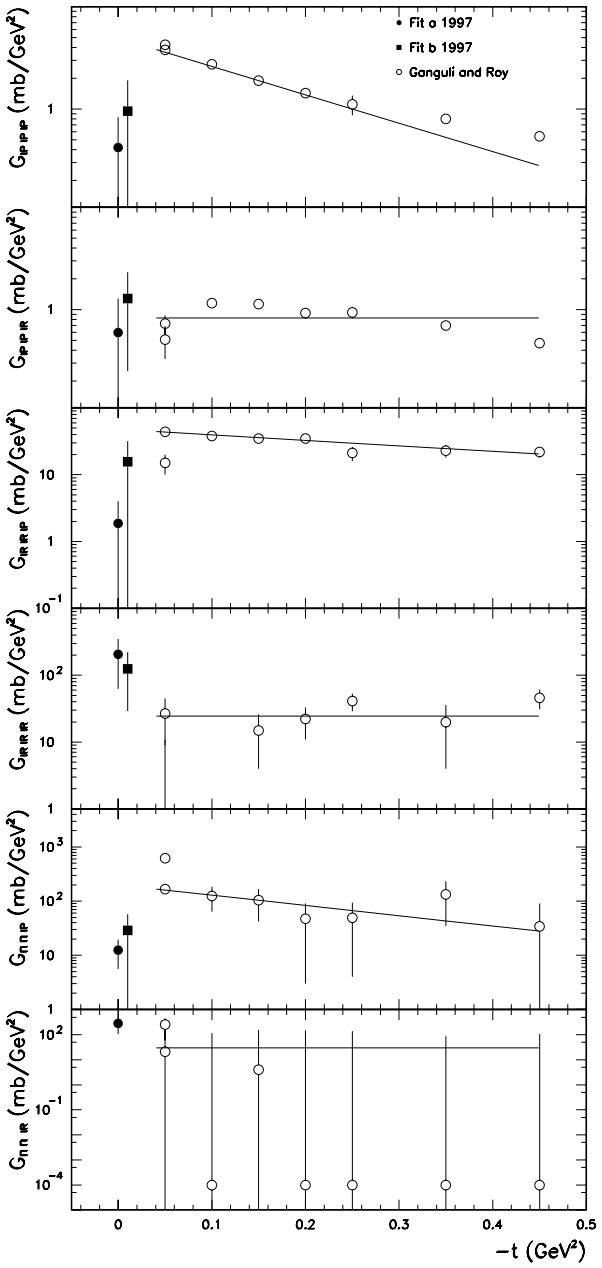

Figure 6.11: *Comparison of γp versus pp triple Regge couplings. The full line represents a simple exponential fit on the t-dependence to the triple Regge couplings obtained from the pp-data.*

The diffractive structure function can be written down in terms of the total diffractive

cross section,

$$\frac{d\sigma(\gamma^\star p \to Xp)}{dz} = \int \frac{d^2\sigma}{dzdt}dt = \frac{4\pi\alpha_{em}^2}{Q^2}F_2^{D(3)}(\beta, Q^2, x). \tag{6.11}$$

And using the right handside of equation (6.5) for $d\sigma/dz$ and the fact that

$$\frac{F_2(x,Q^2)}{\sigma_{tot}^{\gamma p}} = \frac{Q^2}{4\pi\alpha_{em}^2}, \tag{6.12}$$

one obtaines that $F_2^{D(3)}(\beta, Q^2)$ can be rewritten as:

$$F_2^{D(3)}(\beta,Q^2) = \int dt\ \frac{s_0}{W^2}\sum_{iik} G_{iik}^{\gamma p}(t)\left(\frac{W^2+Q^2}{M_X^2+Q^2}\right)^{2\alpha_i(t)}\left(\frac{M_X^2}{s_0}\right)^{\alpha_k(0)}\frac{F_2(x,Q^2)}{\sigma_{tot}^{\gamma p}}. \tag{6.13}$$

Here the Q^2-dependence in the derivation of the triple Regge expression (6.5) is taken into account leading to the replacement of $M_X^2/W^2 \to (M_X^2+Q^2)/(W^2+Q^2)$, i.e. $x_{I\!P}$ in respectively the photoproduction limit and in the deep inelastic region.

$F_2^{D(3)}$ can also be predicted using the pp-couplings instead of the γp-couplings. Therefore one has to replace $\sigma_{\gamma p}$ by σ_{pp} and the formula equivalent to equation (6.13) reads as,

$$F_2^{D(3)}(\beta,Q^2) = \int dt\ \frac{s_0}{W^2}\sum_{iik} G_{iik}^{pp}(t)\left(\frac{W^2+Q^2}{M_X^2+Q^2}\right)^{2\alpha_i(t)}\left(\frac{M_X^2}{s_0}\right)^{\alpha_k(0)}\frac{F_2(x,Q^2)}{\sigma_{tot}^{pp}}. \tag{6.14}$$

The same equations hold for the comparison with F_2^{LP} and F_2^{LN}.

Figure 6.12 shows the measured values of $F_2^{D(3)}$ as a function of $x_{I\!P}$ in bins of (β,Q^2) as well as the predictions from equation (6.13) and (6.14) using respectively the couplings obtained from the γp- and pp-data. In the low Q^2- and high M_X-region where the triple Regge model is applicable, the predictions follow the data quite well. Only at higher Q^2 they undershoot the data. As can be seen from expression (6.13), the Q^2-evolution predicted by the triple Regge model is approximately equal to the one exhibited by the inclusive F_2. This indicates that the diffractive structure function evolves faster than the Q^2-dependence present in the inclusive F_2 structure function.

Figure 6.13 and 6.14 show the diffractive structure function F_2^{LP}, obtained from the measured cross section of DIS events with a leading proton in the final state. Figure 6.14 shows the data corresponding to the large $x_{I\!P}$-range, ($x_{I\!P} > 0.3$) where the reggeon and pion exchanges are important. Again at low Q^2 the model predictions describe the data well irrespective whether γp- or pp-couplings are used. Also for the data at lower $x_{I\!P}$-values shown in figure 6.13 the model describes the data well although the predictions from equation (6.13) tend to be systematically above those from equation (6.14). It is interesting to note that in going to lower $x_{I\!P}$-values the dominance of the triple pomeron term increases as shown by the pure $1/x_{I\!P}$ behavior.

The diffractive structure function F_2^{LN}, obtained from the measured cross section of DIS events with a leading neutron in the final state, has also been measured and is shown in figure 6.15. This data sample contains only processes in which isovector exchanges take place between the photon and proton. This means that in the formula (6.13) and (6.14)

only reggeon terms (a- and ρ-exchange) and π-exchange terms have been considered. The model predictions are shown in figure 6.15. Unfortunately the comparison with the data can not be extended below $z < 0.7$ because then the M_X- and W-values become comparable and the triple Regge model is no longer valid. Nevertheless figure 6.15 indicates that the data above $z > 0.7$ are reproduced well.

6.5 Conclusion

The diffractive photoproduction data have been subjected to two types of Regge analysis: in the first one, done in the normal Regge limit, an effective pomeron intercept as a function of M_X^2 has been determined. In the second one, performed in the triple Regge limit, the pomeron intercept as well as the triple Regge couplings have been measured. The result of the first analysis showed that the process underlying the rapidity gap data is dominated by pomeron exchange. This is in contrast to the processes that control the leading proton data at higher values of M_X^2 where reggeon and pion exchange become dominant. Various data sets have been used to perform the more complex triple Regge fit. Due to strong correlations, the triple Regge couplings can not be well constrained. However the pomeron intercept extracted from the various fits is constrained well and its value was found to be compatible with the "soft pomeron" intercept of Donnachie and Landshoff. The discrepancy in the leading proton data between FPS and LPS, and the influence on the outcome of the triple Regge fit result has been investigated in detail. The effect of the different data sets on the value of the $\mathcal{R}$ parameter can be summarized as follows:

1. A value of $\mathcal{R}$=11.4±0.2±2.7±6.3 is found when the FT, RG and FPS data sets are used in the over-all fit.

2. Removing the FPS data from the fit reduces the value to $\mathcal{R}$=5.7±3.3 comparable with previous H1 analysis [68] mentioned in table 6.2 as "Fit c 1994".

3. Using the FT, RG and only one FPS data set at $\langle W \rangle$=187 GeV, one obtains $\mathcal{R}$=8.9±5.0. Hence the inclusion of a single FPS data point increases $\mathcal{R}$ substantially.

4. Using the FT, RG and LPS data set at $\langle W \rangle$=197 GeV, one obtains $\mathcal{R}$=4.3±2.5, in closer agreement with the result of point 2.

Assuming Regge factorization, the triple Regge coupling constants extracted from γp-interactions have been compared with those obtained in pp-data showing a reasonable agreement given the different assumptions made in both extractions.

Finally the predictions of a triple Regge model have been extended to the low Q^2 deep inelastic region and compared to $F_2^{D(3)}$, F_2^{LP} and F_2^{LN}. It has been found that the triple Regge model also describes the deep inelastic data in the triple regge range of validity, i.e. $M_X > 4$ GeV and $W^2 \gg M_X^2$ for not too high values of Q^2. From this study one can conclude that the transition between soft and hard diffraction is situated around $Q^2 \approx 12$ GeV^2.

Figure 6.12: *The measured values of $x_{I\!P} F_2^{D(3)}$ [48] compared with the predictions of the triple Regge model using either the couplings determined from data on $pp \to pX$ (Ganguli and Roy) represented by the full line or on $\gamma p \to Xp$ (Fit a 1997) represented by the dashed line.*

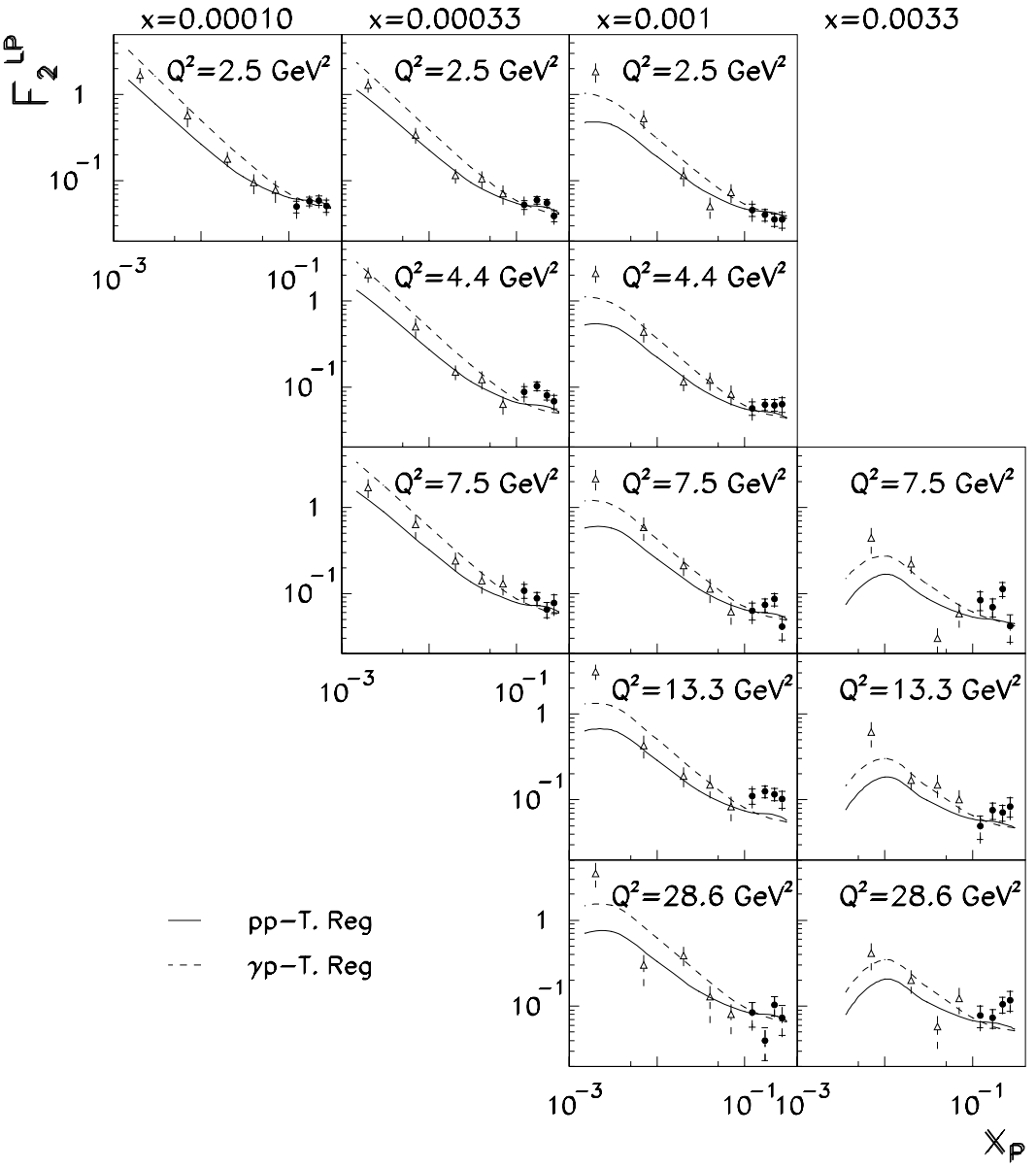

Figure 6.13: *The measured values of F_2^{LP} (solid circles [70], triangles [102]) with $p_T < 0.2$ GeV are compared with the predictions of the triple Regge model using either the couplings determined from data on $pp \to pX$ (Ganguli and Roy) or on $\gamma p \to Xp$ (Fit a 1997).*

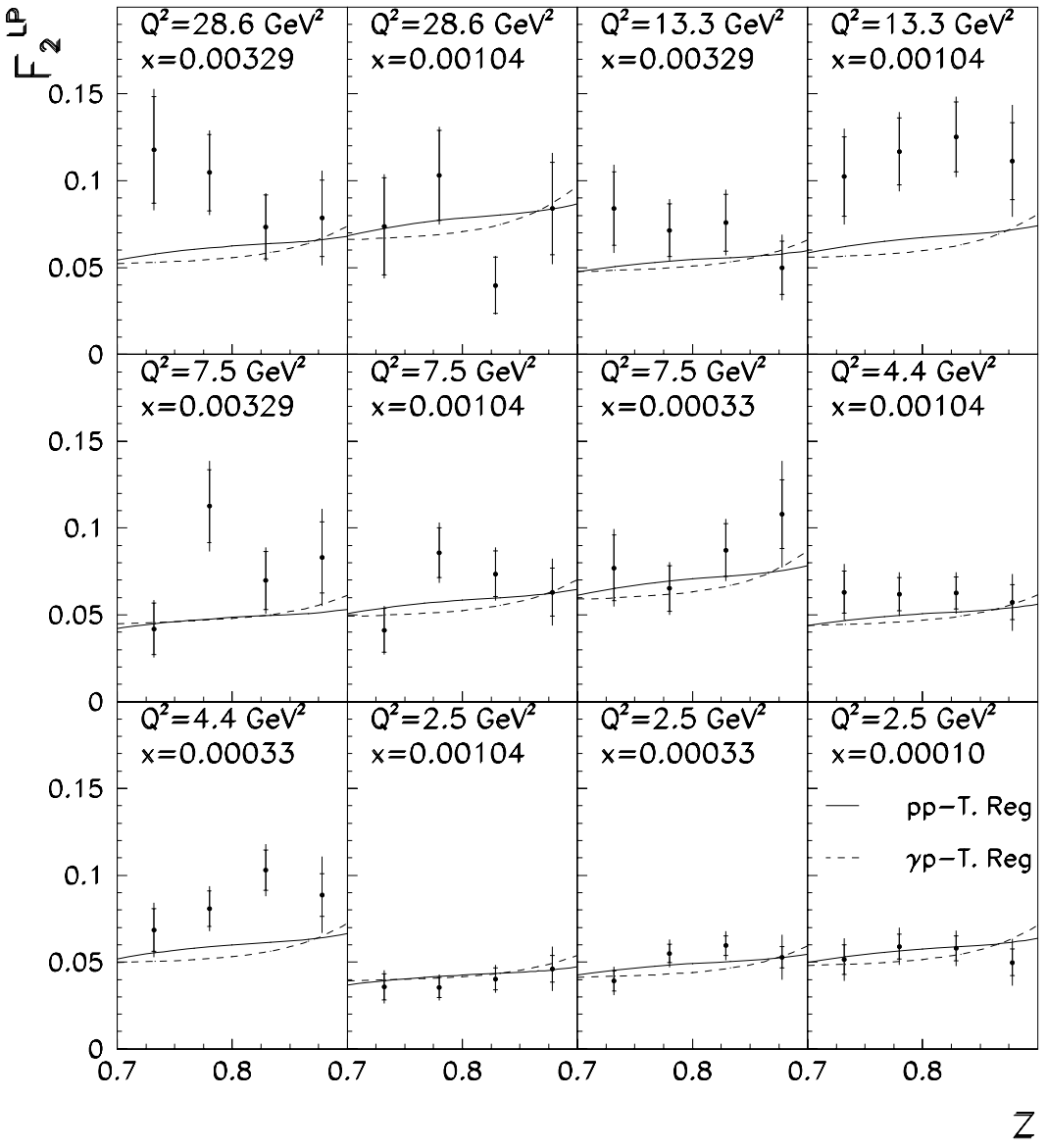

Figure 6.14: *The measured values of F_2^{LP}[70] with $p_T < 0.2$ GeV are compared with the predictions of the triple Regge model using either the couplings determined from data on $pp \to pX$ (Ganguli and Roy) or on $\gamma p \to Xp$ (Fit a 1997).*

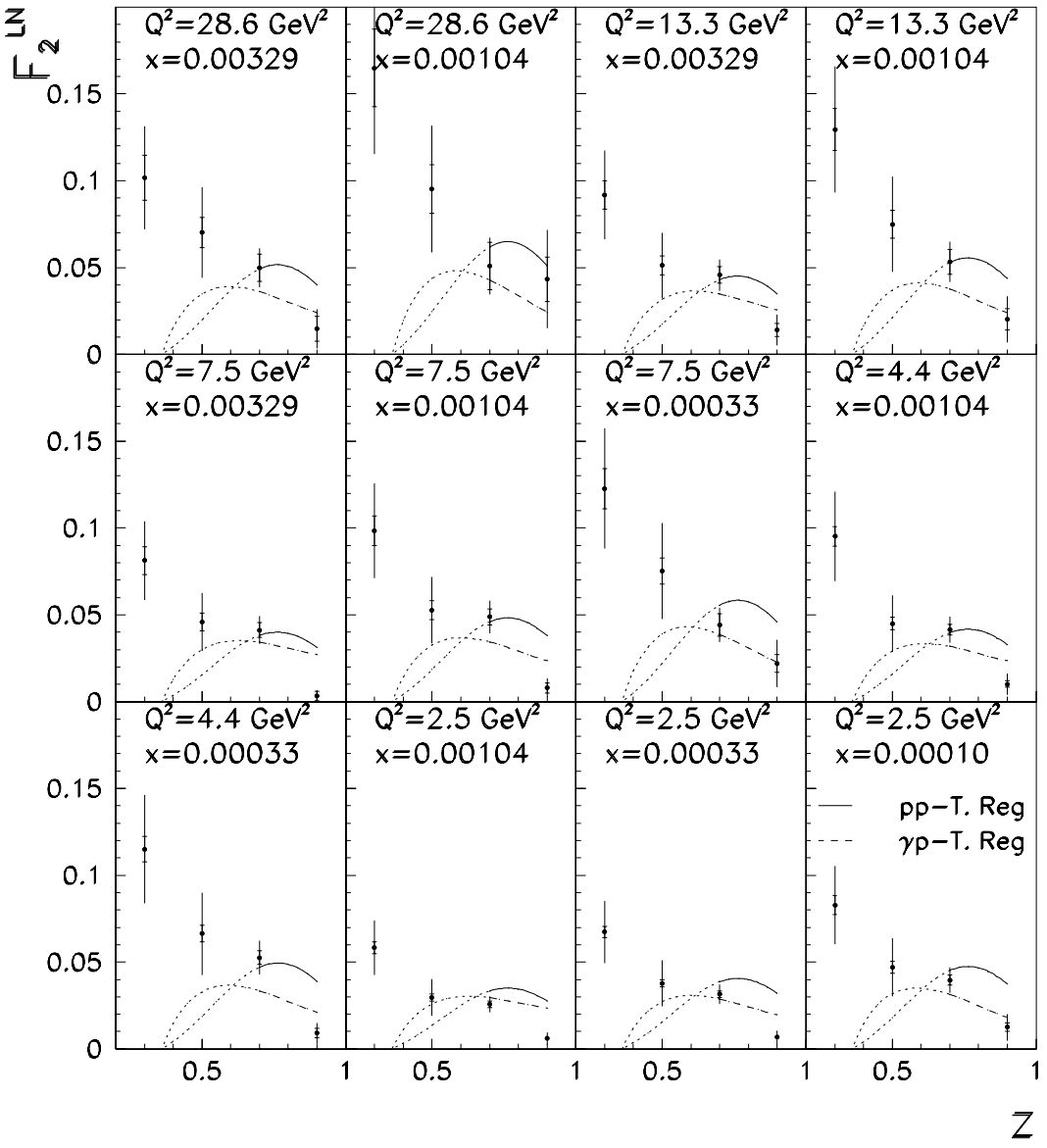

Figure 6.15: *The measured values of F_2^{LN}[103] with $p_T < 0.2$ GeV are compared with the predictions of the triple Regge model using either the couplings determined from data on $pp \to pX$ (Ganguli and Roy) or on $\gamma p \to Xp$ (Fit a 1997).*

Bibliography

[1] F.E. Close, *An Introduction to Quarks and Partons*, Academic Press, (1979)

[2] F. Halzen and A. Martin, *Quarks and Leptons*, John Wiley, (1984)

[3] C. Callan and D. Gross, *Phys. Rev. Lett.* **21** (1968) 311

[4] H1 Collaboration, *Phys. Lett.* **B393** (1997) 452, [arXiv:hep-ex/9611017]

[5] H1 Collaboration, *Eur. Phys. J.* **C21** (2001) 33, [arXiv:hep-ex/0012053]

[6] J.D. Bjorken, *Phys. Rev.* **163** (1967) 1767

[7] R.P. Feynman, *Phys. Rev. Lett.* **23** (1969) 1415

[8] R.P. Feynman, *Photon hadron interactions*, Benjamin (1972)

[9] E.D. Bloom et al., *Phys. Rev. Lett.* **23** (1969) 930

[10] M. Breidenbach et al., *Phys. Rev. Lett.* **23** (1969) 935

[11] NMC Collaboration, *Nucl. Phys.* **B483** (1997) 3

[12] BCDMS Collaboration, *Phys. Lett.* **B223** (1989) 485

[13] L.W. Whitlow et al., *Phys. Lett.* **B250** (1990) 193
L.W. Whitlow et al. *Phys. Lett.* **B282** (1992) 475

[14] H1 Collaboration, *Phys. Lett.* **B393** (1997), 452

[15] J.G.H. de Groot et al., *Z. Phys.* **C1** (1979), 143

[16] D.H. Perkins, *Introduction to High Energy Physics*, Addison Wesley Publishing Company Inc. (1987)

[17] H1 Collaboration, *Eur. Phys. J.* **C13** (2000) 609

[18] H1 Collaboration, *Eur. Phys. J.* **C19** (2001) 269

[19] ZEUS Collaboration, *Eur. Phys. J.* **C12** (2000) 411

[20] ZEUS Collaboration, *Eur. Phys. J.* **C21** (2001) 443, [arXiv:hep-ex/0105090]

[21] E665 Collaboration, *Phys. Rev.* **D54** (1996) 3006

[22] V.N. Gribov and L.N. Lipatov, *Sov. J. Nucl. Phys.* **15**, (1972) 438;
Yu.L. Dokshitzer, *Calculation of the structure function for deep inelastic and e^+e^- annihilation by perturbation theory in Quantum Chromodynamics* [in Russian] Sov. Phys. JETP **46** (1977) 641;
G. Altarelli and G. Parisi, *Nucl. Phys.* **B126** (1977) 298

[23] E. Kuraev, L. Lipatov, V. Fadin, *Sov. Phys. JETP* **44** (1976) 443
Y. Balitsky, L. Lipatov, *Sov. J. Nucl. Phys.* **28** (1978) 822

[24] C. Weizsäcker, *Z. Phys.* **88** (1934) 612
E. Williams, *Phys. Rev.* **45** (1934) 729

[25] S. Frixione et al., *Phys. Lett.* **B319** (1993) 339

[26] C. Friberg and T. Sjöstrand, preprint, [arXiv:hep-ph/0007314]

[27] T.H. Bauer et al., *Rev. Mod. Phys.* **50** (1978) 261

[28] G.A. Schuller and T. Sjöstrand, *Nucl. Phys.* **B407** (1993) 539

[29] G.A. Schuller and T. Sjöstrand, *Phys. Lett.* **B300** (1993) 169

[30] H1 Collaboration, *Nucl. Phys.* **B445** (1995) 195

[31] Zeus Collaboration, *Phys. Lett.* **B315** (1993) 481

[32] H1 Collaboration, *Nucl. Phys.* **B429** (1994) 477

[33] Y.L. Dokshitzer, V.A. Khoze, A.H. Mueller and S. Troyan, *Basics of perturbative QCD* (1991) Editions Frontieres, Grif-sur-Yvette, France

[34] J.J. Sakurai, *Ann. Phys.* **11** (1960) 1

[35] U. Amaldi, M. Jacob and G. Matthiae, *Ann. Rev. Nucl. Sci.* **26** (1976) 385

[36] A.B. Kaidalov, *Phys. Rep.* **50** (1979) 157

[37] K. Goulianos, *Phys. Rep.* **101** (1983) 169

[38] P.D. Collins, "An Introduction to Regge Theory and High-Energy Physics", *Cambridge Univ. Pr.*, 1977

[39] G. Alberi and G. Goggi *Phys. Rep.* **74** (1981) 1

[40] A. Barnes et al. *Phys. Rev. Lett.* **37** (1976) 76

[41] P. Landshoff *The two Pomerons* University of Cambridge, [arXiv:hep-ph/9410250]

[42] H1 Collaboration, *Z. Phys.* **C69** (1995) 27, [arXiv:hep-ex/9509001]

[43] H. Abramowicz et al., *Phys. Lett.* **B269** (1991) 465

[44] CDF Collaboration, *Phys. Rev.* **D50** (1994) 5518

[45] G. Ingelman and P.E. Schlein, *Phys. Lett.* **B152** (1985) 256

[46] J. Collins, *Phys. Rev.* **D57** (1998) 3051
J. Collins, *Phys. Rev.* **D61** (2000), [arXiv:hep-ph/019902]

[47] L. Trentadue, G. Veneziano, *Phys. Lett.* **B323** (1994) 201
A. Berera, D. Soper, *Phys. Rev.* **D50** (1994) 4328
M. Grazzini, L. Trentadue, G. Veneziano, *Nucl. Phys.* **B519** (1998) 394

[48] H1 Collaboration, *Z. Phys.* **C76** (1997) 613

[49] ZEUS Collaboration, *Eur. Phys. J.* **C6** (1999) 43

[50] H1 Collaboration, Measurement of the Diffractive Structure Function $F_2^{D(3)}$ at HERA, Paper submitted to International Europhysics Conference on High Energy Physics EPS 2001, Budapest, July 2001 (abstract 808). Available from http://www-h1.desy.de/h1/www/publications/htmlsplit/H1prelim-01-111.long.html

[51] H1 Collaboration, Measurement and NLO DGLAP QCD Interpretation of Diffractive Deep-Inelastic Scattering at HERA, Paper submitted to International Conference on High Energy Physics, ICHEP02, Amsterdam, July 2002 (abstract 980). Available from http://www-h1.desy.de/h1/www/publications/htmlsplit/H1prelim-02-012.long.html

[52] T.H. Bauer et al., *Rev. Mod. Phys.* **50** (1978) 261

[53] R.P. Feynman, *Phys. Rev. Lett.* **23** (1969) 1415

[54] A.H. Meuller, *Phys. Rev.* **D2** (1970) 2963

[55] Benecke et al., *Phys. Rev.* **188** (1969) 2159

[56] CHLM Collaboration, *Nucl. Phys.* **B72** (1974) 376

[57] R. Field and G. Fox, *Nucl. Phys.* **B80** (1974) 367

[58] A. Donnachie, P. Landshoff, *Nucl. Phys.* **B244** (1984) 322

[59] T. Inami and R. Roberts, *Nucl. Phys.* **B93** (1975) 497

[60] K. Hidaka, *Phys. Rev.* **D16** (1977) 690

[61] D. Roy and R. Roberts, *Nucl. Phys.* **B77** (1974) 240

[62] M. Einhorn, M. Green, M. Virasoro, *Phys. Rev.* **D7** (1973) 102

[63] K. Golec-Biernat, J. Kwieciński and A. Szczurek, *Phys. Rev.* **D56** (1997) 3955

[64] R.D. Peccei and A. Pignotti, *Phys. Rev. Lett.* **26** (1971) 1076
J.M. Wang and L.L. Wang, *Phys. Rev. Lett.* **26** (1971) 1287
R. Rajaraman, *Phys. Rev. Lett.* **27** (1971) 693

[65] CHLM Collaboration, *Nucl. Phys.* **B51** (1973) 388
CHLM Collaboration, *Nucl. Phys.* **B54** (1973) 6
CHLM Collaboration, *Nucl. Phys.* **B72** (1974) 376
CHLM Collaboration, *Nucl. Phys.* **B73** (1974) 40
CHLM Collaboration, *Nucl. Phys.* **B108** (1976) 1
UCLA-FNAL Collaboration, *Phys. Lett.* **B45** (1973) 399
ANL-FNAL Collaboration, *Phys. Rev. Lett.* **31** (1973) 1080
J. Whitemore et al., *Phys. Rev.* **D11** (1975) 3124

[66] S.N. Ganguli and D.P. Roy, *Phys. Rept.* **67** (1980) 201

[67] M. Bishari, *Phys. Lett.* **B38** (1972) 510

[68] H1 Collaboration, *Z. Phys.* **C74** (1997) 221

[69] H1 Collaboration, *Nucl. Phys.* **B619** (2001) 3

[70] H1 Collaboration, *Eur. Phys. J.* **C6** (1999) 587

[71] W. Schmidke, "Leading Baryon Production in *ep* Scattering at HERA", p.924 in A. Astbury et al., "High energy Physics" Proceedings, 29th International Conference, ICHEP 1998, Vancouver, Canada, July 23-29 , 1998. Vol. 1, 2 Signapore: World Scientific (1999) p1833

[72] L. Alvero, J.C. Colllins, J. Terron and J.J. Whitmore, *Phys. Rev.* **D59** (1999) 074022
L. Alvero, J.C. Colllins and J.J. Whitmore, [arXiv:hep-ph/9806340]
B.E. Cox, J.R. Forshaw and L. Lönnblad, [arXiv:hep-ph/0012310]
CDF Collaboration, *Phys. Rev. Lett.* **84** (2000) 5043
C. Royon, L. Schoeffel, J. Bartels, H. Jung and R. Peschanski, *Phys. Rev.* **D63** (2001) 074004

[73] Abstract 833, submitted to the XXXIst International Conference on High Energy Physics, 24-31 July 2002, Amsterdam, The Netherlands

[74] T. Chapin et al., *Phys. Rev.* **D31** (1985) 17

[75] A. Donnachie and P.V. Landshoff *Phys. Lett.* **B296** (1992) 227, [arXiv:hep-ph/9209205]

[76] W. Apel et al., *Nucl. Phys.* **B154** (1970) 189

[77] ZEUS Collaboration, *Z. Phys.* **C75** (1997) 421

[78] H1 Collaboration, I. Abt et al., *Nucl. Instr. and Meth.* **A386** (1997) 310,
H Collaboration, I. Abt et al., *Nucl. Instr. and Meth.* **A386** (1997) 348.

[79] Proceeding of the *HERA Workshop*, B.H. Wiik, Vol.1, eds. W. Buchmüller and G. Ingelman, Hamburg, 1991.

[80] HERMES Collaboration, K. Coulter et al., *DESY/PRC* **90/1** (1990).

[81] HERA-B Collaboration, *DESY/PRC* **94/04** (1992).

[82] H1 Calorimeter Group, B. Andrieu et al., *Nucl. Instr. and Meth.* **A336** (1993) 460
H1 Calorimeter Group, B. Andrieu et al., *Nucl. Instr. and Meth.* **A336** (1993) 499
H1 Calorimeter Group, B. Andrieu et al., *Nucl. Instr. and Meth.* **A344** (1994) 492

[83] H1 SPACAL Group, *Nucl. Instr. and Meth.* **A386** (1997) 397.

[84] H1 SPACAL Group, *Nucl. Instr. and Meth.* **A374** (1996) 149.

[85] P. Van Esch et al., Nucl. Instrum. Meth. **A446** (2000) 409, [arXiv: hep-ex/0001046]

[86] H. Bethe, W. Heitler, *Proc. Roy. Soc.* **A146** (1993) 83.

[87] H1 Collaboration, *Z. Phys.* **C66** (1995) 529.

[88] N. Gogitidze, H1 LUMI System Status Report. H1 Collaboration meeting, DESY, Hamburg, Germany, 13-Oct-1994

[89] S. Eichenberger et al., *Nucl. Instr. and Meth.* **A323** (1992) 532.

[90] R. Engel, *Z. Phys.* **C66** (1995) 203
R. Engel and J. Ranft, *Phys. Rev.* **D54** (1996) 4244

[91] T. Sjöstrand, *Comput. Phys. Commun.* **82** (1994) 74

[92] D. Amati, A. Stanghellini and S. Fubini, *Nuovo Cimento* **26** (1962) 896

[93] H1 Collaboration, *Z. Phys.* **C75** (1997) 607

[94] J.Ebert, J.Marks, A.Mehta, J.Phillips and L.West, HFS- a software package to cope with the hadronic final state, see http://www-h1.desy.de/ marks/hfs/hfs.html

[95] H1 Collaboration, *Nucl. Instr. and Meth.* **A386** (1997) 310-396

[96] H1 SPACAL GROUP, *Nucl. Instr. Meth.* **A374** (1996) 149-156

[97] F. James, MINUIT: Function minimization and error analysis, Computing and network division CERN, Geneva, Switzerland (1994)

[98] ZEUS Collaboration, Leading proton production in e^+p collisions at HERA,
Paper submitted to International Conference on High Energy Physics, ICHEP02, Amsterdam, July 2002 (abstract 833), Available from
http://www-zeus.desy.de/physics/phch/conf/amsterdam_paper/DIFF/lp.ps.gz

[99] H1 Collaboration, *Z. Phys.* **C69** (1995) 27

[100] M.M. Block, F. Halzen and G. Pancheri, *Eur. Phys. J.* **C23** (2002) 329, [arXiv:hep-ph/0111046]

[101] G. Baur, K. Hencken, D. Trautmann, *J. Phys.* **G24** (1998) 1657, [arXiv:hep-ph/9804348]

[102] H1 Collaboration, Measurement of semi-inclusive diffractive deep-inelastic scattering with a leading proton at HERA, Paper submitted to International Europhysics Conference on High Energy Physics EPS 2001, Budapest, July 2001 (abstract 809), Available from http://www-h1.desy.de/h1/www/publications/htmlsplit/H1prelim-01-112.long.html

[103] H1 Collaboration, *Eur. Phys. J.* **C6** (1999) 587

Summary

This thesis presents a new measurement of the diffractive dissociation cross section $M_X^2 d\sigma/dM_X^2$ for the photoproduction process $\gamma p \to XY$, with a large gap between the photon system X and Y, with Y a proton or low mass proton excitation. The cross section measurement was performed in the same two centre of mass energy-bins as a previous analysis, $\langle W \rangle$=231, 187 GeV, but now on a data sample which is improved by almost a factor of 10. We also present a new measurement which is performed at a lower centre of mass energy of $\langle W \rangle$=91 GeV. The data sample corresponds to an integrated luminosity of ~ 2 pb^{-1} which were collected with the H1 detector at HERA during a short dedicated run at the end of 1997.

The obtained differential cross section is interpreted in the framework of the phenomenological Regge model. Two types of Regge analysis are performed. The first analysis is performed in the normal Regge limit, where an effective pomeron intercept is extracted as a function of M_X^2. From this extraction one can deduce that the cross section performed on these large rapidity gap data is dominated by pomeron exchange. The second analysis, performed in the triple Regge limit performs a triple Regge fit on a combined data set of fixed target data, these rapidity gap data and leading proton data. A good description of the data over the full range is found by the triple Regge model. The pomeron intercept is extracted from the triple Regge fit and is found to be $\alpha_{I\!P}(0) = 1.13 \pm 0.06$, which is compatible with the soft pomeron extracted from the fits of Donnachie and Landshoff. Also the triple Regge couplings were extracted and found to be in fair agreement with triple Regge couplings earlier obtained on pp-data.

At the end, the triple Regge model which was used to describe the soft physics processes is also applied on processes in the deep inelastic region. By doing so the transition from the soft towards the deep inelastic region is investigated. Therefore, diffractive data in the deep inelastic region like $F_2^{D(3)}$, F_2^{LP} and F_2^{LN} were compared with a triple Regge model, using either the triple Regge couplings extracted from the combined triple Regge fit or using the triple Regge couplings which were extracted from pp-data. A satisfactory agreement is found for not too large values of Q^2 (i.e. $Q^2 \lesssim 12$ GeV^2) and not to low values of M_X.

Acknowledgements / Dankwoord

Het werk voorgesteld in dit proefschrift zou nooit tot een goed einde gekomen zijn zonder de hulp, steun en het gezelschap van verscheiden mensen werkende op het IIHE, UA en in DESY, alwaar ik verscheiden weken heb vertoefd tijdens dit doctoraat. Onmogelijk is het echter iedereen te danken die op een of andere manier heeft bijgedragen tot het verwezenlijken van dit werk en dat ga ik dan ook niet doen. Maar een aantal mensen die dicht bij het hele proces betrokken zijn geweest wil ik toch even persoonlijk bedanken.

Door de leuke en leerrijke colleges van Prof. Dr. J. Lemonne en Prof. Dr. A. Severin kwam ik voor het eerst in aanraking met de elementaire deeltjes fysica. Mede dankzij Prof. Dr. J. Lemonne werd het mogelijk een eindverhandeling te schrijven op het DELPHI experiment en later deze doctoraatsverhandeling te voltooien op het H1 experiment. Mijn oprechte dank hiervoor en voor het mogelijk maken van de vele nuttige verblijven in DESY.

Vervolgens dank ik mijn promotor Robert Roosen. Niet alleen voor de tijd die hij telkens opnieuw wist vrij te maken om naar de overeenkomst van verscheiden controle plotjes tussen Monte Carlo en data te kijken, als ook voor de constructieve commentaar op de transparanten die tijdens de diffractieve meetings gingen getoond worden, maar ook voor zijn nauwgezet commentaar bij het doorlezen van eerdere versies van dit proefschrift.

Vervolgens zou ik Pierre Van Mechelen willen bedanken voor de morele steun gedurende de hele periode waarin dit proefschrift tot stand is gekomen. Maar ook voor zijn helder kijk op verscheiden fysische problem die we zijn tegen gekomen op deze lange weg, de aangename ontspannings momenten in en buiten DESY en de ondersteuning tijdens de door mij gegeven modelinge uiteenzettingen in de diffractive werkgroep.

I want to thank also the convenors of this diffractive group, i.e. Paul Newman, Pierre Marage, Sergey Levonian, Pierre Van Mechelen and Frank-Peter Schilling, for their continous support and the many new ideas given (as well during as after these meetings), to tackel the encounterd problems in the analysis.

A special thanks to Paul Newman for his constructive help during the whole process of extracting a differential cross section and afterwards during the triple Regge analysis. During this last triple Regge step also Terry Sloan came up with some great ideas which I have worked out in this thesis, for which I want to thank him.

Ook collega's op het IIHE waren belangrijk in de ontwikkelings- en ontspannings-fasen gedurende de opbouw van dit werk: Patrick, An Fremout, Ann Van Lysebetten, Philip, Barbara, Laurent, Xavier, Caroline, Rosine, Marleen, Monique, Myriam,...

Maar ook het thuisfront liet zich niet onbetuigd in de steun. Daarom wil ik als eerste mijn papa bedanken, van wie ik hoogst waarschijnlijk deze wetenschappelijk kijk op de dingen heb mogen erven, maar die tot mijn aller grootste droefheid de voltooiing van dit werk niet heeft mogen meemaken. Maar ook mijn mama, broer en zus wil ik bedanken voor hun voortdurende steun en voor hun blijk van intresse die ze tot op de dag van vandaag nog steeds weten te tonen. Ook wil ik in dit dankwoord mijn, op dit ogenblik 10 maanden oude dochtertje, Geike, bedanken voor de grappige momenten die ze me al gegeven heeft tijdens het schrijven van dit proefschrift.

En als laatste wil ik mijn echtgenote, Greet, bedanken voor de voortdurende opvang tijdens leuke en minder leuke momenten die dit werk met zich hebben meegebracht. Zonder jouw was dit werk nooit tot een goed einde gekomen. Dank je wel!

november 2002